VILNIUS UNIVERSITY

Mindaugas Pranaitis

STUDY OF CARRIER TRANSPORT, TRAPPING AND OPTICAL
NONLINEARITIES IN POLYMERS PROMISING FOR
OPTOELECTRONIC APPLICATIONS

Doctoral dissertation
Technological Sciences, Material Engineering (08T)

Vilnius, 2012

VILNIAUS UNIVERSITETAS

Mindaugas Pranaitis

KRŪVIO PERNAŠOS IR PAGAVOS BEI OPTINIŲ NETIESIŠKUMŲ TYRIMAS POLIMERINĖSE MEDŽIAGOSE, PERSPEKTYVIOSE OPTOELEKTRONIKOS TAIKYMAMS

Daktaro disertacija
Technologijos mokslai, medžiagų inžinerija (08T)

Vilnius, 2012

The dissertation has been prepared during 2008-2012 at Vilnius University (Lithuania) and Angers University (France)

Scientific Supervisors:

Prof. Habil. Dr. Vaidotas Kažukauskas (Vilnius University, Technological Sciences, Material Engineering – 08 T)

Prof. Habil. Dr. Bouchta Sahraoui (Angers University, Technological Sciences, Material Engineering – 08 T)

Acknowledgement

I would like to express my deep and sincere gratitude to my supervisors, Prof. Habil. Dr. Vaidotas Kažukauskas and Prof. Habil. Dr. Bouchta Sahraoui. Their wide knowledge and logical way of thinking have been of great value for me. Their understanding, encouraging and personal guidance have provided a good basis for the present thesis.

I wish to express my warm and sincere thanks to my colleagues: dr. Vidmantas Kalendra, dr. Konstantinos Iliopoulos, Hasnaa El-Ouazzani.

During this work I have collaborated with many colleagues for whom I have a great regard, and I wish to extend my warmest thanks to all those who have helped me with my work.

I would like to acknowledge the financial support of the French Embassy in Lithuania.

Finally, I would like to give my special thanks to my wife Inga for her support, understanding and care.

Table of Contents

Introduction

Organic semiconductors have been the subject of the intense scientific investigations over the past 50 years. They are of great importance in physics, chemistry, material science and engineering due to their lightweight, flexibility and low fabrication cost. It is expected that, in the near future, organic materials will find widespread use in many technological applications. In the case of organic optoelectronic systems, the list of devices includes light emitting diodes (OLEDs), photovoltaic cells (OPVs), field-effect transistors (OFET), and photorefractive materials for light manipulation.

Organic and polymeric materials are also used for photonic applications: all-optical switching, modulators, optical correlators, plastic waveguides, all polymeric integrated circuits, solid-state lasers, and for biophotonic applications as in the case of the development of organic labels for multiphoton microscopy and photodynamic therapy. The advances in the developing of organic compounds with better mechanical, electrical, and optical (linear and non-linear) characteristics are of a great importance for this field.

In order to improve these user-oriented characteristics, more relevant research should be done. It is known that electrical properties of organic semiconductor, such as charge mobility and charge trapping, are decisive factors that affect the performances of the devices. The investigation of charge carrier transport behavior in conjugated polymers has been the subject of numerous investigations.

Trapping of charge carriers in organic electronic materials reduces the carrier mobility, affects the driving voltage, disturbs the internal field distribution, decreases the luminescence efficiency by quenching the emissive excited state, reduces the operation stability of organic devices, and can lead to material degradation via solid-state electrochemical reactions. The determination of energetic distribution of defects states is therefore of key

importance for controlling the material electrical properties in order to understand and to optimize charge transport in devices.

In the field of photonics organic and polymeric materials have shown great promise because of their wide-ranging properties. In addition, organic NLO materials offer simple processing techniques that are compatible with existing technologies for the fabrication of integrated optical or electrooptical devices.

The thesis is organized as follows: Chapter 1 gives an overview of organic / bio-organic semiconductors and their most general properties. It also introduces the non-linear optical properties of amorphous materials. In the Chapter 2 the fundamentals of the experimental methods are presented: the Thermally Stimulated Current Spectroscopy, Charge Extraction by Linearly Increasing Voltage, Current-Voltage characteristics and Harmonic Generation by Maker fringes methods. Chapter 3 focuses on charge carrier transport and trapping in organic semiconductors. Afterwards, the experimental results and their discussion are presented. The second part of this dissertation is a result of collaboration between Vilnius University and Angers University. The investigations of electrical and optical properties of bio-organic molecules are described in the Chapters 3.5 and 3.6.

The main goals of the thesis are advanced characterization by complementary optical and electrical methods of organic semiconductors and the complexes of DNA (deoxyribonucleic acid) designed with purposefully controllable properties for opto-, photo- and electrical applications in modern device engineering.

By planning these investigations, the following **specific tasks** were foreseen:

1. To investigate effects of molecular orientation in the single-layer poly(p-phenylenevinylene) (PPV) derivative bearing push–pull like molecules for photovoltaic devices.

2. To investigate charge transport and trapping in bulk-heterojunction poly-3-hexylthiophene (P3HT) with the fullerene derivative (PCBM)

for solar cells applications and in [poly-(2-methoxyl, 5-(3,77dimethyloctyloxy)] para phenylenevinylene) (MDMO-PPV) for light emitting diode applications.

3. To investigate electrical and linear/nonlinear optical properties of bio-organic materials consisting from DNA and different type surfactants complexes for photonics application.

Scientific novelty and importance

1. It was demonstrated that the polymer photovoltaic device having an active layer with donor/transmitter/acceptor structure bearing polar molecules exhibits the improvement of the external quantum efficiency associated with the growth of the mobility and reduced potential barrier for charge injection or extraction from the electrodes.

2. The impact of the trapping states and their energetical and spatial distribution on the charge transport properties of organic semiconductors was revealed by several different complementary methods.

3. It was demonstrated that carrier trapping is effectively involved in the charge transport phenomena, depending on the exciting light spectral range and applied electrical field.

4. The influence of the hybrid DNA, dyes and silica material complexes on the optical properties of bio-organic materials was proven.

5. The new cationic surfactant with a high efficiency third order nonlinear optical properties was demonstrated, which extended the range of available solvents for DNA complex.

Practical importance. Investigations made on polymeric semiconductor device should be of great interest for applications like photovoltaic solar cells and organic light emitting diodes to facilitate exciton dissociation and improve charge transport in the structure. Investigations made

on bio-organic molecules and hybrid complexes enable use DNA structures for photonics and optoelectronic devices applications.

Statements presented for defence

1. External quantum efficiency of the polymeric structure with the functionalized poly(p-phenylene vinylene) derivative bearing polar molecules can be increased up to 40 % by the orientation of the active polar molecule 4-(N-butyl-N-2-hydroxyethyl)-1-nitro-benzene, and this is associated with carrier mobility variation.

2. The high, up to $10^{-18}\,cm^{-3}$ density of the non-homogeneously distributed trapping states in π-conjugated polymeric semiconductors poly-3-hexylthiophene is one of major factor conditioning carrier transport phenomena.

3. The spectral range of exciting light and applied electric fields change filling of the distributed in energy trapping states of conjugated polymers [poly-(2-methoxyl, 5-(3,77dimethyloctyloxy)] para phenylenevinylene) (MDMO-PPV), thus enabling direct assessment of the trapping state distribution.

4. Organic and hybrid materials incorporated with DNA bio-molecules complexes form samples with enhanced from 3 % up to 15 % optical transmission and increased from 100 % to 300 % fluorescence intensity, depending on dye concentration. Moreover, due to the presence of conjugated π-electrons in nucleobases of DNA, the third order nonlinear susceptibility increase up to 3 times as compared with undoped complexes.

Author's contribution

The author carried out the majority of experiments described in the thesis. He wrote and applied computer programs for modeling of trap distribution, mobility dependence and nonlinear optical susceptibility. The

author personally prepared the drafts of the publications [A10, A11, A12], and also had contributed to the preparation of others manuscripts.

List of papers related to the thesis

A1.   C. Sentein, L. Rocha, A. Apostoluk, P. Raimond, I. Duyssens, I. Van Severen, T. Cleij, L. Lutsen, D. Vanderzande, V. Kažukauskas, M. Pranaitis, V. Čyras, Evidence of the improvement of photovoltaic efficiency by polar molecule orientation in a new semiconducting polymer. // Sol. Energ. Mat. Sol. C. 91 1816–1824 (2007).

A2.   V. Kažukauskas, V. Čyras, M. Pranaitis, A. Apostoluk, L. Rocha, L. Sicot, P. Raimond, C. Sentein. Influence of polar molecular chain orientation on optical and carrier transport properties of polymer blends // Org. Electron. 8 21 – 28 (2007).

A3.   V. Kažukauskas, V. Čyras, M. Pranaitis, C. Sentein, L. Rocha, P. Raimond, I. Duyssens, I. Van Severen, T. Cleij, L. Lutsen, D. Vanderzande. Improvement of photovoltaic efficiency by polar molecule orientation in a newly developed semiconducting polymer // Thin solid films. 516 24 8963-8968 (2008).

A4.   V. Kažukauskas, M. Pranaitis, L. Sicot, F. Kajzar. Negative mobility dependence on electric field in poly(3-alkylthiophenes) evidenced by the charge extraction by linearly increasing voltage method // Thin Solid Films 516 8988–8992 (2008).

A5.   V. Kažukauskas, M. Pranaitis, A. Arlauskas, O. Krupka, F. Kajzar, Z. Essaidi, B. Sahraoui. Electrical and optical properties of thin films of DNA:PEDOT // Optical materials. 32 12 1629-1632 (2010).

A6.   V. Kažukauskas, A. Andrius, M. Pranaitis, M. Glatthaar, A. Hinsch. Charge Transport and Trapping in Bulk-Heterojunction Solar Cells // Journal of nanoscience and nanotechnology. 10 2 1376-1380 (2010).

A7.   H. El Ouazzani, K. Iliopoulos, M. Pranaitis, O. Krupka, V. Smokal, A. Kolendo, B. Sahraoui, Second- and Third-Order Nonlinearities of Novel

Push-Pull Azobenzene Polymers // Journal of physical chemistry B 115 1944-1949 (2011).

A8. M. Levichkova, D. Wynands, A. A. Levin, K. Walzer, D. Hildebrandt, M. Pfeiffer, V. Janonis, M. Pranaitis, V. Kažukauskas, K. Leo, M. Riede. Dicyanovinyl sexithiophene as donor material in organic planar heterojunction solar cells: Morphological, optical, and electrical properties // Organic Electronics. 12, 2243–2252 (2011).

A9. V. Kažukauskas, M. Pranaitis. Trap distribution near the energy band gap edge in MDMO-PPV // Functional materials letters. 4 1 53-56 (2011).

A10. M. Pranaitis, V. Janonis, A. Sakavičius, V. Kažukauskas. Determination of the charge trap energy distribution in conjugated polymer MDMO-PPV // Semiconductor science and technology. 26 8 085021 (2011).

A11. B. Sahraoui, M. Pranaitis, K. Iliopoulos, M. Mihaly, A. F. Comanescu, M. Moldoveanu, I. Rau, V. Kažukauskas. Enhancement of linear and nonlinear optical properties of deoxyribonucleic acid-silica thin films doped with rhodamine // Applied physics letters. 99, 24, 243304 (2011).

A12. B. Sahraoui, M. Pranaitis, D. Gindre, J. Niziol, V. Kažukauskas. Opportunities of deoxyribonucleic acid complexes composites for nonlinear optical applications // Journal of applied physics. 110, 8, 083117 (2011).

Publications not included in the thesis:

P1. V. Kažukauskas, M. Pranaitis, L. Sicot, F. Kajzar. Negative Mobility Dependence in Different Regioregular Polythiophenes Revealed by the Charge Extraction by Linearly Increasing Voltage Method // Mol. Cryst. Liq. Cryst. 447 141[459] – 153[471] (2006).

P2. V. Kažukauskas, M. Pranaitis, L. Sicot, F. Kajzar. Negative Mobility Dependence on Electric Field in Poly(3-alkylthiophene)s // Mater. Sci. (Medžiagotyra) 12 3 187 – 191 (2006).

P3. V. Kažukauskas, V. Čyras, M. Pranaitis, A. Apostoluk, L. Rocha, L. Sicot, P. Raimond, C. Sentein. Effect of molecular chain orientation on carrier

transport and optical properties of polymer blends // Eur. Phys. J. – Appl. Phys. 37 3 253-256 (2007).

P4. V. Kažukauskas, M. Pranaitis, V. Čyras, L. Sicot, F. Kajzar. Negative Mobility Dependence in polythiophenes P3OT and P3HT evidenced by the charge extraction by linearly increasing voltage method // Eur. Phys. J. – Appl. Phys. 37 3 247-251 (2007).

P5. V. Kažukauskas, V. Kalendra, N. Vainorius, M. Pranaitis, J. V. Vaitkus. Deep defect level spectra in the neutron irradiated Si ionizing radiation detectors // Phys. Status Solidi C 6 12 2861–2863 (2009).

P6. V. Kažukauskas, A. Andrius, M. Pranaitis, R. Lessman, M. Riede, K. Leol. Characterization of effective charge carrier mobility in ZnPc/C60 solar cells after ageing // Physica status solidi C 6 12 2864-2866 (2009).

P7. V. Kažukauskas, A. Andrius, M. Pranaitis, R. Lessman, M. Riede, K. Leol. Conductivity, charge carrier mobility and ageing of ZnPc/C60 solar cells // Optical materials. 32 12 1676-1680 (2010).

P8. N. Mongwaketsi, S. Khamlich, M. Pranaitis, B. Sahraoui, F. Khammar, G. Garab, R. Sparrow, M. Maaza // Physical origin of third order non-linear optical response of porphyrin nanorods. Mat. Chem. Phys. 134 646-650 (2012).

The results of the thesis were personally presented by the author at the following conferences:

C1. M. Pranaitis, M. Mihaly, A. Comanescu, M. Moldoveanu, I. Rau K. Iliopoulos, J. Niziol, V. Kažukauskas, B. Sahraoui. Poster presentation. Linear and nonlinear optical properties of functionalized DNA complexes. Second French-Polish, Workshop on Organic Electronics and Nanophotonics Angers, France, September 4-8, 2011.

C2. M. Pranaitis, V. Kažukauskas, B. Sahraoui, J. Niziol, O. Krupska. Oral presentation. Krūvio pernašos ir netiesinių optinių reiškinių analizė DNR kompleksuose skirtuose netiesinei optikai ir optoelektronikai // Fizinių ir

technologijos mokslų tarpdalykiniai tyrimai: pirmosios LMA Jaunųjų mokslininkų konferencijos pranešimų santraukos, Vilnius, 2011.

C3.   M. Pranaitis, M. Mihaly, A. Comanescu, M. Moldoveanu, I. Rau K. Iliopoulos, V. Kažukauskas, B. Sahraoui. Poster presentation. Linear, Nonlinear optical properties of DNA/Rhodamine-Silica thin films. 12th International Conference Electronic and Related Properties of Organic Systems, Vilnius, July 11-13, 2011.

C4.   M. Pranaitis, V. Kažukauskas. Poster presentation. Impact of the Gaussian distribution of states on thermally stimulated current specta in MDMO-PPV, 12th International Conference Electronic and Related Properties of Organic Systems, Vilnius, July 11-13, 2011.

C5.   6th International Summer School New Frontiers in Optical Technologies, Tampere, Finland. Poster presentation. 8-12 August 2011.

C6.   M. Pranaitis, V. Kažukauskas, A. Arlauskas. Oral presentation. Distribution of charge carrier traps at the band gap edges in MDMO-PPV. 3rd International Symposium on Flexible Organic Electronics, Halkidiki, Greece, 6-9 July, 2010.

C7.   M. Pranaitis, V. Kažukauskas, O. Krupka, F. Kajzar, B. Sahraoui. Poster presentation. Temperature dependent photo-conductivity of DNA:PEDOT thin films. 3rd International Symposium on Flexible Organic Electronics, Halkidiki, Greece, 6-9 July, 2010.

C8.   M. Pranaitis, V. Kažukauskas, A. Arlauskas. Oral presentation. Charge carrier transport in non-homogeneous MDMO-PPV polymer. 14 International Symposium on Ultrafast Phenomena in Semiconductors (14 UFPS). Vilnius, Lithuania, August 23-25, 2010.

C9.   V. Kažukauskas, M. Pranaitis, O. Krupka, F. Kajzar, B. Sahraoui. Poster presentation. Photoelectrical behaviour of DNA:PEDOT functionalised films. 14 International Symposium on Ultrafast Phenomena in Semiconductors (14 UFPS). Vilnius, Lithuania, August 23-25, 2010.

C10. M. Pranaitis, V. Kažukauskas, A. Arlauskas. Poster presentation. Investigation of charge trapping in disordered organic materials. 38-oji

Lietuvos nacionalinė fizikos konferencija, birželio 8-10. Vilniaus universitetas, 2009.

C11. Training courses "Organic Electronic" Technion - Israel Institute of Technology, Haifa, Israel. Oral presentation. 2008.

1. Optical, electrical properties and potential of organic materials

1.1 Organic semiconductors

Organic materials combine novel semiconducting electronic properties with the scope of easy shaping, simply controllable properties, and cheap and nature-friendly manufacturing. There is a nearly infinite variety of these organic materials and their properties can be tuned by changing their chemical structure, making them very versatile. There are two major classes of organic semiconductors: low molecular weight materials and polymers.

An important difference between these two classes of materials lies in the way how they are processed to form thin films [1]. Whereas small molecules are usually deposited from the gas phase by sublimation or evaporation, conjugated polymers can only be processed from solution e.g. by spin-coating or printing techniques.

Both classes of organic semiconductors are based on the unusual properties of the carbon atom (C: $1s^2 2s^2 p^2$). Among other configurations, it can form the so-called sp^2-hybridisations where sp^2-orbitals form a triangle within a plane and one p_z-orbital, which are perpendicular to the molecular plane. Chemical bonds formed by overlap of two sp^2-orbitals are called σ-bonds; they are localized between the bonding C atoms. The energy difference between the occupied binding orbitals and the unoccupied anti-binding orbitals is quite large and well beyond the visible spectral range. Correspondingly, longer chains of bound carbon atoms would have a large gap between the highest occupied molecular orbital (HOMO) and the lowest unoccupied molecular orbital (LUMO), leading to insulating properties. However, in the sp^2-hybridisation, the p_z-orbitals form additionally $\pi-$bonds. The overlapping p_z-orbitals established a delocalization of the electrons situated above and below the plane of the molecule. These bonds have much smaller energetic difference between the HOMO and LUMO, leading to strong absorption in or near the visible spectral range of only a few eV. In comparison with the σ electrons, the contribution of the π electrons to bonding of the molecule is thus weaker.
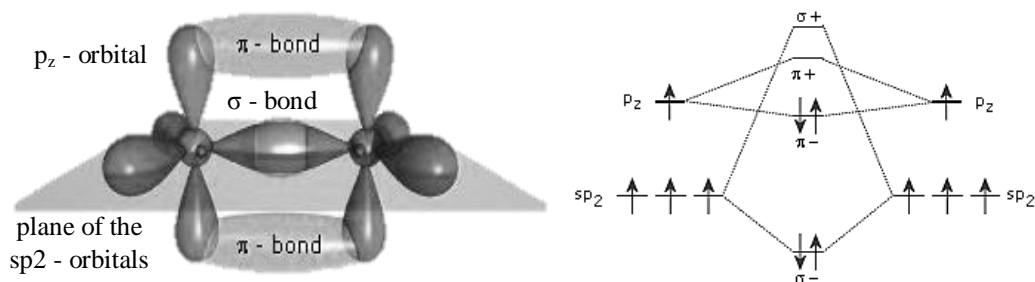
Figure 1. Scheme of the orbitals and bonds for two sp^2-hybridised carbon atoms. Left: σ- and π-bonds in ethene, as an example for the simplest conjugated π-electron system. The right viewgraph shows the energy levels of a π-conjugated molecule. The lowest electronic excitation is between the bonding π-orbital and the anti-bonding π-orbital [2].

1.1.1. Small molecules

Then carbon atoms form molecules, typically with benzene rings as the basic unit, the π-bonds become delocalized and form a π-system which often has the extensions of the molecule. The gap between occupied and empty states in these π-systems becomes smaller with increasing delocalization. These substances can be prepared as molecular single crystals. Due to the close coupling of the π-systems of the molecules in these crystals, they show in a purified form remarkable transport properties, including band transport up to room temperature with mobilities of 1-10 cm^2/Vs [3]. Most of the molecules can also be easily evaporated to form polycrystalline (mobilities typically around 10^{-3} cm^2/Vs) or amorphous (mobilities typically around 10^{-5} cm^2/Vs) layers at the room temperature [4,5].

1.1.2. Conjugated polymers

Semiconducting polymers are organic macromolecules which have a framework of alternating single and double carbon-carbon bonds [6,7]. Single bonds are referred to as σ-bonds and are associated with a highly localized electron density in the plane of the molecule. Double bonds contain both an σ-

bond and a π-bond. As compared to the σ-bonds forming the backbone of the molecules, the π-bonding is significantly weaker.

A typical example of a conjugated polymer is polyacetylene, which consists only of a single chain of alternating single- and double-bonds are presented in Figure 2.
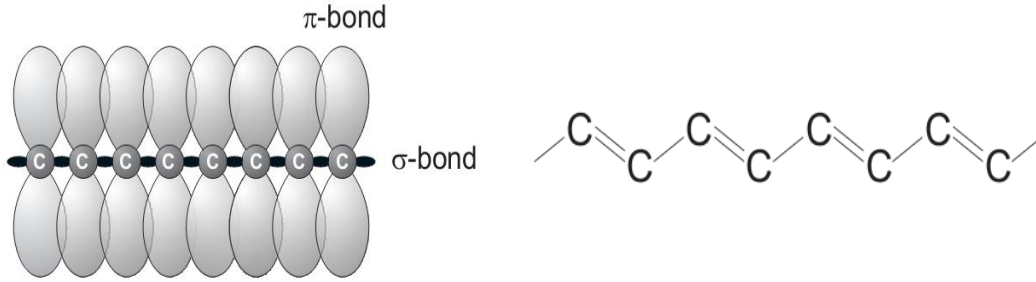
Figure 2. The polyacetylene polymer chain structure. Modified according to [8].

The transport properties of such polymers are usually determined by defects in the chains or by hopping from chain to chain. Therefore, the samples do not show band transport, but thermally activated hopping. The semiconducting polymers have attracted considerable attention due to their wide range of applications.

1.2. Charge transport in conjugated polymers

The absence of long range order in polymer semiconductors complicates the description of charge transport processes in terms of standard semiconductor models. Charge transport in organic semiconductors such as conjugated polymers is dependent on π-bonding orbitals and quantum mechanical wave-function overlap. The charge carriers are localized on polymer segments. The charge transport among these localized states is described by a hopping process. This process of phonon-induced hopping was suggested by Conwell [9] and Mott [10] in connection with metallic conduction in inorganic semiconductors. Miller and Abrahams proposed a

hopping model based on a single-phonon jump rate description [11]. Their investigations were focused on slightly doped inorganic semiconductors at low temperatures, with energetically shallow impurity centers, acting as localized states. This as variable range hopping (VRH) known model was later adopted for disordered organic semiconductors. Thereby, the hopping transport is a thermally activated (i.e. phonon assisted) tunneling between the localized states. To get from one localized state to another the charge carrier has to overcome the spatial distance as well as the energetic difference between initial and target state (Fig. 3).
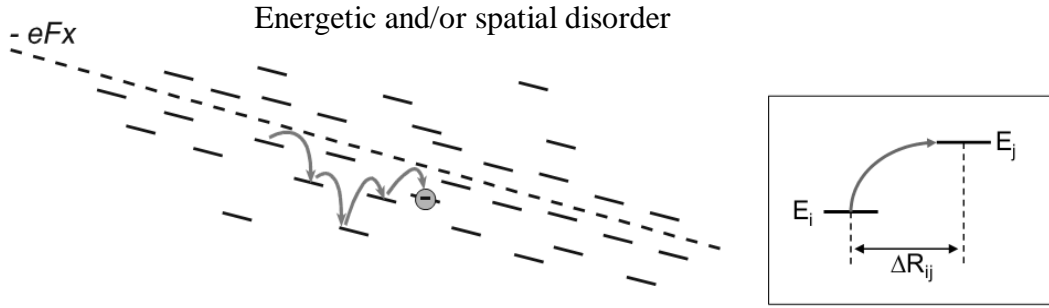
Figure 3. Energetic and spatial disorder. Left: the energetic states in applied electrical field. The right picture shows the hopping between states with energies E_i and E_j. ΔR_{ij} is the spatial distance of the two sites [12].

The former is overcome via tunneling and the latter has to be compensated by the absorption or emission of a phonon (conservation of energy). The hopping rate ν_{ij} between an initially occupied localized state i and an unoccupied localized target state j depends on the height of the energetic barrier $E_j - E_i$ and the spatial distance R_{ij} between initial and target state:

$$\nu_{ij} = \nu_0 \exp\left(-2\gamma\Delta R_{ij}\right) \begin{cases} \exp\left(-\dfrac{E_j - E_i}{k_B T}\right) & E_j > E_i \\ 1 & E_j \leq E_i \end{cases} \qquad (1.1)$$

where the prefactor ν_0 is the maximum hopping rate, called the attempt-to-escape frequency, the rate with which a charge carrier tries to escape from his localized state and in organic semiconductors it is assumed to be in the range

of 10^{11}–10^{13} s^{-1}. γ is the inverse localization radius; a quantity for the wavefunction overlap.

The first term in Equation 1.1 corresponds to the tunneling, the second to the thermal activation. For uphops the Boltzmann term is used (k_B is the Boltzmann constant and T the temperature), whereas for downhops it is approximately assumed that the emission of a corresponding phonon is always possible (probability = 1). Thus, an uphop is always harder than a downhop.

Later, Bässler [13] proposed a charge transport model for disordered organic systems. He assumed that electron-phonon coupling is sufficiently weak so that the polaronic effects can be neglected, and the hopping rates can be described by the Miller-Abrahams formalism (Eq. 1.1). The charges hop in a regular array of hopping sites. In this way both positional disorder (fluctuation in inter site distance) and energetic disorder (fluctuation in site energy) are introduced. In this model, the energy distribution of localized states can be approximated by a Gaussian function [13]:

$$DOS_{Gauss} = \frac{N_t}{(2\pi\sigma_{DOS})^2} exp\left(-\frac{E^2}{2\sigma_{DOS}^2}\right).$$

(1.2)

With N_t the density of localized states and the energy E measured relative to the center of the density of states (DOS) distribution. σ_{DOS} is the width of the distribution, a quantity of the disorder in the organic semiconductor – the less ordered, the higher is σ_{DOS}. For organic semiconductors σ_{DOS} is in the range of 50–100 meV in most cases [14]. A scheme of the hopping transport within a Gaussian distribution of localized states is shown in Fig. 4.
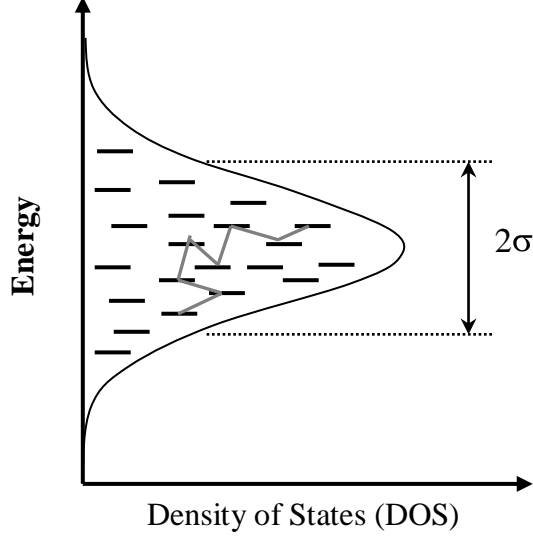
Figure 4. The hopping transport within a Gaussian distribution.

Bässler used the hopping–rate equation (Eq. 1.1) to perform Monte Carlo simulations and investigated thus the charge transport in organic semiconductors. The charge transport in the Gaussian disorder model (GDM) cannot be solved analytically and therefore an alternative approach of Monte Carlo simulations has been applied. The received mobility values from the simulations were fitted parametrically resulting in following expression for the temperature and electric field (F) dependence of the mobility [13]:

$$\mu_{GDM}\left(E\right) = \mu_\infty exp\left[-\left(\frac{2\sigma}{3k_BT}\right)^2\right]\begin{cases} exp\left\{C\left[\left(\frac{\sigma}{k_BT}\right)^2-\Sigma^2\right]\sqrt{F}\right\}, \Sigma \geq 1.5 \\ exp\left\{C\left[\left(\frac{\sigma}{k_BT}\right)^2-2.25\right]\sqrt{F}\right\}, \Sigma < 1.5 \end{cases}, \quad (1.3)$$

where μ_0 is the mobility in the limit $T\rightarrow\infty$, with values between 10^{-6} and 10^{-5} m^2/Vs, C is a constant that depends on the site spacing, and Σ is the degree of positional disorder. A few years later, another model, called correlated disorder model (CDM), was proposed by Novikov et al [15]. In the CDM the spatial and energetic disorder depend on each other, accounting for the fact that a changing environment for a given molecule will also influence its energy levels.

1.3. Nonlinear optics

The optical phenomena perceived in our life reveal the interactions of light with matter. Classical interactions like refraction and reflection occur within the linear optical domain. In this case, the light intensity transmitted is proportional to the incident light intensity. This is no longer valid for strong light intensities such as those produced by pulsed lasers. The optical properties can then vary as a function of the square, cubic or higher powers of the strength of the optical field [16]: this is the nonlinear optical domain.

The use of the first laser in 1960 made possible the creation of the field of nonlinear optics which at present plays a major role in the development in spectroscopy and laser technology. The early phases of the development and the basic principles of nonlinear optics were reviewed in the most illuminating way in the classical books by Bloembergen [17] and Akhmanov and Khokhlov [18]. A systematic introduction into nonlinear optic effects along with a comprehensive overview of nonlinear-optical concepts and devices can be found in books by Shen [19], Boyd [16], Butcher and Cotter [20], Reintjes [21] and others.

Materials with NLO properties are extensively investigated due to their potential applications in the telecommunication area, data storage, computers and display technologies.

1.3.1. Wave description in nonlinear optic

Nonlinear optics is concerned with understanding the behavior of light-matter interactions when the material's response is a nonlinear function of the applied electromagnetic field. The electromagnetic field polarizes the material, causing the positive and negative charges to move in opposite directions until they encounter the surface. The net result is a dipole moment. The electromagnetic field due to the polarization opposes the applied electromagnetic field, thus reducing the field strength inside the material.

The electric polarization, $\vec{P}(t)$, is the dipole moment per unit volume, and is a function of an applied optical field of a material system, $\vec{E}(t)$. When the applied electromagnetic field strength is much smaller than the electromagnetic fields that hold an atom or molecule together, the relation between polarization and electromagnetic field can be written as a source of new components of the electromagnetic field acting the time varying higher-order polarization components:

$$\vec{P}(t) = \chi^{(1)}\vec{E}(t) + \chi^{(2)}\vec{E}^2(t) + \chi^{(3)}\vec{E}^3(t) + \ldots = \vec{P}^L(t) + \vec{P}^{NL}(t) , \quad (1.4)$$

where

- $\chi^{(1)}$ is the first-order linear susceptibility which describes the linear optical properties such as refraction and absorption,

- $\chi^{(2)}$ is the second-order optical susceptibility describing the second harmonic generation (SHG), linear electro-optic effect (Pockels effect) and other frequency changes,

- $\chi^{(3)}$ is the third-order optical susceptibility includes third harmonic generation (THG), degenerate four-wave mixing (DFWM), optical Kerr effect (OKE), phase conjugation, saturation absorption, photoinduced absorption and others.

Thus, for a lossless, isotropic and dispersionless nonlinear optical medium, $\vec{P}^{NL}(t)$ is taken as a source term in the Maxwell's equations, and the nonlinear optical wave equation takes the general form [16]. This description is proposed in the Gaussian system of units.

$$\nabla \times \nabla \times \widetilde{E}(t) + \frac{\varepsilon^{(1)}}{c^2}\frac{\partial^2 \widetilde{E}(t)}{\partial t^2} = -\frac{4\pi}{c^2}\frac{\partial^2 \widetilde{P}^{NL}(t)}{\partial t^2} . \quad (1.5)$$

This is the most general form of the wave equation in nonlinear optics. Here $\varepsilon^{(1)}$ is the permittivity of free space and c is speed of light (3×10^{10} cm/s).

1.4. Nonlinear optical properties of polymers

The domain of organic NLO materials took impetus when Davydov et al in 1970 established [22] the connection between enhanced nonlinear response and charge transfer in conjugated molecules. This led to an entirely new concept of molecular engineering using organic materials (conjugated polymer) for nonlinear optics. The polymers are important materials for the fast processing of information and for optical storage applications.

An important aspect in the development of organic NLO materials is the attempt to simultaneously control the NLO susceptibilities, solubility, processability, optical clarity, absorption, thermal stability through the molecular structure. This approach requires knowledge of the relationship between molecular structural features and the resultant microscopic and macroscopic properties of the material. There is a focus of attention on the electronic contribution to the NLO properties of π-conjugated systems since the realization that such systems may exhibit large ultra-fast non-resonant NLO responses [23]. The NLO response of many organic polymers is extremely rapid because the effects occur primarily through electronic polarization. The polarizability of organic materials is generally the contribution from the lattice components (atoms, molecules) because of the weak intermolecular bonding (Van der Waals, dipole-dipole interactions, hydrogen bonds). The conjugated π electron system provides a pathway for the entire length of conjugation under the perturbation of an external electric field.

The optical nonlinearity can be enhanced by increasing the length of the conjugated system, keep the planarity of the π-bridge or functionalizing the ends of π-conjugated system with appropriate electron donors and acceptor groups, which allows enhancing the asymmetric electronic distribution in either or both the ground and excited states [24]. When acceptor and donor moieties are placed at terminal position of conjugated backbone, both linear and nonlinear optical properties increases significantly which involves correlated and high delocalized π-electron states. The strength of donor and

acceptor groups and order of their stacking along the backbone plays important roles in determining the magnitude of nonlinear optical efficiency [25].

1.5. Bio-molecules, DNA

1.5.1. DNA in Photonics

In the last years is observed an increasing interest research on biological materials or biopolymers for photonic device fabrication. Among these biopolymers, deoxyribonucleic acid (DNA) has become an emerging material. The unique structure of this material provides many opportunities for device design and fabrications with novel properties such as enhanced optical performance or NLO properties.

1.5.2. Structure of DNA

Deoxyribonucleic acid is a polymer that is normally a double stranded macromolecule. Two polynucleotide chains (strands) are held together by weak forces and form a DNA molecule, the DNA double-helix. There are four different types of nucleotides found in DNA, differing only in the nitrogenous base: thymine (T), cytosine (C), adenine (A) or guanine (G) (Fig. 5). Within the DNA double helix, A forms two hydrogen bonds with T on the opposite strand, and G forms three hydrogen bonds with C on the opposite strand [26]. The monomer unit of DNA consists of two inter-twined spirals of 5-carbon sugar (deoxyribose), a nitrogen containing base attached to the sugar, and phosphate molecules linked by hydrogen-bonded base pairs. The phosphate backbone is negatively charged with H^+ or Na^+ to balance the neutrality. The width of the double helix is about two nanometers and the length of the DNA molecule depends on the number of base pairs (about a third of a nanometer per base pair).
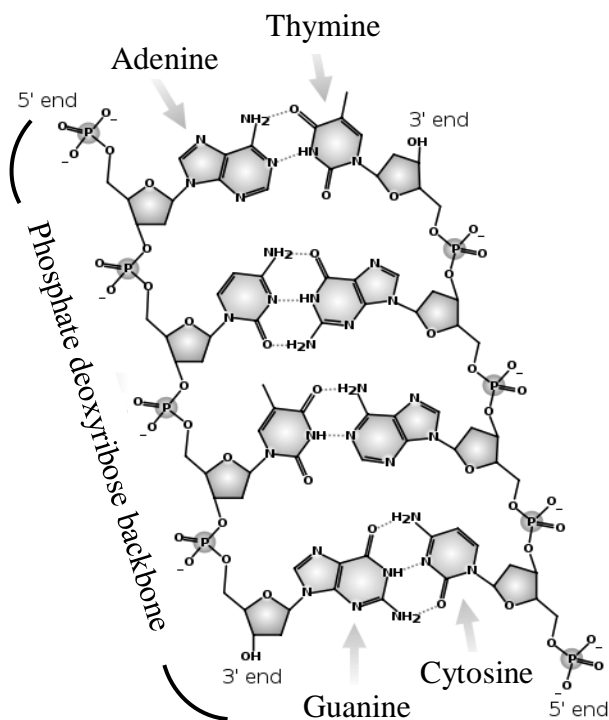
Figure 5. Chemical structure of DNA. Hydrogen bonds shown as dotted lines [27].

1.5.3. Functionalization of DNA

The pure DNA is optically and electronically inactive material. Therefore in order to obtain defined properties it have to be functionalized with active molecules, procuring a well-defined property, like good thin film formation ability, excellent light propagation properties, good charge mobility, etc. depending on targeted applications.

The active molecules can be blended with the DNA matrix by intercalation in stacked layers of nucleic acid bases of the helix, by inserting into the major and minor grooves of DNA helix or by electrostatically stacking on the surface of DNA helix [28]. Intercalation occurs when flat molecules of an appropriate size and chemical nature fit themselves in between base pairs of DNA. This is the principal model of the association between DNA and certain kinds of small molecules which have planar aromatic ring systems. Most minor groove binding small molecules possess four structural features like a positive charge, curvature, and flexibility and hydrogen bond donor and acceptor

28

groups to interact with complementary groups on the floor of the groove. Binding in the minor groove requires substantially less distortion of the DNA compared with intercalative binding [29]. Binding within the major groove of the double helix is rare for small molecules. Electrostatic attraction to the anionic phosphodiester groups along the DNA backbone is possible for cationic molecules.

Minor groove binders usually have a limited flexibility since this allows the molecule to adjust its structure to follow the groove as it twists around the central axis of the helix [30].

Usually the functionalization of DNA with organic polymers (surfactants) is electrostatic, occurring between the negatively charged phosphate group and the headgroup of the surfactant. Ionic surfactants, either anionic or cationic, can strongly interact with oppositely charged DNA. This is attributed to the electrostatic attraction and to the hydrophobic interaction between molecules [31]. This interaction is influenced by the length of the hydrophobic carbon chain and the size of the polar headgroup of cationic surfactants.

Item the DNA can be functionalized with organic–inorganic hybrid materials, like silica matrices with both the properties of the flexibility of an organic material and the mechanical strength of an inorganic material. Here the phosphate groups of the nucleic acid form hydrogen bonds with the non-ionized silicon by the electrostatic interaction. Thus, DNA is immobilized by formation of a silica networks [32, 33].

2. Experimental Methods and Techniques

2.1 Charge Extraction by Linearly Increasing Voltage

Charge Extraction by Linearly Increasing Voltage [34], (CELIV), is a measurement technique that is used to directly measure the charge carrier mobility in semiconductors with dispersive transport. A schematic illustration

of this method is presented in Fig. 6. By applying a linearly increasing voltage to the sample with free charge carriers inside, a current response comprising a capacitive part (geometric) and an extraction current is obtained. The free charge carriers are either equilibrium carriers (due to doping or impurities).They can be injected by the electrodes or they are generated by light. From such a current transient it is possible to calculate various quantities. The only restriction imposed by the experimental setup is that at least one contact of the sample should be (partially) blocking.
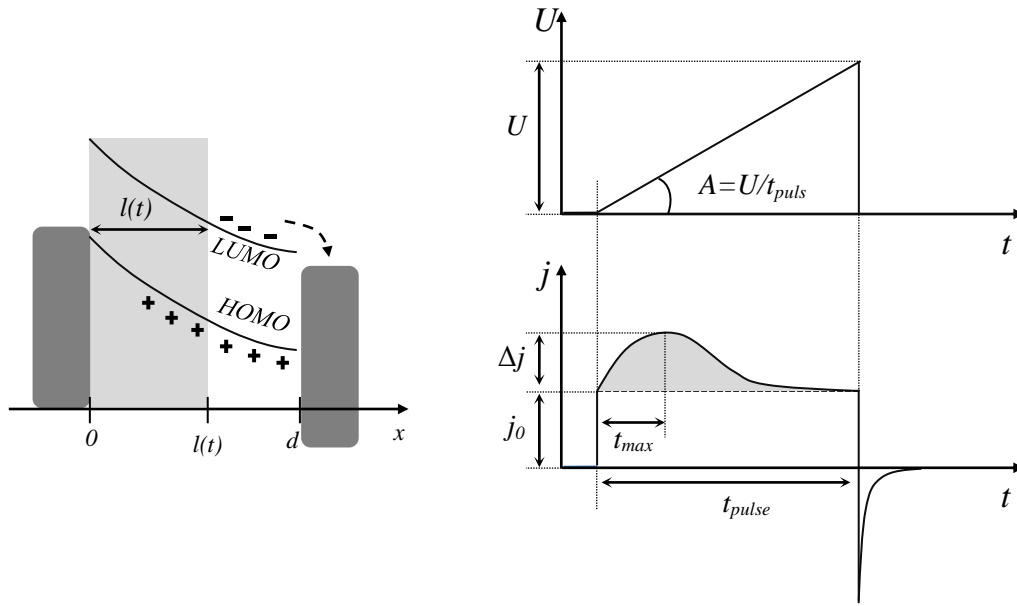

Figure 6. The principal of CELIV. On the left side is illustrated schematically the band diagram of the typical device. On the right side $A=Ut_{pulse}$ is the slope of applied voltage, j_0 is the displacement current, Δj is the extraction current, while t_{max} is the time to reach extraction current maximum [34].

In this method a linearly increasing voltage $U(t) = At$, where A is the slope of the applied voltage pulse (in these experiments, ranged between 10 and 10^6 V/s), is used to extract equilibrium charge carriers with density n and mobility μ from a film with a certain dielectric permittivity ε and thickness d. The whole device is represented as a capacitor with the film between two electrodes at $x=0$ (blocking contact) and $x = d$. At the beginning of the CELIV current transient a capacitive current step $j_0 = A \times \varepsilon\varepsilon_0/d$ is seen (Fig. 6), it can be used for estimation of d or ε of the sample. The following current increase Δj is

related to the extraction current caused by the charge carriers transported in the film. The current continues to increase as the voltage increases until the charge carriers are extracted from the film and the current drops down to the capacitive step level. In practice, if the duration of the applied triangle voltage pulse t_{pulse} is not long enough, then there might be some carriers left in the film and the extraction current will end at a higher level than the capacitive step. The mobility of extracted charge carriers is calculated from the time when the extraction current reaches its maximum (t_{max}).

The charge carrier concentration ($n = Q_{extracted}/eV$), where $Q_{extracted}$ is the extracted charge, e the elementary charge and V is the volume) is estimated from the integrated extraction photocurrent transient with respect to time.

For calculation of extraction current transients the continuity, current, and Poisson equations must be taken in to account [34]. It is assumed, that the electrode dimensions of a cell are much larger than the thickness and the charge carrier density of free charge carriers is n. Then charge carriers distribution $\rho(x,t)$ at time t is

$$\rho(x,t) = \begin{cases} en, & 0 \leq x \leq l(t) \\ 0, & x \geq l(t) \end{cases} \quad . \tag{2.1}$$

This expression is related to the time dependent extraction depth $l(t)$, where $0 \leq l(t) \leq d$. At a certain time t in the region $0 \leq x \leq l(t)$ all carriers are extracted.

Applying the increasing voltage the total current density in the external circuit due to the redistribution of the charge carriers (electric field) is

$$j(t) = j_0 + \rho(t)\left(\frac{\mu At}{d} - \frac{en\mu}{2\varepsilon\varepsilon_0}l^2(t)\right) , \tag{2.2}$$

$$\rho(t) = \begin{cases} en\left(1 - \frac{l(t)}{d}\right) & 0 \leq l(t) \leq d \\ 0 & d < l(t) \end{cases} \quad . \tag{2.3}$$

For the calculation of current transient $j(t)$ the extraction depth $l(t)$ is the crucial parameter. $l(t)$ can be expressed as a Ricatti-type first order differential equation [35]. The extraction current Δj is caused by the conductivity of the

sample and can be estimated the bulk conductivity, without interference from the contact barriers, as in [34, 36].

In order to estimate mobility from CELIV, three cases depending on the conductivity of the material must be considered:

1. *Low conductivity case*, when $\tau_\sigma >> t_{tr}$ (or $\varDelta j < j_0$), where τ_σ is the dielectric relaxation time. The charge carrier mobility is directly estimated from the extraction maximum from CELIV transients.

$$t_{max} = \frac{t_{tr}}{\sqrt{3}} = d\sqrt{\frac{2}{3\mu A}} \, , \tag{2.4}$$

$$\mu = \frac{2d^2}{3At_{max}^2} = \frac{2(\varepsilon\varepsilon_0)^2}{3[j_0]^2} \frac{A}{t_{max}^2} . \tag{2.5}$$

2. *High conductivity case*, when $\tau_\sigma << t_{tr}$ (or $\varDelta j > j_0$). The charge carrier mobility is then estimated:

$$t_{max} = \sqrt{\frac{\tau_\sigma d^2}{\mu A}} \, , \tag{2.6}$$

$$\mu = \frac{\tau_\sigma d^2}{At_{max}^3} = \frac{\varepsilon\varepsilon_0 d^2}{\sigma At_{max}^3} = \frac{2(\varepsilon\varepsilon_0)^2}{3[j_0]^2} \frac{j(0)}{\varDelta j} \frac{A}{t_{max}^2} \, , \tag{2.7}$$

3. *Moderate conductivity case*, when $\tau_\sigma \approx t_{tr}$ (or $\varDelta j \approx j_0$). The charge carrier mobility is calculated from the following equation [34]:

$$\mu = \frac{2d^2}{3At_{max}^2\left[1+0.36\dfrac{\varDelta j}{j_0}\right]} = \frac{2}{3}\frac{(\varepsilon\varepsilon_0)^2}{[j_0]^2}\frac{A}{t_{max}^2}\frac{1}{\left[1+0.36\dfrac{\varDelta j}{j_0}\right]} . \tag{2.8}$$

Experimentally it is most convenient to make measurements when $\varDelta j \approx j_0$. This may be achieved by choosing a proper A or sample of proper thickness. Namely this regime was chosen in our work.

CELIV technique was chosen due to its ability to measure simultaneously charge carrier mobility and conductivity. However, the theory for calculating the current response due to the linearly increasing voltage has only been presented for the simplified cases of low and high conductivity

regimes, respectively. Others analytical expressions for CELIV approximation were presented in [35, 37, 38].

General linearly increasing voltage could be applied not only for charge carrier transport analysis in organic semiconductor. Recently, Gaubas et al. proposed the Barrier Evaluation by Linearly Increasing Voltage Technique (BELIV) for Si solar cells and irradiated pin diodes based on measurements of current transients at reverse and forward biasing [39].

2.1.1. Experimental setup for CELIV

The setup for CELIV measurements is shown schematically in Fig. 7.
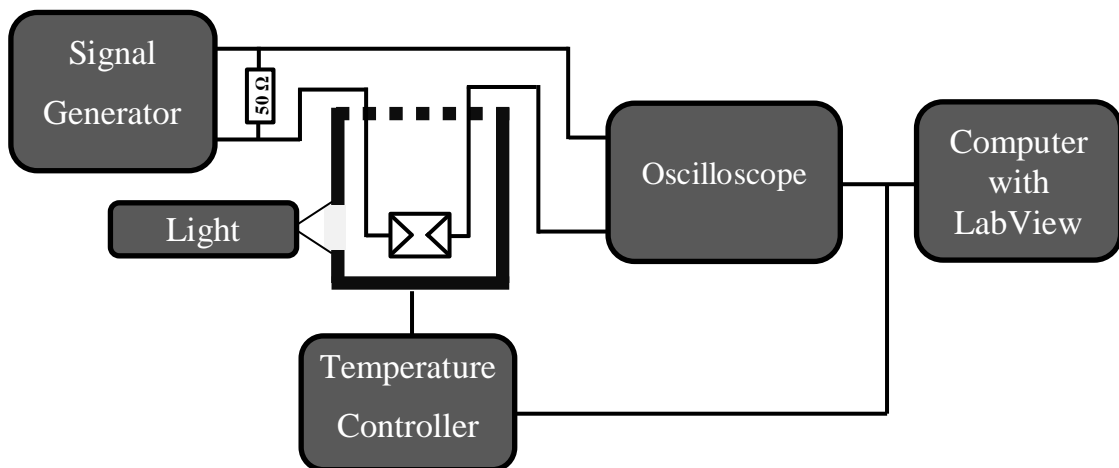
Figure 7. The experimental setup used for CELIV measurements.

Samples were placed in the nitrogen cryostat Janis VPF-475. The Agilent 33220A functional generator was used to generate the linearly increasing voltage and other arbitrary pulses. The optical excitation of the samples was achieved by illuminating with the royal blue LED Luxeon III Star (Radiometric Power – 340 @ 700mA) through both contacts. Current transients were recorded by the Tektronix TDS 2022 digital storage oscilloscope. All devices were connected through the GPIB (IEEE-488) interface to PC and controlled by using the purpose-written LabView program.

2.2. Thermally Stimulated Currents

The thermally stimulated current (TSC) technique is a quantitative spectroscopic tool which allows probing the trapping states in the energy gap of a semiconductor (organic and inorganic). In this technique, the trapped charge carriers are released by heating up the sample with a linear temperature ramp, while the stimulated current is recorded as function of temperature. The resulting curve is called a TSC curve and usually in the form of peak(s), giving information about the properties of trapping levels within and close to edges of the band gap. Trap filling can be achieved by illumination of the sample by which carriers are generated directly in the bulk or surface dependent on light wavelength, thus generating excitons which have to be separated via an electric field in the device or assisted by traps (optical trap filling). Alternatively, charge carriers can be injected via the electrodes into the sample by applying a voltage (electrical trap filling) which is accompanied by a dielectric polarization. Thereby, with a proper choice of the electrode materials electrons or holes can be selectively injected, thus allowing distinguishing between electron or hole traps [40], whereas in the case of optical trap filling this distinction is not directly possible.

The possible transitions of carriers in the band gap are the change in occupancy of the various localized energy states. The major electronic transitions associated with the TSC are described below and represented in the Fig. 8 [41].
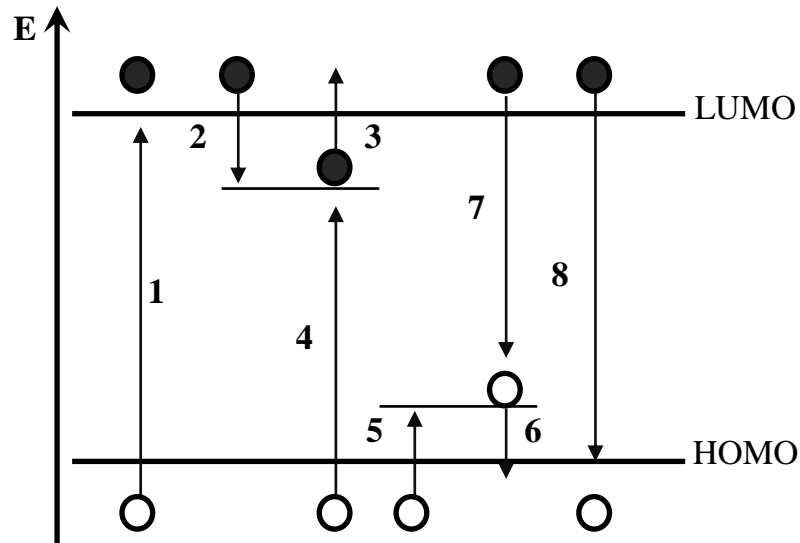
Figure 8. Transitions, which can be investigated by the TSC technique. For the sake of convenience, the simplified representation only shows discrete energy levels. 1) band to band excitation; 2) and 5) electron and hole trapping, respectively; 3) and 6) electron and hole release; 4) and 7) indirect recombination; 8) direct recombination. The arrows represent electrons and holes transitions [41].

1. Transition {1} is the band-to-band excitation of a valence band electron to conduction band. This transition occurs when valence band electron is given enough energy to jump over the band-gap.

2. Transitions {2} and {5} are called electron and hole trapping, respectively. Without any excitation the carriers remain trapped, and probability of their escape is low as compared to that at higher temperatures or upon light excitation.

3. Transitions {3} and {6} are called electron and hole generation. When enough energy (either thermal, optical or electrical) is supplied to electrons and holes in the trapping centers, they can be excited to conduction or valence bands, respectively. Depending on the level system some electrons and holes can be re-trapped at the trapping centers again.

4. Transitions {4} and {7} are indirect recombination mechanisms. These transitions occur when free electrons and holes in the conduction and valence bands, respectively, recombine with charge carriers of opposite sign in the trapping centers.

5. Transition {8} is the direct recombination defined as the recombination of a charge carrier in the conduction band with an opposite sign charge carrier in the valence band.

The transition {3} and {6} in the thermally stimulated processes give a transient increase in the conductivity of sample. This increase is observed as a peak in the TSC curve of the sample.

Such TSC experiments are used in two modes: (1) the conventional TSC mode; (2) the fractional TSC mode. In the conventional TSC mode only one temperature sweep over the whole temperature range is used to record the TSC. A typical result is shown in Fig. 9 as a solid line.
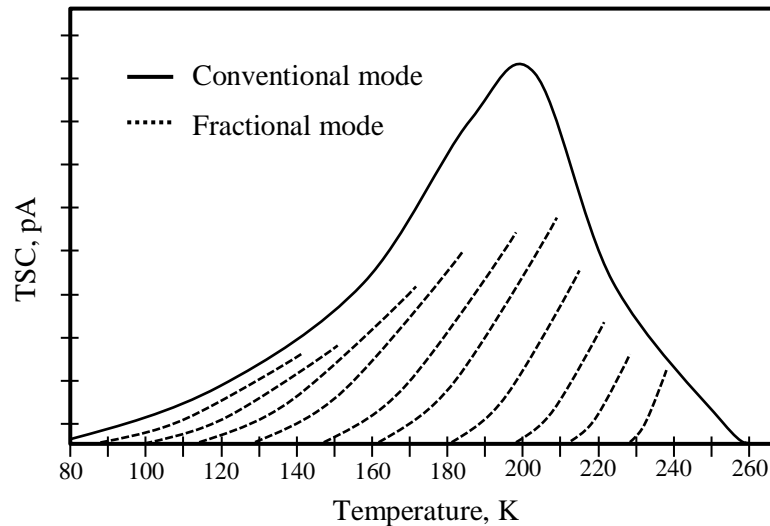

Figure 9. TSC experimental curve: conventional (solid line) and fractional mode (dashed lines).

In order to refine the obtained results or if energy distribution of the trapping states exists, the fractional techniques have to be applied. The general procedure is similar to the conventional TSC mode with the difference that multiple temperature cycles are performed. Each cycle starts with trap filling at the temperature T_{start} followed by a TSC scan up to the temperature T_{stop} and a subsequent cooling down to T_{start}. Then, without new irradiation, the next TSC scan is carried out up to next T_{stop}. The whole trap spectrum can be scanned by the stepwise increase of the preheating temperature T_{stop} and each released

36

charge per T_{stop} interval can be related to the activation energy. A lower limit of trap density n_t can be obtained by integrating the TSC spectrum over time, according to the inequality:

$$\int I_{TSC}dt \leq en_tV \qquad (2.9)$$

with the elementary charge e and the sample volume V. The inequality is caused by the fact that the estimated trap density is only a lower limit of the actual one. This is caused by two reasons; (1) incomplete trap filling, (2) recombination, (3) re-trapping. Not every trapping state has to be filled at the beginning of the measurement. In the case of optical trap filling, the incident light not only generates new electron–hole pairs but also can release already trapped charges, resulting in a specific equilibrium concentration of occupied trapping states. Furthermore, if the temperature at which trap filling is performed is too high, shallow traps will not be filled or partially emptied during the thermalization time.

In recombination case the charge carriers may recombine after they got de-trapped. The recombined charge carriers do not contribute to the current. Therefore, the measured trap density can be lower than that present in material.

2.2.1. Analysis of TSC spectrum

The spectra contain information about the energy, concentration and distribution of the trapping states. Hering and Adams in 1960 [42] elaborated the previous model [43,44] and proposed the theory to describe the thermally stimulated current in system with the monoenergetic trap levels. It was assumed that at low temperature trapping states are partly filled. The concentration of the filled trapping states n_t mainly depends on the transitions from and to trapping levels. During the heating trapped electron can be released back into the conduction band from the trapping states located at E_t. The probability of thermal generation is $exp(-E_t/kT)$ where k is Boltzmann constant. Meanwhile the unoccupied trapping states can capture free electrons. The probability of such process depends on both the concentration of free

electrons (n_c) in the conduction band and the concentration of empty traps ($N_t - n_t$). The rate of electron capture is $n_c(N_t - n_t)S_t v_e$ where N_t is trap concentration and S_t is capture cross section. v_e is thermal velocity of carriers.

Under these condition the rate equations describing the rate of change of free and trapped charge may be written as [42]:

$$\frac{dn_t}{dt} = -n_t v_0 \exp\left(-\frac{E_t}{kT}\right) + n_c(N_t - n_t)S_t v_e \ , \qquad (2.10)$$

here v_0 is the carrier attempt-to-escape frequency, $v_0 = N_c S_t v_e$. Meanwhile, the electron excited to the conduction band can either be re-trapped or recombine with the hole, directly or through a recombination center. The rate of the recombination is n_c/τ, where τ is the recombination lifetime. Then the rate of change of the free electron concentration is given by

$$\frac{dn_c}{dt} = -\frac{n_c}{\tau} - \frac{dn_t}{dt} \ . \qquad (2.11)$$

The first term in Eq 2.11 describes the loss of electrons in the conduction band due to recombination and the second term represents the change of the electron concentration in traps.

The solution of the equations 2.10 and 2.11 is usually based on two fundamental assumptions which were first introduced by Randall and Wilkins [43]. These assumptions are as follows: (1) the rate of the re-trapping of charge that has been released from a trap is negligible compared to the rate of recombination, and (2) the system is close to equilibrium. That is, the rate of change of free electron density is small as compared to the re-trapping and recombination rates (i.e. Quasi-Equilibrium). This situation of the *Slow re-trapping* can be expressed by the following inequalities:

$$\frac{n_c}{\tau} >> n_c(N_t - n_t)S_t v_e \qquad (2.12)$$

and

$$\left|\frac{dn_c}{dt}\right| << \left|\frac{dn_t}{dt}\right| \qquad (2.13)$$

Applying these approximations to Eqs. 2.10 and 2.11 leads to

$$\frac{dn_t}{dt} \approx -n_t \nu_0 \exp\left(-\frac{E_t}{kT}\right) \qquad (2.14)$$

and

$$\frac{dn_c}{dt} \approx -\frac{n_c}{\tau}. \qquad (2.15)$$

Integration of Eq. 2.14, using the relationship $T=T_0+\beta t$, results in

$$n_t = n_0 \exp\left\{-\int_{T_0}^{T}\frac{\nu_0}{\beta}\exp\left(-\frac{E_t}{kT}\right)dT\right\}. \qquad (2.16)$$

Where n_0 is the initial trapped electron concentration and T is temperature.

Then substituting Eqs. 2.15 and 2.16 into Eq. 2.14 leads to

$$n_c = n_0 \tau \nu_0 \exp\left\{-\frac{E_t}{kT} - \int_{T_0}^{T}\frac{\nu_0}{\beta}\exp\left(-\frac{E_t}{kT}\right)dT\right\}. \qquad (2.17)$$

The thermally stimulated conductivity σ is given by

$$\sigma(T) = n_c e\mu = e\mu n_0 \tau \nu_0 \exp\left\{-\frac{E_t}{kT} - \int_{T_0}^{T}\frac{\nu_0}{\beta}\exp\left(-\frac{E_t}{kT}\right)dT\right\}. \qquad (2.18)$$

Here, τ is the electron lifetime, μ is the electron mobility, β is the heating rate, T_0 is the temperature at which heating begins, after the initial filling of the traps.

Haering and Adams [42] considered the case in which the time required for thermal equilibrium between the conduction electrons and trapped electrons is much shorter than the recombination lifetime (*Fast re-trapping*). In this case TSC is given by:

$$I(T) = n_0 \frac{N_c}{N_t}\left(\frac{U}{L}\right)A\exp\left\{-\frac{E_t}{kT} - \int_{T_0}^{T}\frac{N_c}{N_t\beta\tau}\exp\left(-\frac{E_t}{kT}\right)dT\right\}. \qquad (2.19)$$

The conductivity of fast re-trapping is given by

$$\sigma(T) = n_0 e\frac{N_c\mu}{N_t}\left(\frac{U}{L}\right)A\exp\left\{-\frac{E_t}{kT} - \int_{T_0}^{T}\frac{N_c}{N_t\beta\tau}\exp\left(-\frac{E_t}{kT}\right)dT\right\} \qquad (2.20)$$

The analysis of the TSC spectrum concerning the activation energy and the distribution of the traps becomes more complicated, if the monoenergetic

traps are not well separated in the energy scale, or, moreover are non-homogeneously distributed, as in the case of organic semiconductors.

2.2.2. Distributed Traps Levels

Since the mechanisms of charge transport and photogeneration are different in organic and inorganic semiconductors, the interpretation of TSC data has to be based on the suitable models.

It is well known that trapping states in disordered materials do not have single activation energies, but are continuously energetically distributed. Statistical distributions of the energies of the localized defects and their trapping states in disordered organic materials are usually described by the Gaussian distribution function $G(E)$ [45]:

$$G(E) = \frac{N_t}{\sigma\sqrt{2\pi}} \exp\left[-\frac{(E-E_t)^2}{2\sigma^2}\right].$$

(2.21)

Here E_t is the mean value of the trapping states level, N_t is the density of trapped charge, and σ is the standard deviation representing the width of the distribution. This distribution in disordered materials is sketched in Fig. 10.
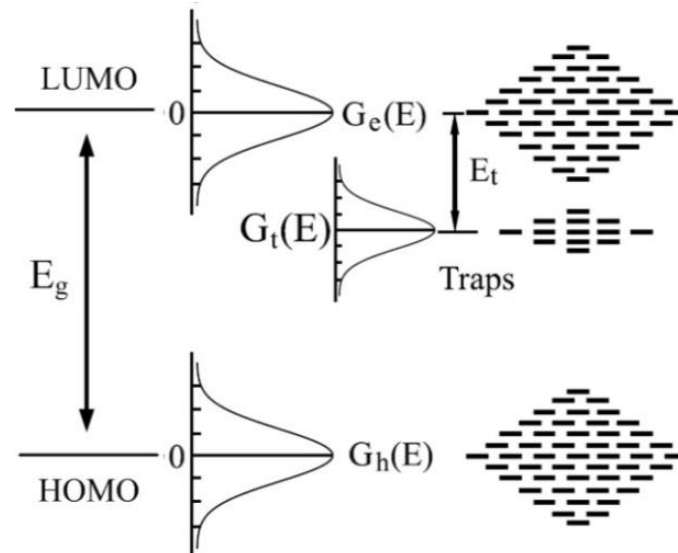

Figure 10. The energy levels with a statistical distribution of energies. $G_e(E)$ and $G_h(E)$ are the Gaussian densities of states for electrons and holes. The energy levels of trapping states within the energy gap (only electron traps are shown). E_t is the trap depth, $G_t(E)$ the density of states of the traps [13].

Therefore the expression of TSC has to take into account the energetic distribution of localized states. In such case the total stimulated current can be written as:

$$I(T) = n_0 \cdot e\mu\tau\nu_0 \left(\frac{A \cdot U}{L} \right) G(E) \cdot \exp\left(-\frac{E_t}{kT} \right) \exp\left(-\frac{\nu_0}{\beta} \int_{T_0}^{T} \exp\left(-\frac{E_t}{kT'} \right) dT' \right)$$, (2.22)

with G(E) described by Eq. (2.21).

2.2.3. Experimental setup for TSC measurements
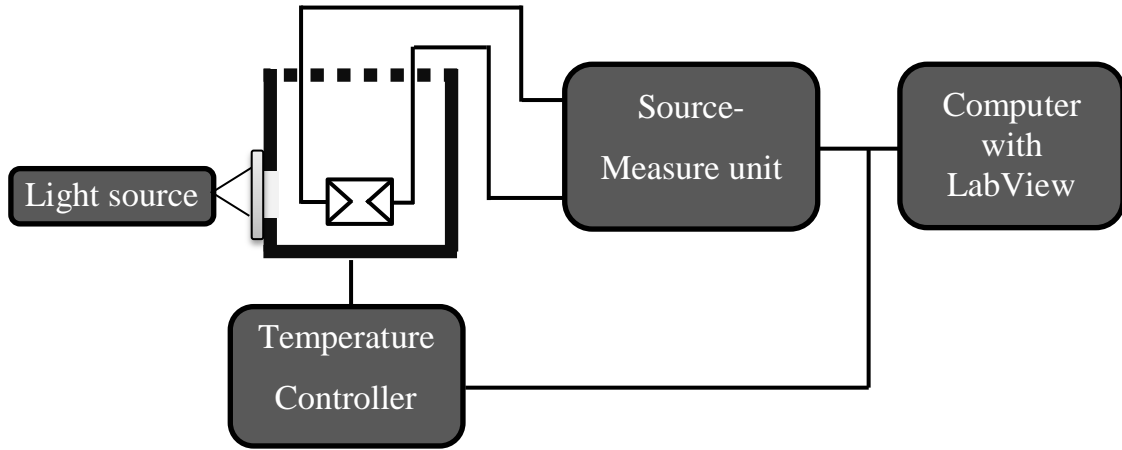
The experimental setup is shown in Fig. 11.

Figure 11. The experimental setup used for TSC measurements.

The sample was placed in the nitrogen cryostat Janis VPF-475. The standard heating rate for the TSC measurements was 10 K/min. It was controlled by the Cryocon 32 temperature controller. Trap filling was achieved by illumination of the samples through the optical window of the cryostat. The 100 W halogen lamp was used for the excitation and to increase the light power the optical lens system was used to focus all incident light to sample. In order to assure the selective excitation ten long-pass colour filters with cut-on energies from 1.77 eV up to 3.1 eV were used. The transmission spectra ranges of the used filters is presented in Fig. 12, showing that the selective

excitation of trapping states in the band gap as well as inter-band excitation of organic polymer MDMO-PPV could be assured.
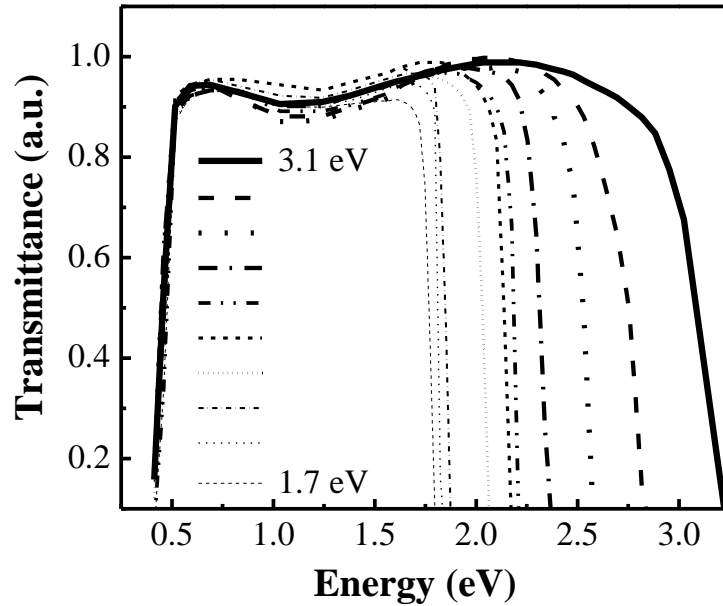

Figure 12. The spectral range of long-pass filters.

Thermally stimulated currents and I-V characteristics were measured by the Keithley 6430 Sub-Femtoamp Remote Source Meter. This device was controlled from PC through the GPIB (IEEE-488) interface.

2.3. Second Harmonic Generation

The second harmonic generation (SHG) originates from the non-linear polarization where a wave of twice frequency 2ω is generating from an incident beam of frequency ω. This second-order process concern only non-centrosymmetric materials [16]. During the experiments the changes of the second harmonic light intensity versus the incidence angle are measured. When the incidence angle is varied, the length of the optical pathway within nonlinear material is varied as well. When the thickness of the material (d) is higher than the coherence length (L_c), the wave's constraint and free interferes to each other. The intensity of the second harmonic signal describes a series of

maxima and minima called "Maker fringes" [46]. Few years later Jerphagnon and Kurtz gave theoretical description of the fringes [47].

The Maker fringes characterize the change in the interaction length when this is subjected to a rotational movement (see Fig. 13).
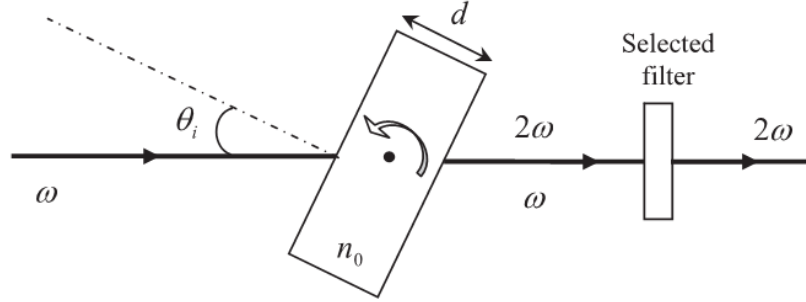

Figure 13. The principal of SHG technique. θ_i is incident angle on sample with thickness d and refractive index n_0.

The interaction length (L) is given by the following relation:

$$L = \frac{d}{\cos\theta_t} \quad \text{with } \theta_t = \arcsin\left[\frac{\sin\theta_i}{n_0}\right], \tag{2.23}$$

where d denotes the thickness of the material, Θ is incidence angle and n_0 is the refractive index of the medium.

In theoretical description of the overlapping of Maker fringes, $I_M(\theta)$, is given by

$$I_M\left(\theta\right) = \left(\frac{1}{n_{2\omega}^2 - n_\omega^2}\right)^2 (d_{eff}\left(\theta\right))^2 I_\omega^2\left(t_\omega\left(\theta\right)\right)^4 T_{2\omega}(\theta), \tag{2.24}$$

where $d_{eff}(\theta)$ is the projection of the effective nonlinear coefficient on the electric field of the fundamental wave. $t_\omega(\theta)$ and $T_{2\omega}(\theta)$ are related to the transmission coefficients (Fresnel coefficients) at the frequencies ω and 2ω, respectively. $I(\omega)$ is the intensity of incident beam, n_ω and $n_{2\omega}$ are the refractive indices of fundamental and second harmonic wave, respectively.

The models proposed in the literature for investigations of optical nonlinearities specifically depend on the types of samples: powder, solution, thin layer, bulk material, etc.

Usually, simplified model of Lee [48] or model of Herman and Hayden [49] are used for thin films.

The simplified model of Lee is based on a comparison of macroscopic NLO properties of the sample under study to those of a 0.5 mm thick Y-cut quartz, taking into account the film thickness, d, and the coherence length of quartz $l_{c,q}$:

$$\frac{\chi^2}{\chi_q^2} = \frac{2}{\pi} \frac{l_{c,q}}{d} \sqrt{\frac{I^{2\omega}}{I_q^{2\omega}}} \, , \qquad (2.25)$$

with

$$l_{c,q} = \frac{\lambda_\omega}{4 \left| n_{q\,2\omega} - n_{q(\omega)} \right|} \, , \qquad (2.26)$$

where χ^2 and χ^{2q} denote second-order nonlinear susceptibilities of the studied material and quartz, respectively.

The second harmonic wave (polarized horizontally (p)) from the fundamental wave polarized vertically (s) for nonlinear isotropic material by Herman and Hayden may be expressed as follows [49]:

$$I_{2\omega}^{s \to p}\left(\theta\right) = \frac{128\pi^5}{c\lambda^2} \frac{\left[t_{af}^{1s}\right]^4 \left[t_{fs}^{2p}\right]^2 \left[t_{sa}^{2p}\right]^2}{n_{2\omega}^2 \cos^2 \theta_{2\omega}} I_\omega^2 \, d^2 \chi_{eff}^2{}^2 \exp[-2(\delta_1 + \delta_2)] \frac{\sin^2 \Phi + \sin h^2 \Psi}{\Phi^2 + \Psi^2} \, ,$$

$$(2.27)$$

where χ^2_{eff} is the effective second-order nonlinear susceptibility, d is the film thickness; t^{1s}_{af}, t^{2p}_{fs} and t^{2p}_{sa} are transmission coefficients (system air–film–substrate–air) for fundamental and second harmonic beams. Φ and Ψ are the phase angles.

2.4. Third Harmonic Generation

In the third harmonic generation (THG) is generating a wave of triple frequency 3ω starting from an incident beam of frequency ω. Propagation of optical harmonic waves in isotropic nonlinear media was described by Bloembergen and Pershan [50] in 1962. Later, in 1985, Kajzar and Messier [51] was proposed theoretical model on THG technique in nonlinear liquid

media, which was extended to thin films [52]. This model is used to describe the basic principles of the THG technique, by detailing in particular a method for determination of the electronic contribution of third-order nonlinear susceptibility (χ^3) starting with revealing Maker fringes.

The third harmonic generation intensity from thin films (deposited on substrates) is given by

$$I^{3\omega} = \frac{64\pi^4}{c^2} \left| \frac{\chi^3}{\Delta\varepsilon} \right|_s (I^\omega)^3 \left| e^{i(\psi_s^{3\omega} + \psi_f^\omega)} \left[T_1 \ e^{i\Delta\psi_s} - 1 + \rho e^{i\phi} T_2 (1 - e^{-i\Delta\psi_f}) \right] + C_{air} \right|^2. \quad (2.28)$$

Here $\Delta\varepsilon$ is the dielectric constant dispersion of the medium:

$$(\Delta\varepsilon)_{s,f} = \varepsilon_{s,f}^\omega - \varepsilon_{s,f}^{3\omega} \quad (2.29)$$

with $\Delta\varepsilon = n^2$. The subscripts s and f refer to the substrate and thin film, respectively. The phases appearing in Eq. 2.28 are given by:

$$\psi_{s,f}^{\omega,3\omega} = \frac{3\omega l_{s,f}}{c} n_{s,f}^{\omega,3\omega} \cos\theta_{s,f}^{\omega,3\omega} \ , \quad (2.30)$$

for the waves with the frequencies ω or 3ω in the medium. $\theta_{s,f}^{\omega,3\omega}$ are the propagation angles in the given medium. l is the medium thickness, T_1 and T_2 are the factors arising from transmission and boundary conditions [53]

$$\rho e^{i\Phi} = \left. \left(\frac{\chi^3}{\Delta\varepsilon} \right)_f \middle/ \left(\frac{\chi^3}{\Delta\varepsilon} \right)_s \right. \ . \quad (2.31)$$

$\Psi_{s,f}$ is the phase of the thin film susceptibility (or difference with that of substrate if not zero), I^ω is the fundamental beam intensity and the phase mismatches $\Delta\psi_{s,f}$ are given by:

$$(\Delta\psi)_{s,f} = \psi_{s,f}^\omega - \psi_{s,f}^{3\omega} \ , \quad (2.32)$$

here $\psi_{s,f}^{\omega,3\omega}$ is given by equation 2.30.

The factors T_1 and T_2 are defined by

$$T_1 = \ t_{12}^\omega t_{23}^\omega \ ^3 \ \frac{N_2^{3\omega} + N_2^\omega}{N_2^{3\omega} + N_3^{3\omega}} \quad \text{and} \quad T_1 = \ t_{12}^\omega \ ^3 \ t_{34}^{3\omega} \ \frac{N_3^{3\omega} + N_3^\omega}{N_3^{3\omega} + N_4^{3\omega}}, \quad (2.33)$$

With $N_j^{\omega,3\omega} \cos\theta_j^{\omega,3\omega}$ and $j = 1, 2, 3, 4$. The t_{12}, t_{23}, t_{34} are transmission factors $t_{ij}^{\omega,3\omega}$ for the fundamental or harmonic waves between the media i and j. Parallel to Kajzar and Messier other theoretical descriptions were done i.e. by Reintjes [21] or Kubodera and Kobayashi [54].

Reintjes model is based on a deeper understanding of phenomena originating in the creation of Maker fringes. The intensity of the third harmonic generation in a nonlinear medium is given by the following expression:

$$I_{3\omega} = \frac{576\pi^6}{n_{3\omega} n_\omega^3 \lambda_\omega^2 c^2} \left|\chi^3\right|^2 I_\omega^3 L^2 \left(\sin\left(\frac{\Delta kL}{2}\right) \bigg/ \frac{\Delta kL}{2}\right)^2. \qquad (2.34)$$

Here I_ω and $I_{3\omega}$ denote the fundamental and harmonic light intensities, respectively, $\left|\chi^{(3)}\right|$ is the modulus of the electronic contribution of third-order nonlinear susceptibility.

$$L = d\left(\cos\left(\arcsin\left[\sin\frac{\theta_i}{n_0}\right]\right)\right)^{-1}, \qquad (2.35)$$

d is the thickness of the material, θ_i is the incidence angle and n_0 is the refractive index of the medium.

Model of Kubodera and Kobayashi compares directly the maximal amplitudes of third harmonic light intensity for the studied material to those of a 1 mm silica slab used as reference. For a weak absorption, the relation used to determine the χ^3 order of magnitude is given by the formula

$$\frac{\chi^3}{\chi_s^3} = \frac{2}{\pi} \frac{l_{c,s}}{d} \sqrt{\frac{I^{3\omega}}{I_s^{3\omega}}}, \qquad (2.36)$$

with $\chi_s^{(3)} = 2.0 \times 10^{-22}\,\text{m}^2\text{V}^{-2}$ at $\lambda_\omega = 1064$ nm [55].

In the case of significant absorption (T < 0.9), the relation becomes

$$\frac{\chi^3}{\chi_s^3} = \frac{2}{\pi} \frac{l_{c,s}}{d} \frac{\alpha/2}{1 - e^{-(\alpha l/2)}} \sqrt{\frac{I^{3\omega}}{I_s^{3\omega}}}, \qquad (2.37)$$

where α denotes the linear absorption coefficient of the material at fundamental wavelength.

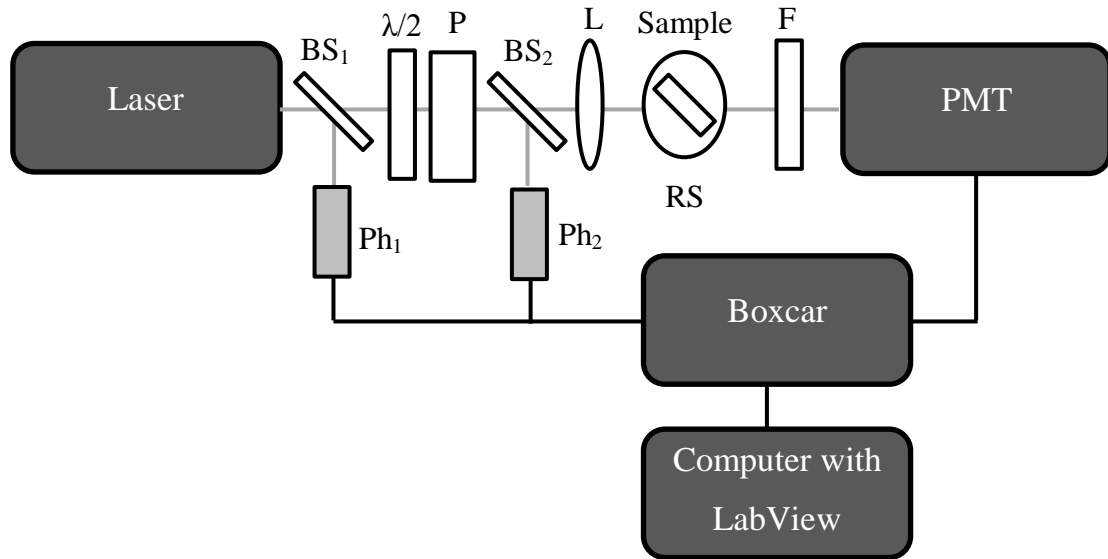## 2.4.1. Experimental setup of the 2nd and 3rd harmonic generation.

Figure 14. Experimental setup for SHG and THG: (BS_1, BS_2) beam splitters, (Ph_1, Ph_2) photodiodes, ($\lambda/2$) half-wave plate, (P) Glan polarizer, (L) convergent lens, (RS) rotation stage, (F) filter and (PMT) photomultiplier tube.

The harmonic generation experimental set-up is presented in Fig. 14. As a source the diode pumped passively mode-locked Nd:YVO_4 laser with 30 ps pulse and a repetition rate of 10 Hz was used. Two separating beam splitters (BS) are sampling one part of the incident beam on the first photodiode (Motorola MRD500; Ph_1) for synchronizing the acquisition, and on the second photodiode (Hamamatsu S1226-8BK; Ph_2) for sampling the energy of the fundamental beam. A half-wave plate ($\lambda/2$) seated before the Glan polarizer (P) controlled the polarization and the power density of the fundamental beam. A convergent lens (L), with a focal distance of 250 mm, allows to focus the Gaussian laser beam on a sample with its rotation axis placed near the focus of this lens. Samples were placed on a rotational stage (model Standa 8MR180) which rotates the sample with high precision. A selective filter KG3 (F) cut the fundamental wavelength transmitted at 1064 nm and allows passing the harmonic generated. A second interference filter FL532 permits to preserve

only the second harmonic at 532 nm ($\pm$ 1 nm) for SHG measurements and interference filter FL355 for THG. This filter is placed close to the photomultiplier (Hamamatsu R1828-01; PMT), which measures intensity of the second or third harmonic signals, respectively. A motorized rotation stage with the mounted sample allowed the variation of the incident angle with a resolution of 0.5^o. The change of the incident angle is generally made from – 70° to + 70° round the normal of the incident beam. Maker fringes were generated by rotating the sample around the axis perpendicular to the beam propagation direction. All the experiments were performed at room temperature.

3. Results of investigated organic and bio-organic polymers

3.1. Molecular orientation of NLO- poly(p-phenylene vinylene) molecules

3.1.1. Sample preparation

The functionalized soluble poly(p-phenylene vinylene) (PPV) derivative bearing polar molecules (NLO-PPV) was designed and synthesized to investigate effects of molecular orientation in single-layer polymer photovoltaic devices. Chemical structure of the material is presented in Fig. 15. The synthesis route is described in [A1].
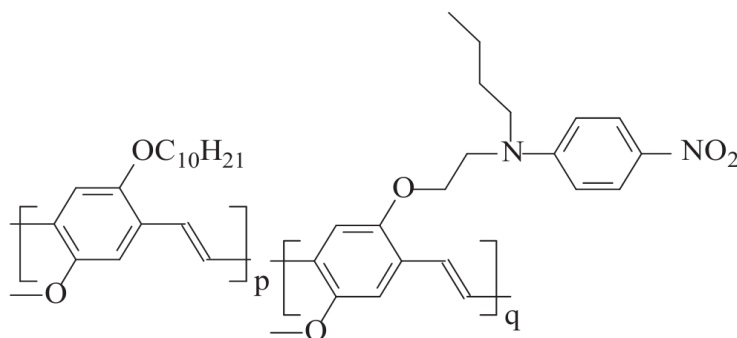

Figure 15. Chemical structure of the synthesized soluble NLO-PPV copolymer [A1].

The active polar molecule is the 4-(N-butyl-N-2-hydroxyethyl)-1-nitro-benzene group on the copolymer. It is a typical push-pull molecule with a

donor/transmitter/acceptor structure, possessing a large ground state dipole momentum which is necessary for the efficient DC-field orientation. Moreover, this grafted dye polar molecule presents no photoinduced molecular movements avoiding that way disorientation caused by the solar light illumination. It was not the case of the DR1 previously used in a model system [A2]. The active molecule is attached onto a soluble poly(p-phenylene vinylene) copolymer containing 50% of MDMO-PPV units. This copolymer is used as an isotropic polymer binder as MDMO-PPV is one of the best conjugated polymer systems so far leading to high solar efficiency. The resulting copolymer (NLO-PPV) contains 50%-molar chromophore concentration.

Test devices with the thicknesses of the active layers between 55 and 80nm were fabricated on the ITO-coated glass substrates. The copolymer film was spin-coated from a chlorobenzene solution. The semi-transparent aluminum electrode was evaporated on the top. Active surface of the devices is 28 mm^2. Orientation of the polar molecules was achieved by application of the DC voltage between the electrodes of the device preheated close to its glass transition temperature T_g (Fig. 16). The reverse bias was used to create polarization field oriented in the forward direction and vice versa. Afterwards, in order to freeze the molecular order, samples were cooled down to room temperature while maintaining the voltage.
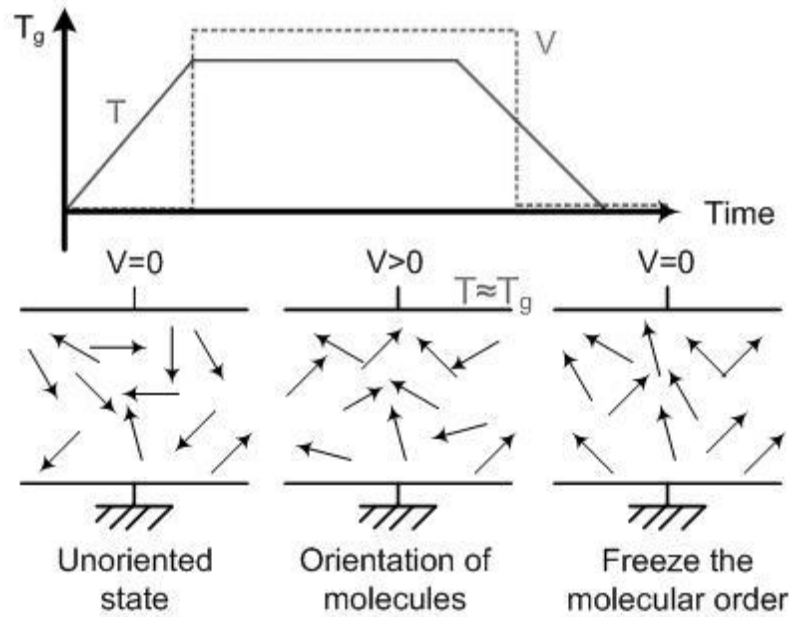
Figure 16. The scheme illustrating the principle of orientation of polar molecules.

The T_g of this new polymer has been evaluated in situ by the Second Harmonic Generation measurements. The principle of SHG studies are presented in ref. [A2]. SHG enables evaluation of the molecular order <cosθ> [56], the average polar orientation along the field direction, allowing thus optimization of the poling parameters: orientation field, poling temperature and duration. The T_g is found to be close to $55^{o}C$. Voltages of up to 100 V/μm were applied at this temperature for 10 minutes to create the orientation. The described orientation effects were reversible and reproducible after several orientation and disorientation cycles.

3.1.2. Current-Voltage Dependencies

Electrical characteristics of the test devices have been monitored in the dark. Though owing to the small polymer layer thickness, some prepared samples initially exhibited short circuits, usually they were readily cured during monitoring of the current-voltage (I-V) characteristics. After that, all the samples from the same batch gave identical and reproducible results.

I-V dependencies of a typical device are shown in Fig. 17. During the experiments, ITO electrodes were grounded, and voltage was applied to the Al

electrodes. Behavior of the I-V curves measured in the dark was found to be dependent on the polarity of the orientation voltage, as it demonstrated in Fig. 17.
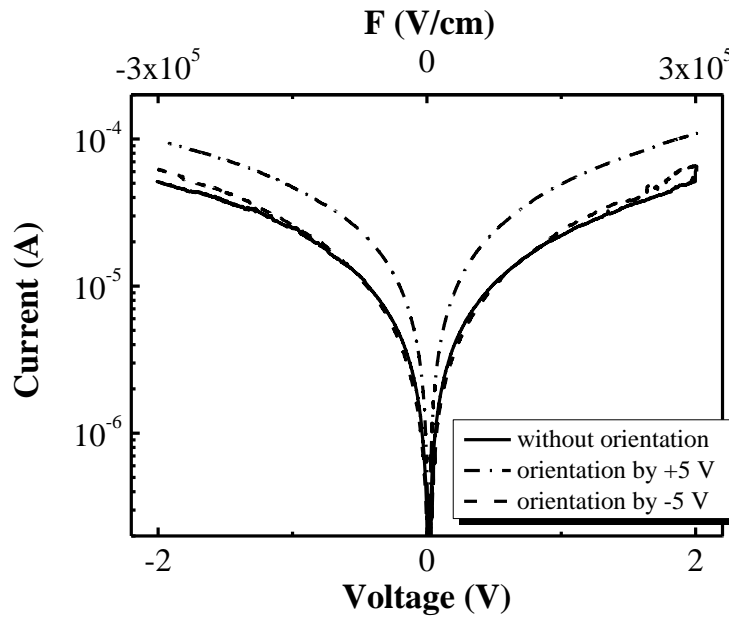

Figure 17. I-V characteristics of the device without orientation and after the orientation in different directions [A3].

Usually orientation in the forward direction resulted in the increase of the current by up to 2.5 times. In contrary, polarization with negative voltage leads at low biases to the decrease of the current as compared to the unoriented sample. This situation can be observed in Fig. 17 at applied voltages of up to 1 V. At higher voltages both currents measured after the orientation were higher than the current without orientation. Characteristically these changes were reversible after several polarization-depolarization thermal cycles with and without applied polarizing biases at high temperature, respectively.

3.1.3. Carrier Mobility

Carrier mobility dependence on the orientation and applied electric field strength was investigated by the Charge Extraction by Linearly Increasing Voltage method which is described in Section 2.1. In Fig. 18 the CELIV oscillograms are presented for the same voltage increase rate, but after different molecular orientation after illumination with blue diode.
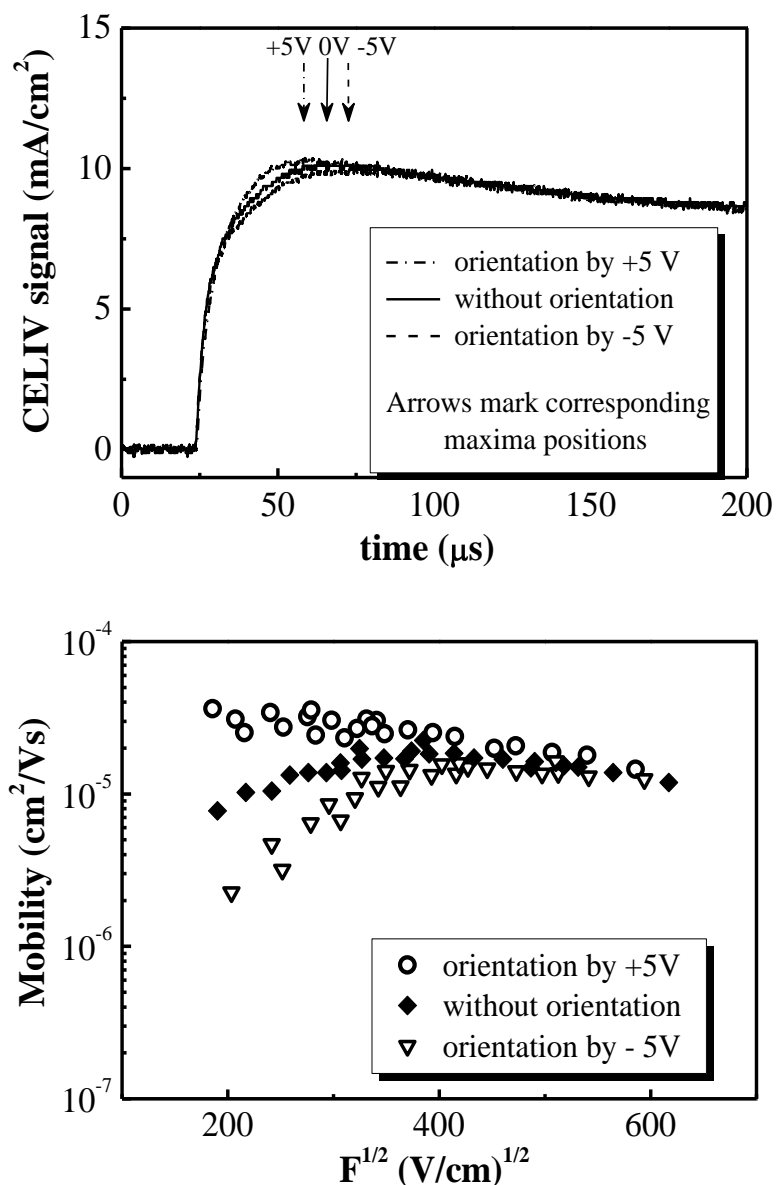
Figure 18. Carrier mobility behavior investigation in illuminated NLO-PPV. In the convention used, ITO is grounded. (top) Normalized CELIV oscillograms obtained (from the top) after orientation by +5V, without orientation and after orientation by -5V. For the sake of convenience, the traces were mathematically smoothed. Arrows mark corresponding maxima positions. (bottom) Effect of the molecular orientation on the mobility dependencies vs. applied electric field strength [A3].

It can be seen that depending on the chain orientation the maximum position changes in time, as it is indicated by the arrows. From these traces, mobility is calculated from the following:

$$\mu = \frac{2d^2}{3At_{\max}^2 \left[1 + 0.36\dfrac{\Delta j}{j_0} \right]} . \qquad (3.1)$$

Characteristically, the biggest mobility differences are observed at lowest electric fields, depending on the polarization direction, i.e., polarity of the bias, used for the poling. A notable decrease of mobility takes place upon orientation of the polar molecules in the reverse direction, and, conversely, mobility increase is observed upon orientation in forward direction.

Mobility differences diminish with increasing electric field strength . This can be explained by the fact that usually only a part of molecules are oriented, as, e.g., it was also pointed out in [57]. In this reference authors report that in the DR1-PMMA 35/65 system an effective degree of orientation of up to 30% could be reached. Therefore, at higher applied electric fields the limited built-in polarization field cannot effectively influence carrier transport any longer, and the usual transport phenomena in inhomogeneous polymer matrix become prevailing. In this region a slight decrease of mobility takes place with increasing electric field (the so called ''negative'' mobility dependence). Within the framework of the Gaussian disorder model (Section 1.3.) such behaviour is usually expected for the spatially inhomogeneous systems.

By time of flight (TOF) technique similar effect was experimentally confirmed many times in different disordered materials as, e.g., molecularly doped polymers, molecular glasses, etc. Though it was argued in [58] that sometimes TOF may give an erroneous overestimation of the mobility values if the dielectric relaxation time τ_σ is shorter than the carrier transit time t_{tr}. The condition $\tau_\sigma > t_{tr}$ has to be fulfilled in TOF to assure the constant electric field in a sample over its thickness (otherwise it can be redistributed by equilibrium charge carriers in time intervals shorter than t_{tr}), and to keep carrier number constant preventing them from recombination during their transit through the sample. The CELIV method was proved to be free of these limitations, and therefore to be much better suitable for the investigation of the high conductivity materials, in which enough carriers exist to create a measurable

current upon extraction. In polymers, the negative mobility behaviour was first evidenced by CELIV in P3HT in [59] and P3OT in [P1].

In our case, we had observed an unusual behaviour of the mobility with increasing external electric field that was especially well pronounced upon orientation in reverse direction: at the lowest fields mobility used to increase, reaching its maximum, and started decreasing again. To our knowledge such behaviour was never observed before. We have modeled it using the Gaussian Disorder Model (GDM) (Section 1.3.):

$$\mu\left(F,T\right)=\mu_{\infty}exp\left[-\left(\frac{2\sigma}{3kT}\right)^2\right]exp\left\{C\left[\left(\frac{\sigma}{kT}\right)^2-\Sigma^2\right]\sqrt{F}\right\}. \quad (3.2)$$

This equation was derived from Monte-Carlo simulations of the hopping processes of charge carriers in a material with energetic (σ) and positional disorder (Σ) described by the Gaussian distribution functions (see section 1.3.).
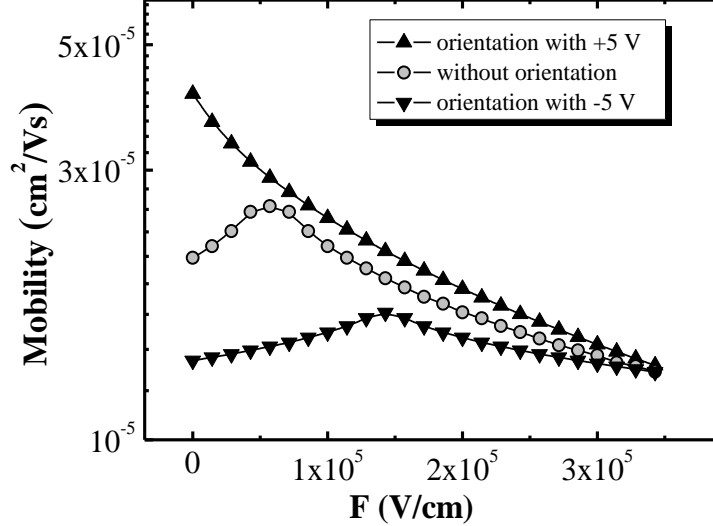

Figure 19. Modeling results of effect of the molecular orientation on the mobility dependencies vs. applied electric field strength.

To model the experimental behavior of mobility we took into account the superposition of three electric fields present in the system:

$$\vec{F}=\vec{F}_{cont}+\vec{F}_{orient}+\vec{F}_{ext}. \quad (3.3)$$

Here F_{cont} is the built-in contact field given by the different work functions of Al (4.3 eV) and ITO (4.7 eV) [60], F_{orient} is the orientation-induced internal field and F_{ext} is the applied external field. Characteristically, dependence of mobility on the molecular orientation at lower electric fields of up to $(1 \div 1.5) \times 10^5$ V/cm qualitatively coincides with the described behavior of the I-V curves. Such results enable one to state that in this region mobility makes a primary influence on the current. On the other hand, big differences in current at higher fields depicted in Fig. 19 cannot be attributed to the mobility, which becomes independent on the polarization. Probably modification of contact or surface effects cannot be excluded in this case, but this requires further investigation.

Moreover, though the qualitative agreement of the experimental and model data is quite good and explains appearance of the mobility maximum, the exact fitting using the simple approach was not possible. This could be because of the non-constant electric field strength over the thickness of the layer. Furthermore, within the framework of GDM, polarization by - 5V, leading to the appearance of the built-in field in reverse direction, could cause mobility drop because of the increased energetic and/or spatial disorder in the material. Indeed, one can assume that partial orientation of molecular dipoles in reverse direction might introduce more energetically and/or spatially scattered transport and/or trapping states that disturb carrier movement, i.e., their hopping between allowed states because of their trapping. In contrast, if the polar molecules become oriented by + 5V to create the built-in field in the forward direction, the energetic disorder is reduced and mobility behaviour is governed by the positional disorder according, resulting in the ''negative'' mobility behaviour, as discussed above.

3.1.4. External Quantum Efficiency

Finally, external quantum efficiency (EQE) measurements of the samples were performed before and after orientation under different voltages

by illumination either through the ITO electrode (150 nm) or through the Al electrode (20 nm). Measurements are presented in Fig. 20.
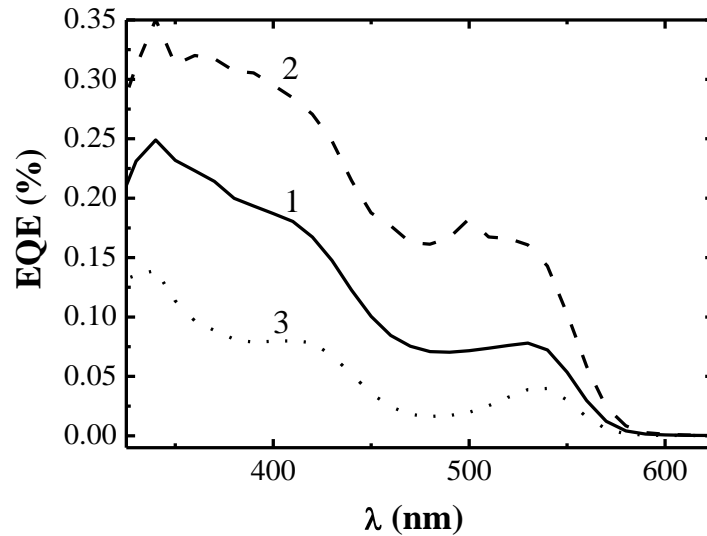

Figure 20. External quantum efficiency spectra measured for different orientation field directions. (1) Initial characteristic; (2) after orientation with +5 V; (3) after orientation with -5V [A1].

The spectra show a variation of the photogenerated current depending on the orientation bias. For a positive orientation bias, was observed an overall increase of the photogenerated current while in the case of a negative orientation bias a decrease is observed. The effect observed is not due to a purely optical modification such as an optical density variation in the polar molecule absorption range since the EQE increase occurs over the whole spectrum. Moreover, these observations are consistent with the current–voltage characteristics and the CELIV measurements for small electric fields. The qualitative effect of orientation direction is the same again as previously, confirming the role of carrier transport. An increase of around 40% of the photo generated current can be calculated from Fig. 20 by the integration of the current over the wavelengths in the visible region in the case of a device oriented with a positive bias compared with the case of an unoriented device. The EQE remains, however, low compared to the characteristics offered by photovoltaic solar cells made on a MDMO-PPV base what is not surprising

here since the device is not optimized in terms of the absorption and charges collection by the electrodes. Further, optimization will also be related to the determination of the polar molecule optimum grafting rate what will need a modeling of the internal field that can be stored in the device. For this purpose, a new method, solid electric field induced second harmonic generation (SEFISHG), which has demonstrated a good potential as a probe of the internal field induced in such structures, will be implemented to the present case [61].

3.2. Charge transport and trapping in bulk-heterojunction P3HT:PCBM solar cells

3.2.1. Samples

Organic bulk-heterojunction solar cell devices were investigated, the active layer of which was formed by the blend of poly-3-hexylthiophene (P3HT) and the fullerene derivative [6,6]-phenyl-C_{61}-butyric acid methyl ester (PCBM).

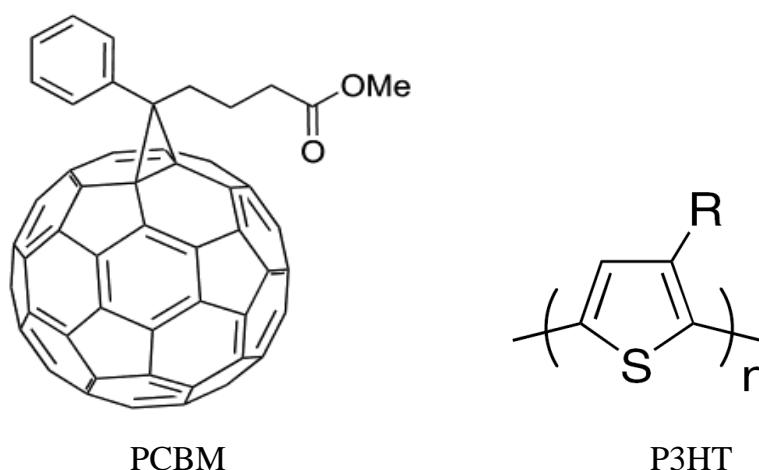The structures of both constituents are shown in Fig. 21.

PCBM   P3HT

Figure 21. Structures of the blend constituents PCBM and P3HT (R=C_6H_{13}) [62].

The investigated devices were produced in the so-called inverted layer sequence, which offers some advantages as compared to the devices of conventional structure [63]. Device layout is presented in Fig. 22.
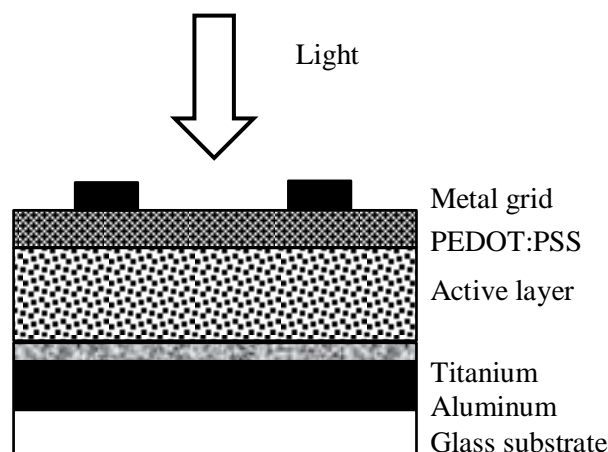
Figure 22. Schematic layout of the inverted device structure.

The devices were fabricated on a cleaned float-glass. First an 80 nm thick Al layer was thermally evaporated; afterwards, a Ti layer of 20 nm was evaporated by electron beam heating, both in vacuum better than 10^{-5} mbar. Ti forms the electron contact, while the Al layer is needed for having a high sheet conductance of the electrode. After that the photoactive layer was spin coated from the tetralin solution (~2% wt.) with a weight ratio of P3HT:PCBM being 6:5 (P3HT 4002 electronic grade synthesized by Rieke Metals, PCBM synthesized by Nano-C). The layer thickness was about 200 nm. As a hole contact 200 nm thick layer of poly(3,4-ethylenedioxythiophene) poly(styrenesulfonate) (PEDOT:PSS) was spincoated on the top (Baytron F CPP105D). To support the sheet conductance of the PEDOT:PSS layer a gold grid was evaporated upon it with a finger width of 100 μm and a distance between the fingers of 500 μm. After the preparation the samples was annealed for 10 min at 100 $^{\circ}$C.

3.2.2. Solar Cell Efficiency

Current–Voltage dependencies of the devices were measured upon illumination by AM 1.5 spectrum light with 100 mW/cm^2 incident power density to test device performance and quality. An I-V curve of sample is presented in Fig. 23.
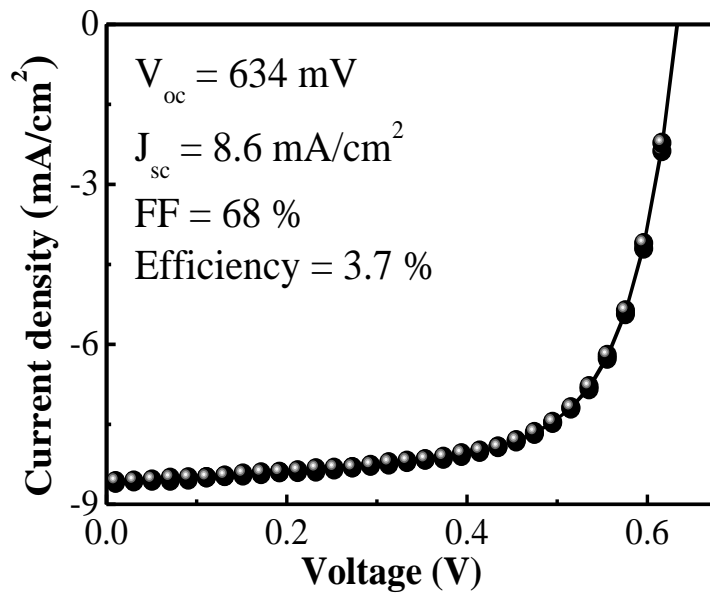
58

Figure 23. Current-Voltage dependence of the device illuminated by AM 1.5 spectrum light with 100 mW/m^2 power density [A6].

The tested devices demonstrated a solar efficiency of up to (3.7±0.2) per cent. The high fill factor of 68 per cent, the open circuit voltage of 634 mV and the short circuit current density of 8.6 mA/cm^2 evidence significant improvement of the device parameters as compared to the first devices produced in this layout [63]. The similar high fill factor was observed in the DCV6T-Bu/C60 planar heterojunction [A8]. Moreover the high fill factor indicates that transport problems are of minor importance. Nevertheless to have a clearer understanding, carrier transport properties were investigated in more detail as described below.

3.2.3. Charge Trapping

The experimental thermally stimulated current spectra measured after the light excitation in two devices fabricated on the same glass plate are presented in Fig. 24 (a and b).
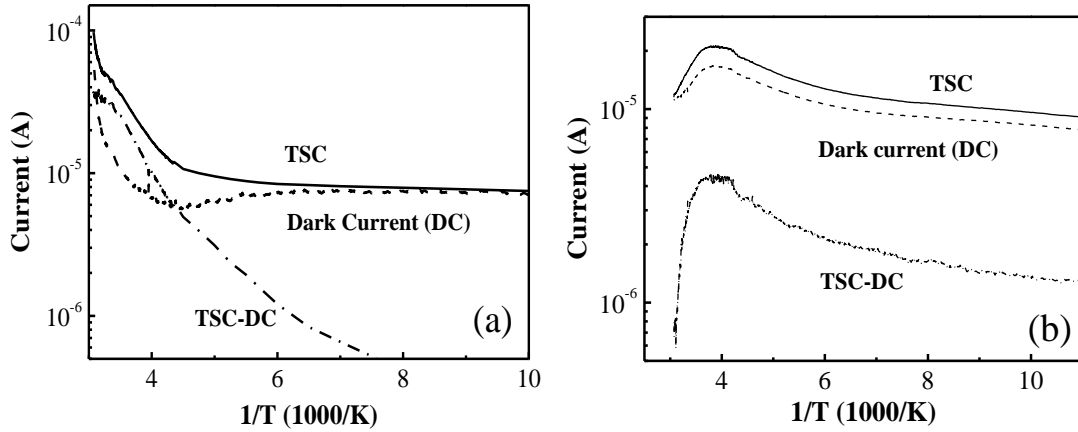
Figure 24. Experimental TSC spectra measured after excitation (solid curves), dark currents (dashed curves), and their differences (dashed-dotted curves) in two samples (a,b) [A6].

Despite the fact that the devices were produced simultaneously, their current spectra do not coincide quantitatively, indicating that even small variations in technological process might result in significant deviations of device properties. Nevertheless, upon subtraction of the dark current from the TSCs, a qualitative coincidence of the results becomes evident. In both cases characteristic maxima appear in the TSC curves, which, though being different in detail, demonstrate qualitative similarity. Appearance of the current maxima cannot be attributed to the carrier mobility behaviour within the GDM approximation, which foresees only mobility increase with temperature. Though in systems with two perfectly blocking electrodes current maxima can appear when all carriers become extracted from the device, because of the growing mobility, [64]. In such case maxima positions should demonstrate an expressed dependence on the heating rate and applied electric field [64], but this phenomenon was not observed. Moreover in our samples current growth took place after the maxima were passed, indicating that the TSC maxima were caused by the emptying of the trapping states and quite broad TSC spectrum reveals an energetic trapping states distribution. To analyze the trapping states parameters quantitatively by fitting the experimental curves a TSC model proposed and described in detail in TSC section 2.2.

60

The current caused by thermally generated carriers is calculated according to eq. 2.22 (see below)

$$I(T) = n_0 \cdot e\mu\tau\nu_0 \left(\frac{A \cdot U}{L} \right) G(E) \cdot \exp\left(-\frac{E_t}{kT} \right) \exp\left(-\frac{\nu_0}{\beta} \int_{T_0}^{T} \exp\left(-\frac{E_t}{kT'} \right) dT' \right)$$

with G(E) see taken from 2.21

Equation (2.22) can be used to model the TSC peaks, by choosing the fitting parameters E_t, n_0, ν_0 and σ.

The obtained resulting curves were modeled by taking into account the thermal generation of carriers from trap states and carrier mobility. The Variable Range Hopping model [65], frequently used to describe the electrical properties of conducting polymers at low temperatures, was found unsuitable to fit the experimental data, as demonstrating different trend. The results for the same samples are presented in Fig. 25 (a and b).
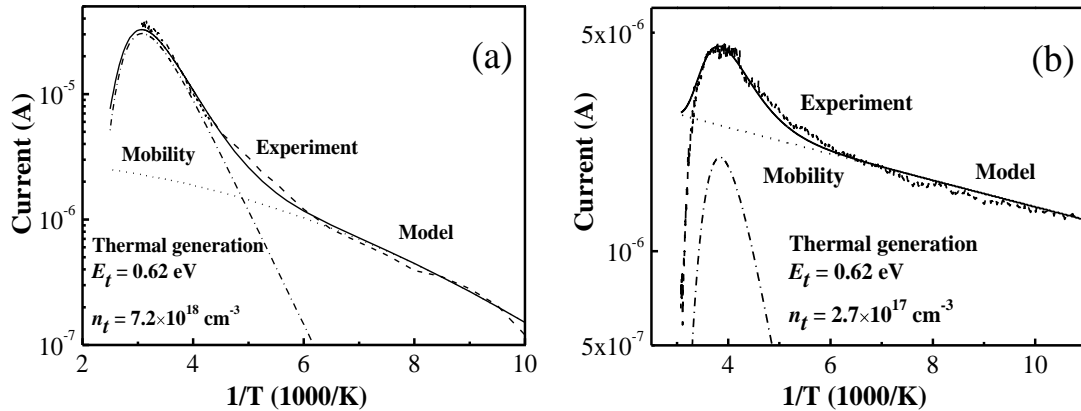

Figure 25. Experimental dependences (dashed curves) and their modeling (solid curves) by taking into account the carrier mobility variation (dotted lines) and the thermal generation of carriers (dashed-dotted curves) in two samples (a,b) [A6].

The thermal activation energy values of the traps were coinciding well within the range of experimental errors: they were equal 0.62±0.02 eV in all samples. The density of traps was evaluated by integrating the current dependence over time. It was found to range between 10^{17} cm^{-3} to some 10^{18} cm^{-3} which coinciding with found in Ref. [66]. Such high density of the traps implies that they could take active part in carrier transport, acting as transport

states and mediating carrier hopping. A similar effect called impurity band transport is well known in crystalline semiconductors. Characteristically in samples of lower conductivity trap density was also significantly lower [A2], confirming qualitatively the above conclusion. The coinciding activation energy of the traps in different samples and their high density imply that they are most probably not caused by the dopants, e.g., oxygen, but are related to material structure itself.

3.2.4. Carrier Mobility

The experimental results were analyzed numerically by taking into account mobility variation according to the Gaussian Disorder Model (GDM) approximation, due to the hopping in a Gaussian site-energy distribution, reflecting the energetic spread in the charge transporting levels of chain segments due to fluctuation in conjugation lengths and structural disorder (see section 1.3.). Fitting of the TSCs by GDM, shown in Figures 25 (a and b) by dotted lines, have given the following values: the positional disorder parameter Σ was equal to 4.5, and the parameter of energetic disorder σ ranged from 0.022 to 0.046 eV. The high-temperature mobility limit μ_∞ was found to be $(1.15 \div 2.3) \times 10^{-3}$ cm^2/Vs, meanwhile coefficient C was $(4.5 \div 5.5) \times 10^{-4}$ (cm/V)$^{0.5}$.

Results of carrier mobility measurements by the CELIV method are presented in Fig. 26.
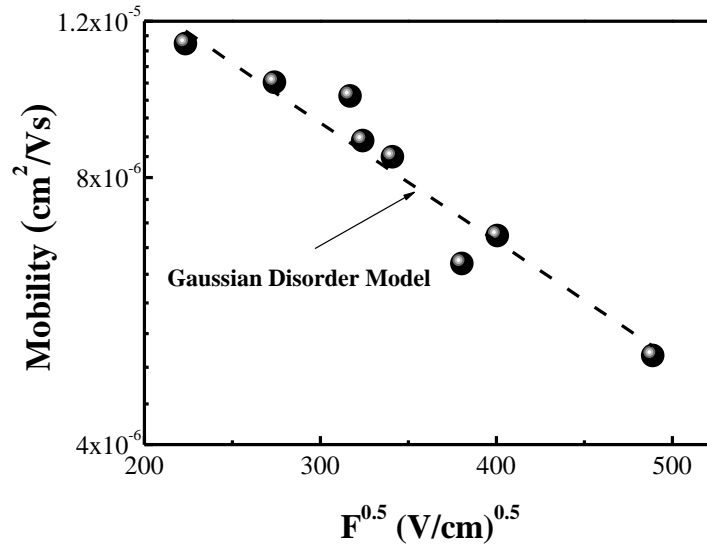
Figure 26. Mobility dependence versus applied electric field strength and its fitting by the GDM [A6].

The so-called negative mobility behaviour was observed in Fig. 26. Such behaviour is usually observed in materials in which carrier transport is governed by the positional disorder, rather than the energetic one. The prevailing role of positional disorder is quite logical in the investigated solar cells with bulk heterojunction structure in which existence of the positional disorder is the necessary condition for the high efficiency. The experimentally measured dependence in Fig. 26 was also fitted by the GDM with the following parameters: Σ = 4.5, σ = 0.045 eV, μ_∞= 9.5$\times$ 10^{-4} cm^2/Vs, C =1.8$\times$10^{-4} (cm/V)$^{0.5}$. It can be seen that the fitting parameters of the experimental data obtained by completely different methods coincide quite well. Such complex analysis has enabled not only evaluation of the trap parameters, but it has also demonstrated a clear coincidence of the results given by both methods, evidencing that carrier trapping is a decisive factor, giving their mobility behaviour.

3.3. Charge transport and trapping in MDMO-PPV as affected by the energetical distribution of trapping states

3.3.1. Samples

In this section we present the trapping states distribution dependence on the exciting light spectral range and applied electrical field in the MDMO-PPV [poly-(2-methoxyl, 5-(3,77dimethyloctyloxy)] para phenylenevinylene) synthesized in two different ways. MDMO-PPV demonstrates excellent solubility in many organic solvents, and shows a great performance in optoelectrical devices. Two popular synthesis routes are the "Gilch" and the "Sulfinyl"- type polymerizations outlined in Fig. 27.
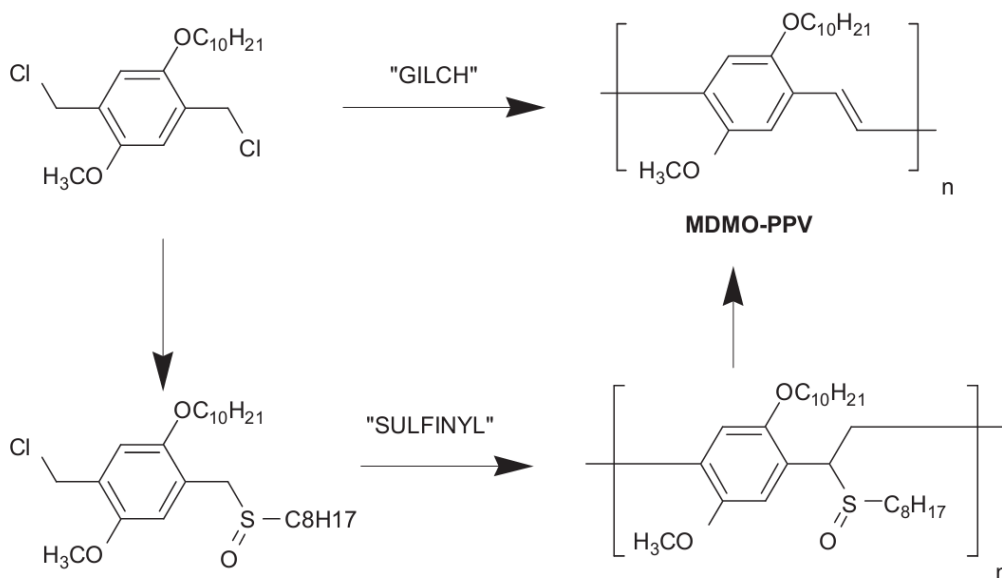
Figure 27. A schematic representation of the "gilch" and "sulfinyl" synthetic route of [poly-(2-methoxyl, 5-(3,77dimethyloctyloxy)] para phenylenevinylene) [67].

"Gilch" route is a dehydrohalogenation process which uses a dichloro-substituted monomer [68, 69]. An alternative synthesis procedure is the "sulfinyl" route, which utilizes an asymmetric chloro-, sulfinyl-substituted monomer [70, 71]. The asymmetry in the sulfinyl monomer leads to a higher regularity in the polymer due to less head-to-head or tail-to-tail additions

during polymerization. Consequently, "sulfinyl" MDMO-PPV constitutes fewer defects that may act as trap sites than regular "gilch" MDMO-PPV [72].

The layers were produced by the drop-casting on the Indium-Tin-Oxide (ITO) glass. The thickness of the films was measured by the profilometer Tencor ALFA-Step. ITO is used as the hole-injecting contact. The Al electrode was evaporated on the top at 5×10^{-6} mbar through a shadow mask. Fig. 28 shows the absorption spectra of the MDMO-PPV with a peak at 500nm.
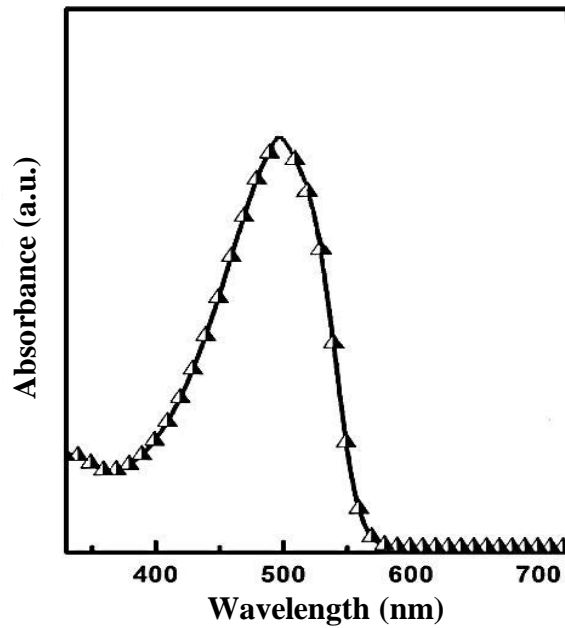

Figure 28. Absorption spectra of the MDMO-PPV [73].

3.3.2. Curent-Voltage Characteristics

Electrical characteristics of test devices have been monitored in the dark. Current–Voltage (I-V) dependencies are shown in Fig. 29.
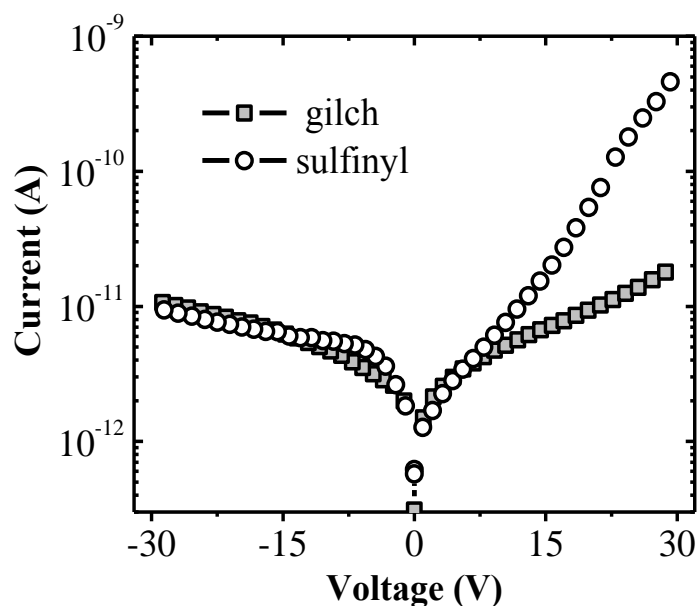
Figure 29. Current-Voltage characteristic at 290 K in MDMO-PPV samples which are synthesized in different ways.

Devices of MDMO-PPV prepared by these two routes had different I-V characteristics. The sample synthesized in "gilch" route shows lower conductivity in forward direction. This current decrease can be attributed to the presence of more trapping and/or recombination states as described above. I-V characteristics measured in the reverse direction were similar. This points out that the electrical current trough the sample is most probably controlled by the high Al/MDMO-PPV contact barrier.

3.3.3. TSC Measurements

The TSC measurements are used as direct photoelectrical method to prove distribution of trapping states in synthetized polymers.

Model comparison: Fractional TSC vs. Gaussian distribution

The typical TSC curves as function of temperature with subtracted dark current are depicted in Fig. 30.
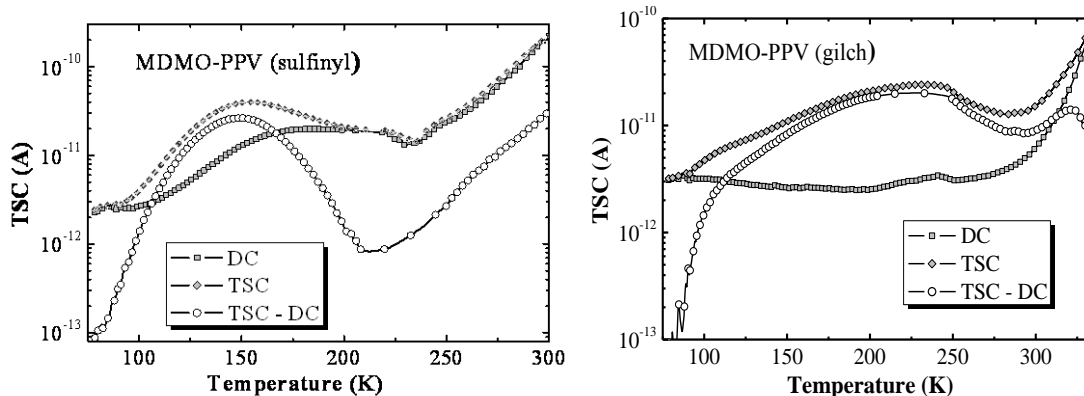
Figure 30. Experimental TSC spectra measured after excitation, dark currents, and their differences in two samples synthesized by the "Gilch" and the "Sulfinyl" routes.

The shape of both TSC spectra indicates trap distribution instead of the discrete trap levels. To gain information about trap distribution the fractional TSC measurements have been applied. Fig. 31 shows the set of the fractional TSC spectra recorded by using temperature intervals of $\Delta T=10$ K.
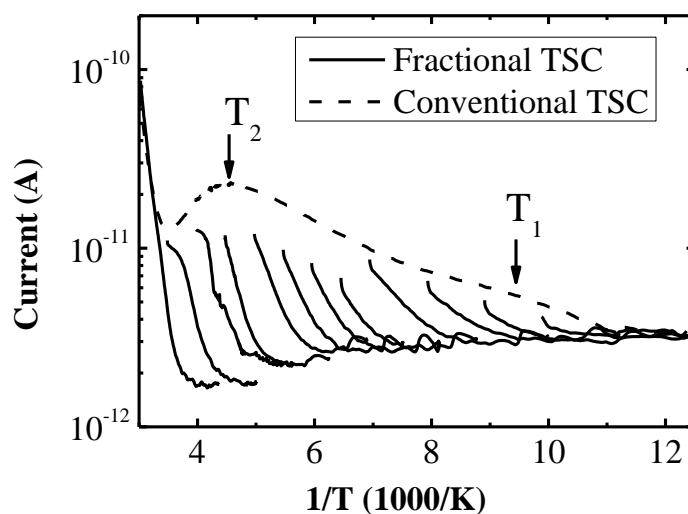
Figure 31. The set of fractional TSC spectra.

The standard TSC exhibits a main TSC peak at about 240 K (T_2) as well as a shoulder at about 120 K (T_1), indicating two different trap distributions. The continuous increase of the activation energies with temperature without any plateaus indicates a continuous trap distribution instead of discrete trap levels [40], as it was already expected on the basis of the broad TSC spectrum.

The each peak activation energy can be described by numerical calculation as [74]:

$$I(T) = N_t e \mu \tau \nu_0 \left(\frac{U}{L} \right) A \exp \left\{ -\frac{E_t}{kT} - \frac{\nu_0 kT^2}{\beta(E_t + kT)} \exp \left(-\frac{E_t}{kT} \right) \right\}$$

(3.4)

The filling of the traps was evaluated by integrating the experimental curves over time; it coincided well with the values obtained from eq. 2.9. By fitting experimental data, the values of E_t, N_t, and ν_0 were used as fitting parameters. At the highest temperatures, appearance of the effective thermal generation process is seen in Fig. 31. It's influence masks that of the generation from the trap T2, making it difficult to assess it.

The obtained density of the filled trapping states depending on the activation energy is presented in Fig. 32.
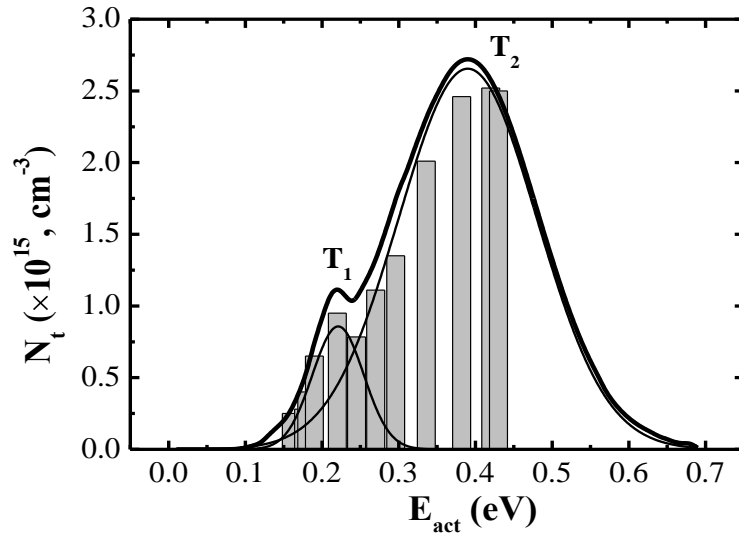
Figure 32. Filled trapping state density vs. activation energy. T_1 and T_2 present the maximum position of two different traps levels.

The filled trapping states distribution is rather broad. The histogram demonstrates a continuous trap distribution with activation energies between about 150 meV and 450 meV and two maxima at about 220 meV and 380 meV, indicating two different traps (T_1, T_2). The density of states demonstrates the Gaussian distribution, as already described in section 2.2.2. Consequently,

the experimental data were approximated by the Gaussian distribution function with the following parameters: $\sigma_1 = 25$ meV and $N_{t1} = 1.2\times10^{15}$ cm^{-3}, $\sigma_2 = 90$ meV and $N_{t2} = 2.7\times10^{15}$ cm^{-3} (solid lines in Fig 32). These two traps might results from structural defects; as, e.g. chain ends and irregularities of the polymer layer.

According to these results the same TSC curve were fitted with equation proposed in [A10]:

$$I(T) = N_t \cdot e\mu\tau\nu_0 \left(\frac{A \cdot U}{L}\right) G(E) \cdot \exp\left(-\frac{E_t}{kT}\right) \exp\left(-\frac{\nu_0}{\beta} \int_{T_0}^{T} \exp\left(-\frac{E_t}{kT'}\right) dT'\right), \quad (3.5)$$

with G(E) given by Eq. 2.21.

To limit the number of the fitting parameters, the following equations were used to determine the initial density of the filled traps N_t [75] and attempt to escape frequency ν, respectively.

$$N_t = \frac{Q}{ALeG}. \quad (3.6)$$

Here Q is the amount of charge released during a TSC experiment. It was calculated by integrating experimental curves over time. G is the photoconductivity gain, A is the area of the sample, and L is its thickness. The attempt to escape frequency is given by [76, 77]:

$$\nu_0 = 3\beta \left(\frac{T_m T'}{T_m - T'}\right) \exp\left(\frac{E_t}{kT_m}\right). \quad (3.7)$$

The variable T' is the temperature at the half of the maximum current value on the low temperature side of the current peak. A trap is characterized by the maximum in the thermally stimulated current appearing at the temperature T_m. This method is valid for the small heating rates and/or for the traps with the high attempt to escape frequencies, as it was in our case.

An example of the fitting is presented in Fig. 33.
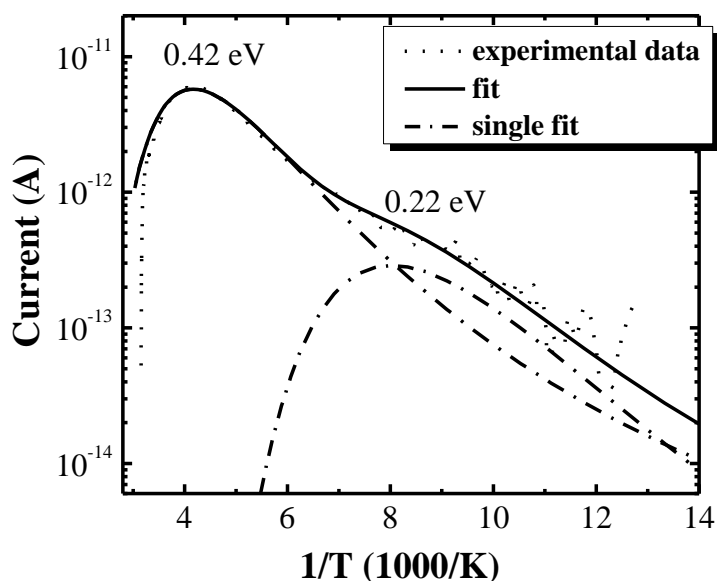
Figure 33. Example of the fitting of experimental TSC. Dashed line shows experimental data, solid curve is fitting results, dotted lines represent thermal generation of carriers from trapping states [A10].

The superposition of the two Gaussian peaks with maxima located at 0.22 eV and 0.42 eV, respectively is clearly seen in Fig. 33. The parameter σ which describes the Gaussian distribution width was 70-100 meV. These values coincide with the reported in literature [4].

3.3.4. Trapping states distribution depending on the exciting light spectral range

In order to measure the trapping states distribution depending on the exciting light spectral range the samples were excited by light with different spectral regions to assure selective excitation of the defect states. As LUMO and HOMO bands of MDMO-PPV are located at -2.8 eV and at -5 eV, respectively, excitation below and above band-gap by light passed through the long-pass colour filters with cut-on energies from 1.77 eV up to 3.10 eV was used. The traps were optically filled at 77 K. The possible ways of trapping states excitation are presented in Fig. 34. Afterwards, before starting the temperature scan, the sample was kept in the dark at liquid nitrogen (LN)

70

temperature to assure the thermalization of carriers and filling of the trapping states (usually for more than 600 s).
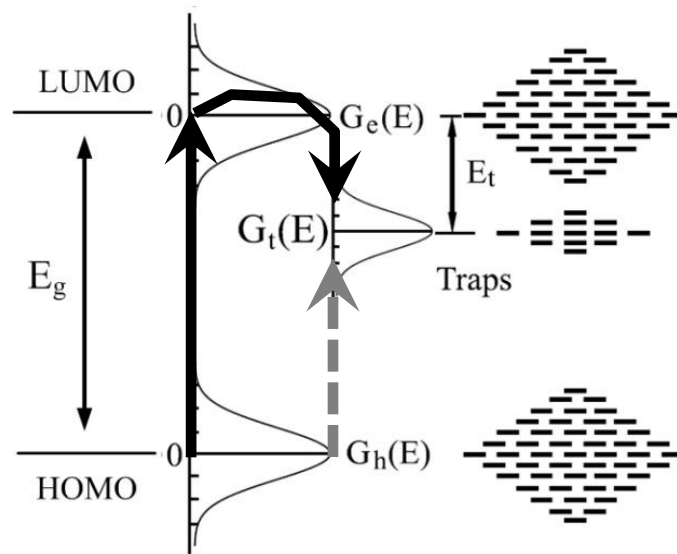
Figure 34. Energy levels with a statistical distribution of energies. E_t is the trap depth, $G_t(E)$ the density of states of the traps. The arrows indicate the excitation below (grey arrow) and above band-gap (black arrows).

After the light was turned off, the constant bias was applied, and the samples were heated at 10 K/min to measure TSCs. The bias was supplied and current was measured by the source-measure unit Keithley 6430. The dark currents at the same bias were measured too and subtracted from the TSC data obtained after the light excitation. The TSC curves as function of temperature with subtracted dark current are depicted in Fig. 35, depending on the cut-on energies of the long-pass colour filters.
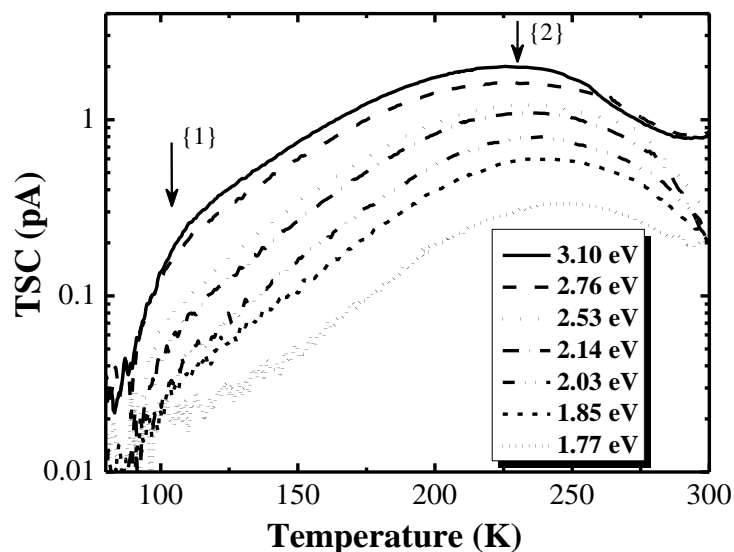
Figure 35. TSC curves with subtracted dark currents depending on the cut-on energies of the long-pass colour filters, as indicated on the Figure. Arrows indicate TSC maxima positions: the maximum {1} is seen as the shoulder on the background of the maximum {2} [A9].

The observed maxima amplitudes due to released charge carriers and their positions are influenced by the optical excitation below and above the band-gap. They are tending to saturate when quantum energy exceeds the band gap. Such a broad TSC spectrum reveals a wide energetic trap distribution in both polymers, implying that there is no single specific structural defect responsible for the trap creation. Moreover, by increasing spectral width of the exciting light the curves are gradually flattening and the peak position is moving towards the lower temperatures, indicating reduction of both the effective activation energy and escape frequency. In Fig. 35 two TSC peaks marked by arrows can be singled out, the first one being superimposed on the second. However, in the material synthetized by the "sulfinyl" route the second TSC maximum at low temperature is less expressed and the main maximum is located at lower temperature, as compared to that synthetized in the "gilch" route.
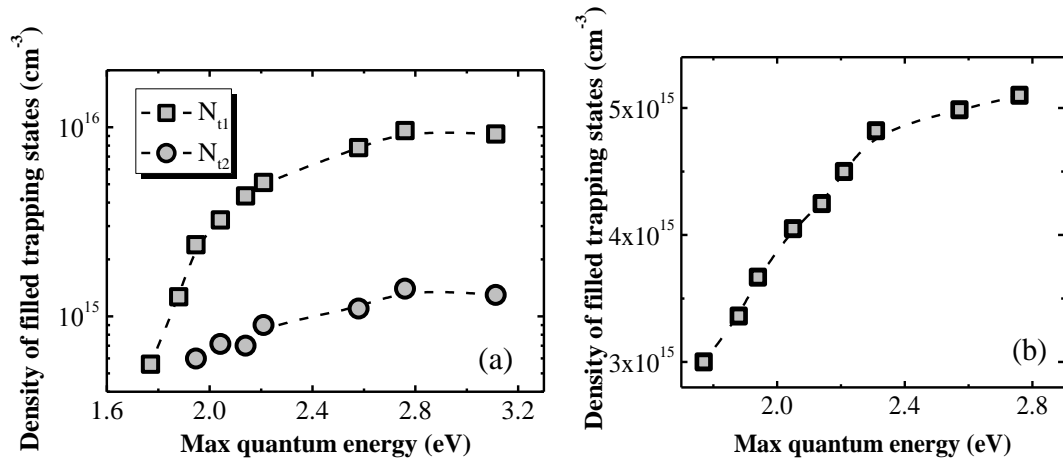
Figure 36. Density of the filled trapping states N_t depending on the exciting light spectral edge in two different samples. (a) "gilch", N_{t1} denotes trap at 0.42 eV, and N_{t2} stands for the trap at 0.22 eV and (b) "sulfinyl" at 0.28 eV.

The density of the filled trapping states N_t calculated from eq. 3.6 is presented depending on the exciting light spectral edge for both levels in Fig. 36. It can be seen that even if the light quanta energy is below the band gap a part of the traps becomes filled. This can be explained by the distribution of states of the band gap edges and that of the trapping states. In this case only the lowest states of the trapping levels will be filled, therefore their activation energy will be higher (Fig. 37). The trap filling and their effective activation energy tend to saturate then the quanta energy exceeds the band gap and absorption increases (Fig. 36, 37).
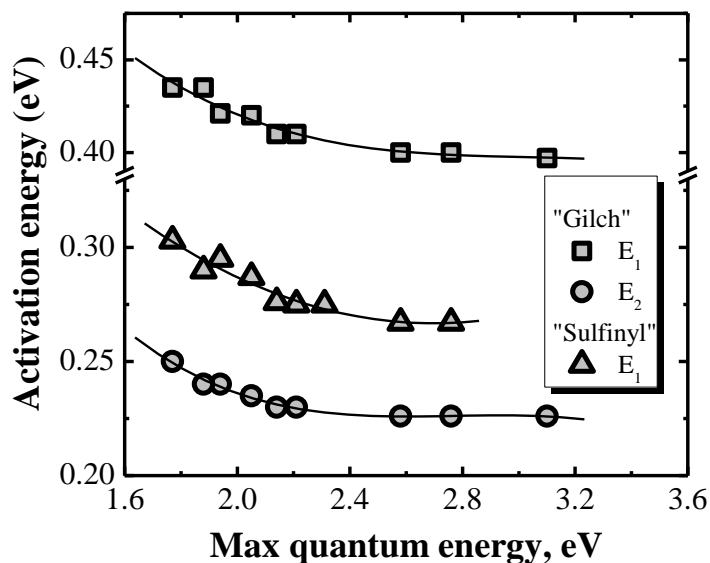
Figure 37. Effective activation energy depending on the exciting light spectral edge. Solid lines are eye-guides.

The saturation values of the effective activation energy of traps are 0.22 eV and 0.40 eV for the "gilch" route synthetized MDMO-PPV polymers and 0.28 eV for the "sulphinyl" route. They coincide with the data of MDMO-PPV [A2] and MEH-PPV [78,79] obtained by TSC. Such activation energies for charge carrier transport were interpreted as hopping mechanism of carriers [80]. Also, TSC measurements with electrical trap filling showed the existence of percolation paths in the polymers [40]. However polymer synthetized in the "sulfinyl" route shows lower activation energies. A lower trap level can be accompanied by an increase in the charge carrier life-time [67]. This implies that both in monomer-unit identical polymers indeed have different densities of electronic defects. Moreover, material synthesized in the "sulfinyl" route does not show typical transient characteristic, which are presented in Fig. 38.
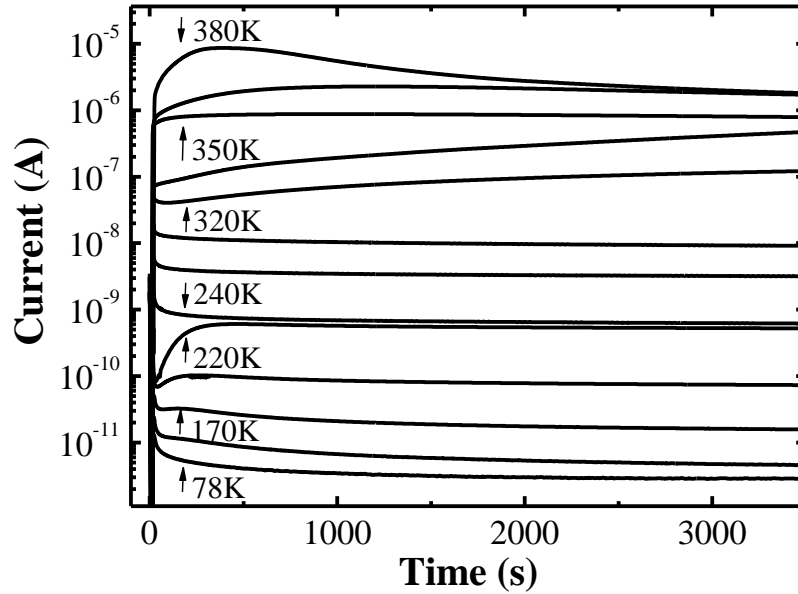
Figure 38. Transient current behavior in MDMO-PPV film (sulfinyl) upon application of the voltage step at different temperatures.

Fig. 38 illustrates current transient behavior in MDMO-PPV sample synthesized in the "sulfinyl" route at different temperatures. The relaxation times necessary to reach 95% of the steady-state values reach several thousand seconds. Characteristically, features of the transients depend on the temperature, indicating effect of the charge distribution affected by traps. E.g., it can be assumed that injected carriers at the temperatures not coinciding with the maxima positions are captured by traps, and this causes gradual decrease of the current. On the other hand the clear increase of the current at the 220 K and 380 K can be associated with the additional charge thermally generated from the traps.

3.3.5. Trap filling depending on the applied electrical field

The trap distribution depending on the applied electrical field has been investigated by applying external electrical field to the sample. The obtained TSC curves are presented in Fig. 39.

75
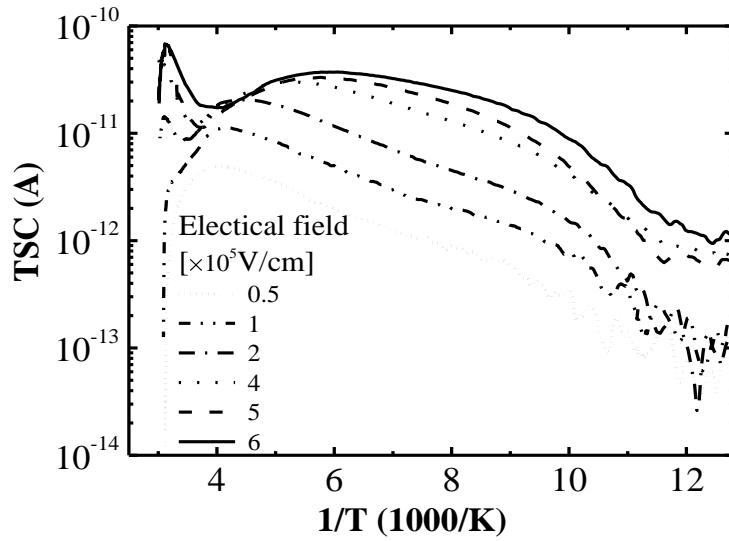
Figure 39. Thermally Stimulated Current curves with subtracted dark currents depending on applied external electrical field.

In Fig. 40 densities of the filled trapping states N_t depending on the effective activation energy E_a are presented as obtained from TSC's by applying external electrical field. The TSC curve was fitted with equation 3.5.
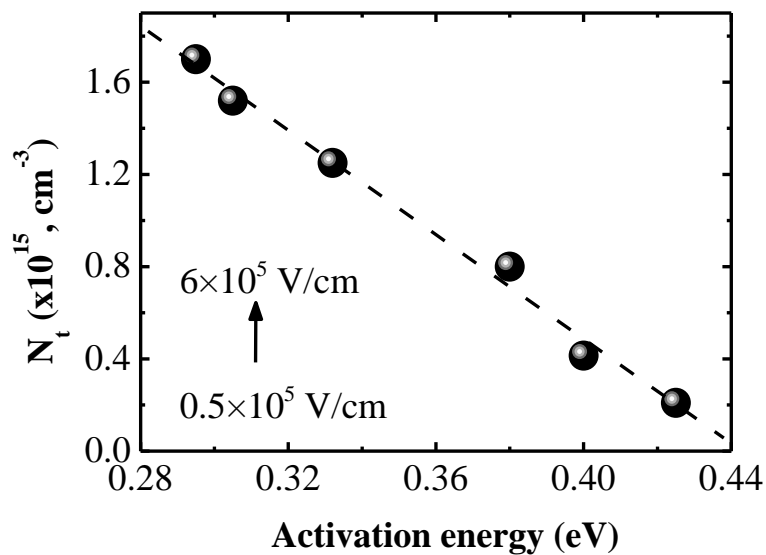
Figure 40. Density of the filled trapping states N_t depending on the effective activation energy E_a as obtained from TSC's by applying the external electrical field [A10].

It can be seen that with increasing electric field strength the effective activation energy values decrease. This can be explained by the fact that the stronger fields bend energy levels, energizing carriers, therefore they can easier escape from the trapping states and potential wells in the bands. Moreover, increasing electrical field improves carrier transport conditions from the contact to more distant sites in the sample by facilitating carrier hopping. This field dependence is widely observed in TSC measurement [81,82] and is in agreement with the field dependence of hole mobility in MEH-PPV as reported in [83]. These results confirm our idea (see in a section 3.2.) proposed for P3HT:PCBM solar cells about the complex role of trapping states in organic materials, i.e., that they are not only trapping carriers, but acting as transport states in the band gap [A6].

3.4. Investigation of electrical and optical properties of DNA functionalized with PEDT-PSS

In this section we report investigations of optical and electrical properties of DNA:PEDT–PSS thin films depending on the temperature and light excitation. The pure DNA is electrically passive material. In order to render it active one has to functionalize it with poly(3,4-ethylene-dioxythiophene) (PEDOT, PEDT) and poly(styrenesulfonate) (PSS) complex. PEDT–PSS is a promising polymer for electronic applications because it is solution processable. When dried, PEDT–PSS coatings have low resistivity, excellent water resistance, and high transmittance of visible light. This enables engineering of the electrical properties of the material.

3.4.1. Samples and experiment

Poly(3,4-ethylenedioxythiophene) and poly(styrenesulfonate) (Fig. 41) aqueous dispersion of the intrinsically conductive polymer PEDT–PSS has been commercialized as the trade mark of BAY-TRON PH 500 being especially homogenized to achieve small size particles.
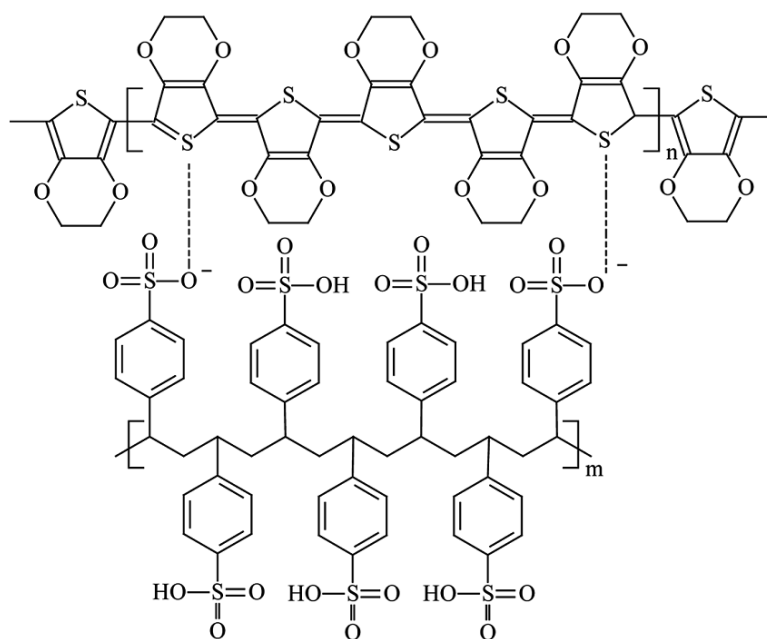
Figure 41. Chemical structure of polymer complex PEDOT-PSS.

The weight ratio of PEDT to PSS is about 1:2.5. This waterborne dispersion is ready to use and can be deposited by spincoating with viscosity maximum 30 mPa·s [A5]. It is tailored to a high conductivity and forms conductive coatings. The coatings are transparent, colourless to bluish; they have good resistance to hydrolysis, good photo stability and good thermal stability, high absorption in the range of 900–2000 nm, no absorption maximum in the visible spectrum up to 800 nm [28].

DNA sodium salts separated from other constituents, extracted from salmon milt and roe were provided by CIST. The procedure leading to obtaining pure DNA includes homogenization, enzyme treatment, protein elimination by controlling the pH level to 7.5, carbon treatment and precipitation by adding acetone. The purified DNA was finally filtered from the acetone and freeze dried [84]. The purified DNA dissolves only in water. It does not dissolve in any organic solvent, except a strong acidic solvent such as trifluo-romethansulfonic acid [85]. The molecular weight measured MW=10^6 Daltons (Da) or 2000 base pairs. The high molecular weight DNA rendered inhomogeneous film thickness due to high solution viscosity. In order to

reduce the viscosity of the DNA-based solutions it was necessary to reduce the mean MW using sonication by ultrasonic procedure to 200 kDa 300 bp and a chain length of 0.1 μm for improved film uniformity and increased poling efficiency [86]. After sonication of DNA (8 g/L) in 18 MΩ·cm deionized water, at 20°C, it was blended using a magnetic stirrer overnight and then DNA solution was added to PEDT–PSS aqueous solution with different volume ratios 1:0.2 and 1:0.5 of DNA:-PEDT–PSS.

The solutions of polymers were spin-coated at 500 or 1200 rpm on the cleaned ITO glass substrates. Immediately after the deposition, the thin films were cured in a 50°C oven in order to eliminate any remaining solvent. The thickness of the thin solid films was measured by profilometer Tencor, ALFA-Step and was found 0.3–1.5 μm. The semi-transparent aluminum contacts were evaporated on the top. Alternatively some samples were deposited on gridded intercalated electrodes initially evaporated on glass substrates.

3.4.2. Optical properties

The UV–VIS–NIR absorption spectra of the studied thin films were measured at room temperature with a Perkin–Elmer UV/VIS/NIR Lambda 19 spectrometer. In Fig. 42 absorption spectrum of the DNA:PEDT–PSS (1:0.5) thin film on the BK7 glass substrates is presented.
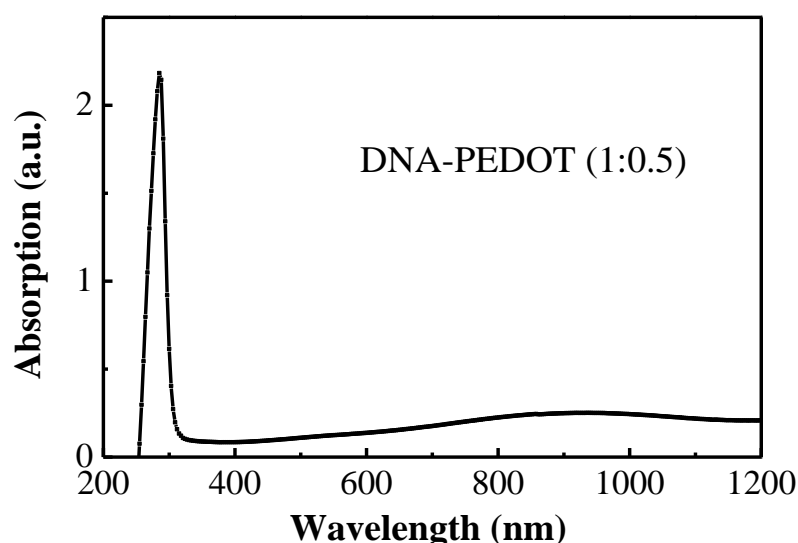
Figure 42. Absorption spectrum of a DNA-PEDOT (1:0.5) thin film [A5].

A strong UV absorption absorption band from 250 to 300 nm is seen. It corresponds to the π–π* transition of electrons of the C=C bond of the DNA bases [87]. Another wide and low absorption band at around 900 nm is associated with the conductive polymer PEDT–PSS [28].

3.4.3. Electrical properties

Sample conductivity at room temperature was in average about $(1 \div 5) \times 10^{-10} \Omega^{-1}$ cm^{-1}, though it could deviate by up to two orders of magnitude even in the samples produced on the same substrate, indicating sensitivity of their properties to the technological conditions, e.g., local uncontrolled variation of the sample doping and/or thicknesses, as the area of the produced layers was relatively big – up to 1.5×1.5 cm^2. The temperature dependences of the film conductivity were measured from 77 K up to 300 K in the dark and upon excitation by the white light from the 100 W halogen lamp. I-V curves were linear and symmetrical down to 78 K temperature as it is shown in Fig. 43.
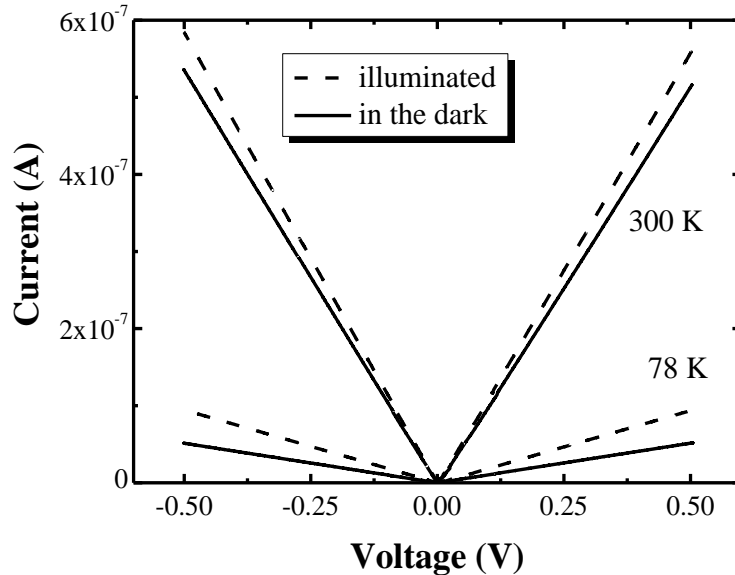
Figure 43. I-V curves of the sample upon illumination by white light (dashed curves) and in the dark (solid lines) at 300 and 78 K as indicated on the figure [A5].

The samples had demonstrated photosensitivity starting from the room temperature down to 78 K. At the room temperature the photosensitivity was about ~10%, and it increased up to a factor of two at the low-temperature. Its dependence on the temperature was quite complex as it will be discussed below.

Characteristically, sample reaction on the applied voltage and light pulses was different: upon application of a voltage step very fast increase of the current was observed, meanwhile the photo-current growth was relatively slow and could be approximated well by the exponential dependence as it is indicated on Fig. 44 by the solid line.
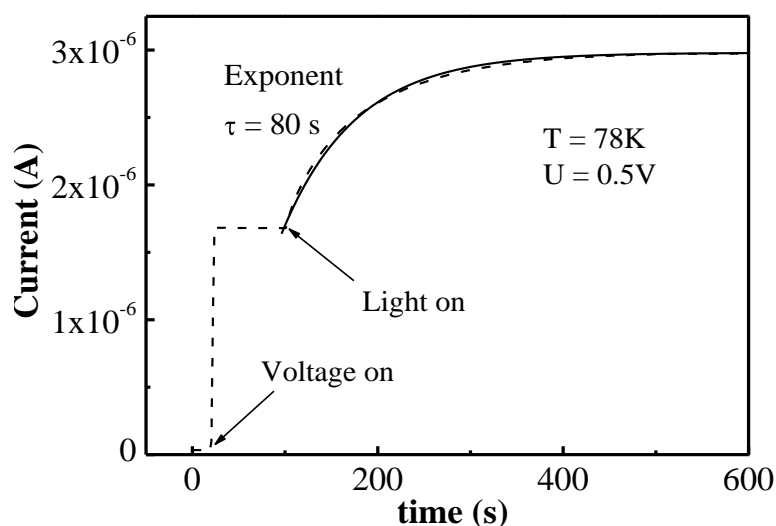
Figure 44. Sample reaction on applied voltage pulse and white light pulse (dashed curve). The photocurrent growth could be approximated well by exponential dependence.

In the present case time constant of the exponential increase was ~80 s, and this value used to shorten with temperature increase. This process still has to be investigated in more detail. Current decay after the light is switched off occurs similarly. This evidences that different carrier transport mechanisms play a role in both cases. Upon application of the voltage pulse fast carrier injection from contacts takes place that is limited by ohmic conduction of the

sample volume. Meanwhile slower light-induced generation of carriers occurs from their transport and/or trapping states.

To investigate carrier transport and thermal generation processes depending on temperature, temperature scans of the dark current were measured (Fig. 45).
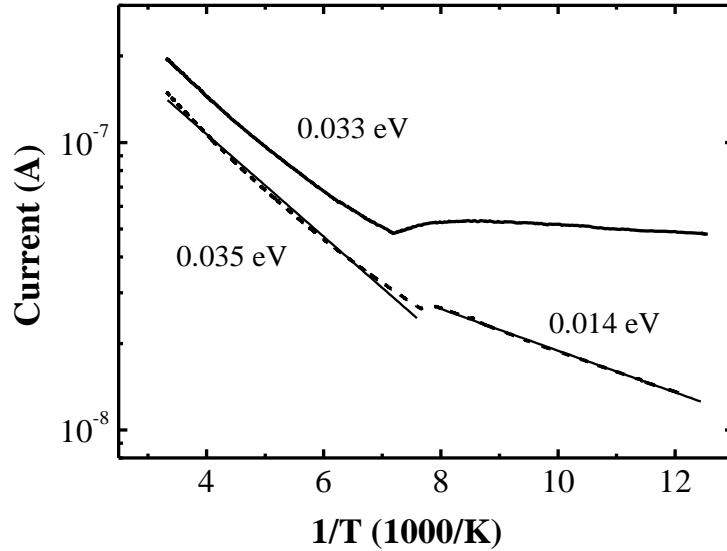
Figure 45. Dark current temperature dependencies in two samples.

It can be seen in Fig. 45, that close to the room temperature their thermal activation energy is about 0.033–0.035 eV. These values were not dependent on the applied bias. Usually thermal activation energy values of DNA varying from 0.18 up to 1.4 eV are reported, depending on material and experimental conditions [88]. Such values are significantly higher than obtained here. This implies that in our samples influence of PEDOT is pronounced, as the conductivity of it is usually high and activation energy close to the room temperature is in meV range [89, 90, 91]. Similar reduction of activation energy down to 0.05 eV was observed in DNA–gold composite in [92].

Below about 130–140 K a characteristic kink appears, and the thermal activation energy drops below 0.014 eV, approaching in some samples zero values. Qualitatively similar trend was observed in DNA–gold composite

because of the change of the charge transport mechanism. At higher temperatures the small polaron hopping model [93, 94, 95] was shown to be applicable. This theory accounts for phonon assistance to electron hopping, and the electrical conductivity is given by:

$$\sigma = \sigma_0 exp\left(-\frac{E_a}{kT}\right).$$ (3.8)

Here E_a is the thermal activation energy of conductivity, T is the temperature and k is the Boltzmann constant. In contrast, in the low-temperature region electrical conductance was shown to proceed according to the Mott variable-range hopping model [95, 96]. According to this model

$$\sigma = \sigma_0 exp\left(-\left(\frac{T_0}{T}\right)^{0.25}\right).$$ (3.9)

To analyze the possible effect of carrier trapping, the Thermally Stimulated Currents was investigated. The TSCs obtained in different samples are shown in Fig. 46.
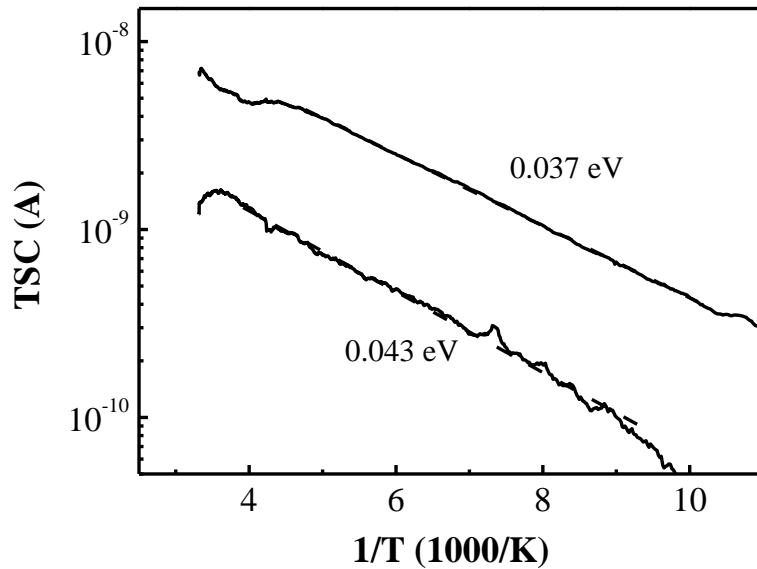
Figure 46. TSC scans in two samples, measured at 0.5 V applied bias after the white light excitation (solid curves). Dashed curves indicate linear fits in Arrhenius scaling [A5].

Characteristically, TSCs are low as compared with both dark current and current after the light excitation. This indicates that relatively small number of carriers becomes trapped, and most of them recombine after the light excitation is turned off. Nevertheless nearly the same activation energy values of about 0.036–0.043 eV were evaluated in a wider temperature region as compared to the dark currents. Such low activation energy values confirm that current increase is related to transport phenomena, rather than change of the carrier density because of their thermal generation, i.e., it could be given by the growth of carrier mobility as described above. This assumption is realistic by having in mind complicated hopping transport character in disordered organic materials. Therefore evaluated activation energies could probably reflect the energetic spread in the charge transporting levels, resulting in distribution of the density of transporting states.

In Fig. 47, the dark current and photocurrent temperature dependencies are presented.
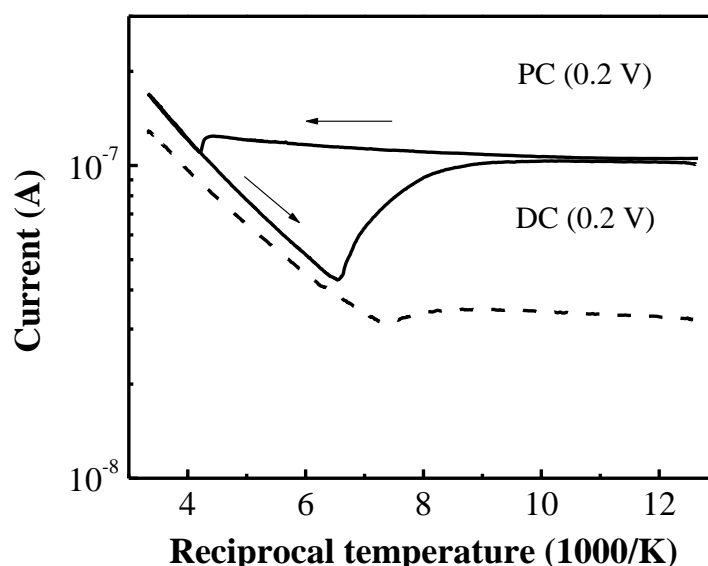
Figure 47. Temperature dependencies of the photocurrent (PC – solid curves), upon scanning the temperature down and up as indicated by arrows and the dark current (DC – dashed curves) at 0.2 V bias and without any applied bias [A5].

As it was mentioned above a characteristic kink was observed in dark the current measurement that becomes even more expressed upon light excitation. By lowering the temperature the photocurrent starts growing at 145–155 K and reaches saturation level that is by a factor of about 2–2.5 higher than that of the minimum. Afterwards, by increasing the temperature, the photocurrent does not change up to 235–245 K, forming a "bistable" loop. This behaviour does not depend on the bias, indicating that the effect is light-induced. This is supported by the fact that sample reaction on the voltage and light pulses was different: upon application of a voltage step very fast increase of the current was observed, meanwhile the photocurrent growth was slow [97].

This evidences effect of different mechanisms. Upon application of the voltage pulse fast carrier injection from contacts takes place that is limited by ohmic conduction of the sample volume. Meanwhile slower light-induced generation of carriers occurs from their transport and/or trapping states.

The behaviour of the current by scanning the temperature upon pulsed illumination of the samples is presented in Fig. 48.
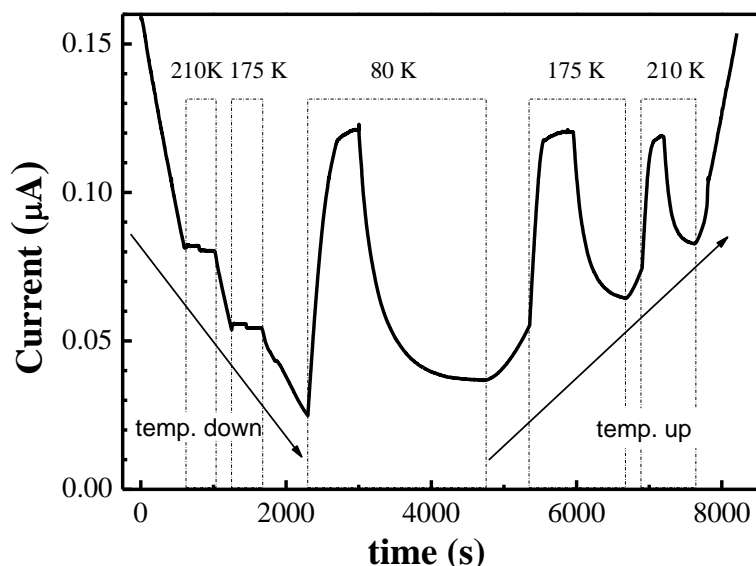
Figure 48. Change of the current upon variation of the temperature and pulsed illumination of the sample. The temperature was stabilized at 210 K, 175 K, and at 80 K, as indicated by the dashed-dotted rectangles. At these points the sample was excited by the white light pulses.

The temperature was stabilized at 210 K, 175 K, i.e., within the bistable loop, and at 80 K. At these points the sample was excited by the light pulses. In Fig. 49 behavior of the relative photo-conductivity $\frac{I_{light} - I_{dark}}{I_{dark}}$ is presented. Upon cooling down to the kink point, the photosensitivity remains low. At the temperatures below this point the photocurrent increases significantly, moreover, its maximum reaches the same value upon heating the sample (Fig. 48). Meanwhile the relative photoconductivity reaches ≈ 0.7 at 80 K (Fig. 49).
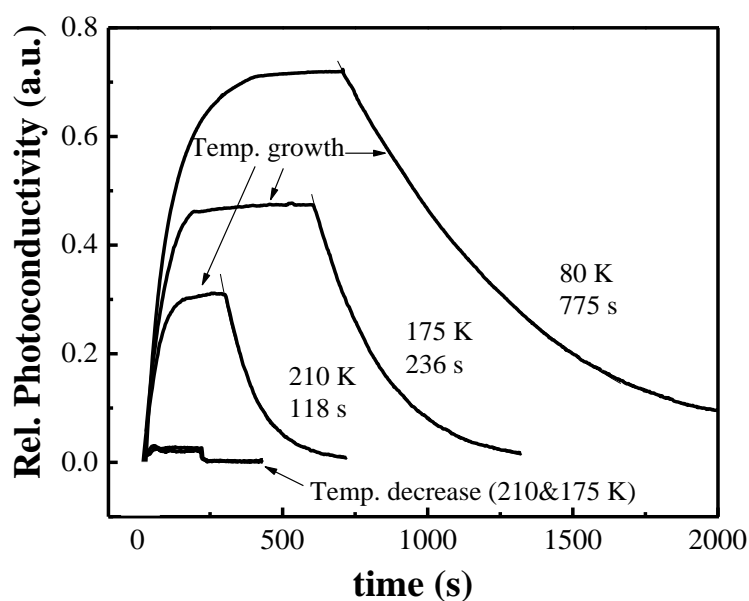
Figure 49. Kinetics of the relative photoconductivity upon excitation of the sample by the white light pulse at different temperatures by cooling and heating.

The photocurrent upon illumination increases much faster than it drops after the light is turned off, though both processes could be approximated by the single exponents. This indicates the complex effect that cannot be attributed to the simple model, e.g., carrier generation from single trapping centers. The long relaxation "tails" indicate appearance of the persistent photoconductivity phenomenon [98]. This phenomenon is associated with the inability of the light-generated carriers to recombine, as they become trapped in the spatially separated potential wells and hills of the band gap edges in the disordered structure. Upon heating the sample relaxation times used to shorten

86

as indicated in Fig. 49. Characteristically, amplitudes of the relative photoconductivity had followed qualitatively similar behavior.

Therefore the bistability of photoconductivity could probably be attributed to the light-induced morphology changes of the samples, resulting in an increase of photosensitivity at low temperatures. To explain this effect several mechanisms can be accounted for. First of all, it is known that an anisotropic conductivity is characteristic for PEDT–PSS thin films [90]. So, one can suppose that light excitation could energize molecular movements of PEDT–PSS, changing in this way the pre-dominant orientation of PSS lamellas. The light-induced variation of PEDOT conjugation lengths was reported in [99]. Another possible mechanism could be variation of the transition temperature at which change of the transport mechanism occurs as described above. This could be assisted by the light-induced changing of the density of hopping states, because of their filling by generated carriers.

3.5. Investigation of the linear and nonlinear optical properties of DNA-Silica-Rhodamine thin films

In this section the investigation will be presented of the linear and nonlinear optical properties of DNA–Silica–Rhodamine thin films, as they are promising systems for the optical waveguide applications. The thin films were characterized by means of UV-VIS spectroscopy and Third Harmonic Generation (THG) measurements. All experiments were performed at room temperature.

3.5.1. Samples preparation

The DNA–Silica materials were prepared using DNA aqueous solutions of 1.0 mg/mL with different Rhodamine dye (Rh) concentrations (Table 1), by using Water/TX – 114/Pinus Oil microemulsion system as template.

Table 1. Compositions of the DNA – silica materials [A11].

Microemulsion system	Symbol	DNA	Rhodamine
Water/TX – 114/Pinus Oil/TEOS pH = 4	SiO2-Rh	-	
	1		0.060%
	2		0.030%
	3		0.007%
	SiO2-DNA-Rh	0.15%	
	1		0.060%
	2		0.030%
	3		0.007%

The DNA-silica thin films were directly synthesized by microemulsion assisted sol–gel dip-coating on glass substrates. The thickness of the films has been in all cases precisely measured by means of a micrometer. The thickness was in all cases found to be around 0.3 mm, while small deviations, which were unavoidable with the aforementioned preparation technique, have been taken into account during the analysis of the experimental results for the determination of the nonlinear optical parameters. The detailed experimental synthesis procedure was described elsewhere [100]. In short, the DNA/water solution was solubilized in a water/oil microemulsion through vigorous stirring and then was encapsulated into a silica matrix in acidic media. These hybrid materials were water-insoluble. This approach is unique as compared to the conventional methods involving adsorption on glass surface, entrapment in polymer matrix or impregnation in porous glass powders, because entrapment is based on the forming of the silica network around the functional molecules within the microemulsions colloidal aggregates.

3.5.2. Transmittance UV–Vis and fluorescence measurements

The structural characterizations of DNA – silica materials, thin films, done by transmittance UV – VIS measurements. The spectra obtained with a JASCO V–550 Spectrophotometer equipped with an integrating sphere. Fluorescence spectra of the samples were recorded at a wavelength between

300 and 800 nm using a Jasco FP-6500 Spectrofluorometer. The transmission and fluorescence spectra were done on films obtained in the same way, by casting on similar supports. The transmittance spectra are presented in Fig. 50.
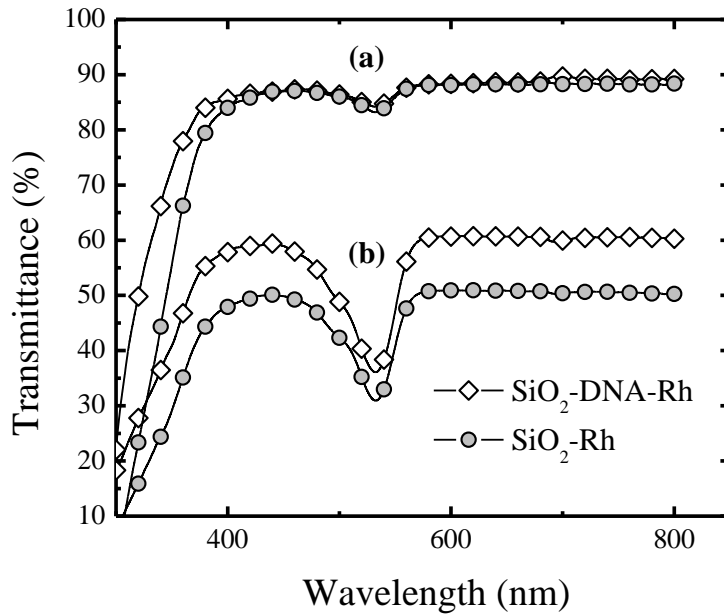
Figure 50. UV–Vis transmittance spectra of thin films, exhibiting low – 0.007 % (a) and higher – 0.060 % (b) concentration of the dye [A11].

The absorption maximum at 532 nm confirms the presence of Rhodamine, homogeneously distributed in the silica or DNA-silica matrices. The same absorption maximum was observed in DNA doped Rhodamine 6G (Rh6G) solution in polyvinyl alcohol [101]. The maximum between 530–540 nm corresponds to absorption by the free Rh monomer [102]. The curves indicated as (a) and (b) in Fig. 50 correspond to 0.007% and 0.060% concentration of dye respectively. It is obvious that by increasing the dye concentration the transparency of the films is reduced. However, the presence of DNA slightly improves their transparency as it can be seen in the same figures. This may be explained by the location of the dye molecules. When small dye concentrations are used, the molecules are located in the DNA groves. On the contrary at high concentrations, they appear in the DNA groves but they are also associated with the surfactant oxyethilenic groups. Moreover

in the DNA presence, the dye molecule could be distributed between the micelles core and DNA groves, avoiding their aggregation, which means that these DNA-based materials appear to be more homogeneous in terms of dye molecules distribution into the matrix.
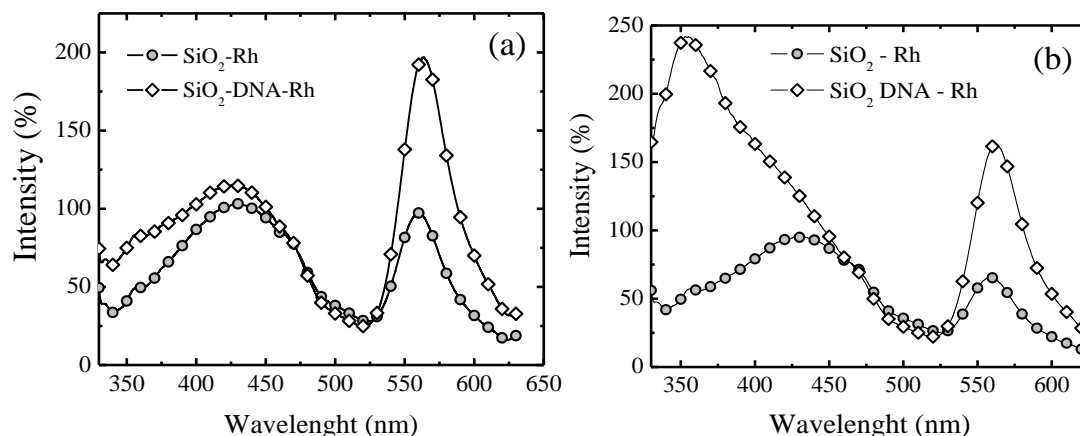
Figure 51. Fluorescence spectra of the Rhodamine-silica thin films in absence / presence of DNA. The excitation wavelength was at 524 nm. a. high; b. small concentration [A11].

Intensification of the fluorescence lines shown in Fig. 51 also support this conclusion. In many cases, the dyes act as fluorescent labels for bio-molecules, and can interact with the bio-molecule either through covalent or non-covalent bonding. Moreover, fluorescence dyes, that bind to double helical DNA by intercalation or groove binding, reduce the fluorescence quenching caused by aggregation [29,103] or the rate of the non-radiative transitions from the excited state [104].

In Fig. 51 shown the new fluorescence band centered at 425 nm, being common to all the Silica-Rhodamine samples, with or without DNA, could be assessed to an association complex between surfactant (Triton X-100) and dye molecules [105]. The sharp peak observed at 350 nm appeared in low concentration range of Rhodamine (Fig. 51 b) could be attributed to fluorescence of aromatic surfactant. Its presence could be noticed as a shoulder in all the other spectra, but only in this case it appears as a well resolved band.

90

Such a behavior could be explained by a preferential location of dye molecules within double strand DNA [100].

3.5.3. Third harmonic generation measurements

The NLO properties of the films were analyzed by the third harmonic generation technique. The measurements were performed in the air by the Maker fringes technique [46], using a diode pumped passively mode-locked Nd:YVO$_4$ laser, working at 1064 nm with 30 ps pulse duration and 10 Hz repetition rate. A fused silica plate was used as a reference material for the THG measurements, due to the well-known nonlinear susceptibility it exhibits ($\chi_{silica}^{(3)} = 2.0 \times 10^{-22} \, m^2/V^2$) [106]. The advantage of the THG technique is that it provides information related only with the electronic contribution to the nonlinearity ($\chi_{elec}^{(3)}$), while it is not affected by other contributions (e.g. rotational, redistribution etc.).

For the investigation of the nonlinear optical response, several Maker fringes patterns have been recorded. In order to characterize the nonlinear optical parameters the experimental data have been analyzed, taking into account also the significant harmonic absorption loss, (Fig. 50) using the procedure described elsewhere [16, 107, 108]. Also is important to mention, there is no chemical interaction between materials components.

The THG measurements have yielded interesting results. The samples have been found to be THG efficient, while the nonlinear optical signal was highly dependent upon the angle of incidence of the laser beam with respect to the sample, resulting to Maker fringes patterns. In Fig. 52 characteristic experimental curves corresponding to the Silica-Rh and Silica-DNA-Rh samples, obtained under the same experimental conditions, are presented.
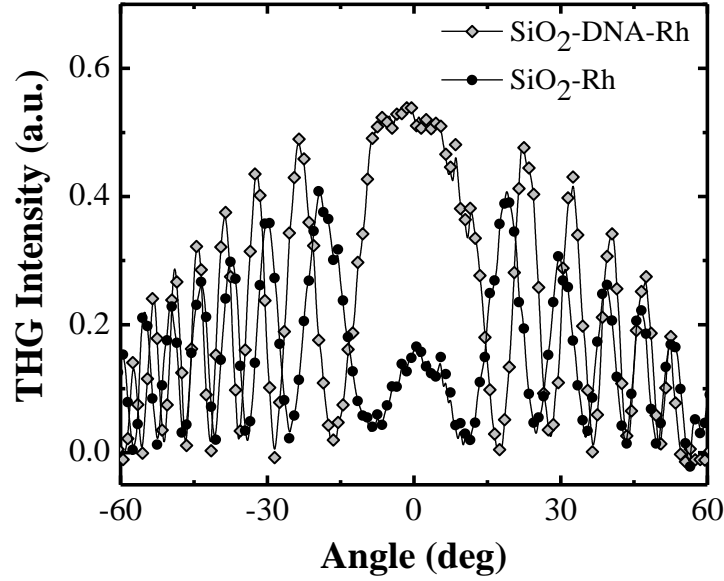
Figure 52. An example of the THG Maker fringes signals as a function of the incident angle in the case of the Silica-Rh and Silica-DNA-Rh systems [A11].

The period of the Maker-fringes patterns has been found to be directly dependent upon the sample thickness as expected. The structure of samples is based on the self-assembling of surfactant molecules at water-oil interface, being able to protect DNA strands into the core micelles, keeping its natural structure and properties.

In Table 2 the nonlinear optical parameters of the investigated compounds can be seen. For comparison the response of fused silica is also added in the same table. The $\chi_{elec}^{(3)}$ values obtained for the films are higher than that of fused silica by about a factor of 6 and 3 for the DNA-doped and the non-doped samples respectively.

Table 2. Third order nonlinear susceptibility values for the investigated compounds [A11].

Sample	Thickness (10^{-2} cm)	$\chi_{elec}^{(3)}$ ($\times 10^{-22}$ m^2/V^{-2})
SiO$_2$-DNA (0.15%)-Rh (0.007%)	3.4	12.5 ± 0.2
SiO$_2$-Rh (0.007%)	3.0	5.6 ± 0.1
Fused Silica	0.1	2.0

However, it is very important that the Silica-DNA-Rh films exhibits significantly higher third order nonlinear susceptibility then the Silica-Rh films. As it can be seen from the same table the increase of the $\chi^{(3)}_{elec}$ in the case of the sample exhibiting 0.007 % concentration of Rh and 0.15 % of DNA is higher than 100% if we compare with the non-doped system. This enhancement of the nonlinear optical response, related to the presence of the DNA can be attributed to the increase of the charge transfer, which takes place in the system and is due to the many highly polarizable conjugated π−electrons in DNA [97] and also in Rh6G-PVA-DNA [101]. Moreover, the interactions due to intercalation into the base pair stack at the core of the double helix, and/or insertion into the minor groove of DNA is well known to have strong impact on the optical characteristics of organic dyes.

3.6. Investigation of DNA complex with new ionic surfactants

In this section new functionalities for nonlinear optical applications of bio-molecular systems will be illustrated. DNA complex with new ionic surfactants were studied. These surfactants enabled DNA solubility in solvents other than alcohols, like aromatic and chlorinated ones. Composites with two NLO active dyes are subjects of the second and third harmonic generation experiments. The found effective nonlinear susceptibilities values are much higher than that for standard fused silica. Meanwhile no influence of the surfactant on NLO properties was identified.

3.6.1. Sample preparation

DNA and its complexes are materials of low optical losses comparable or even lower than that of PMMA [86], what is required for a matrix material in composites with optically active molecules. The best quality films were obtained from DNA complex with cetyltrimethylammonium [109,110] (CTMA) Fig. 53 (a).
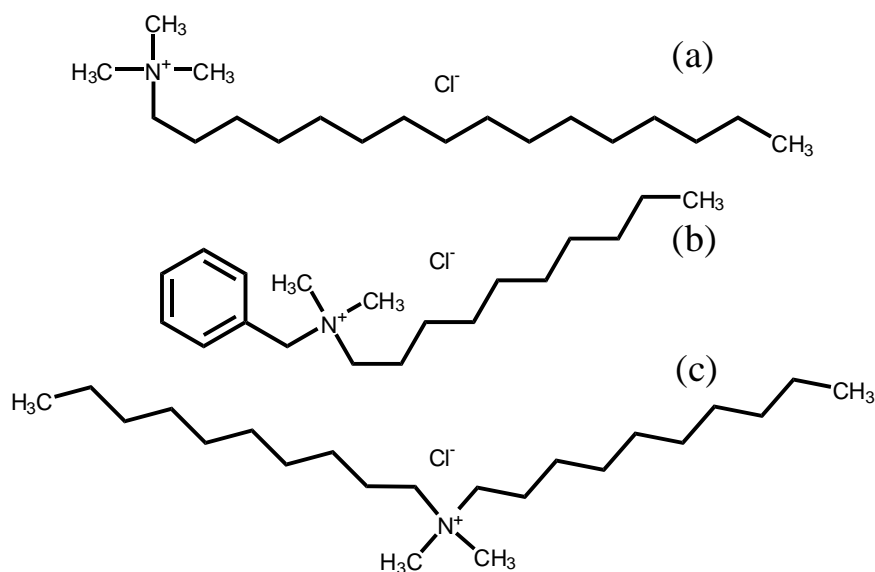
Figure 53. Surfactants structures CTMA- cetyltrimethylammonium (a), BA-benzalkonium chloride (b), DDCA- didecyldimethylammonium chloride (c) [A12].

Despite the success of DNA-CTMA there is still need for new cationic surfactants which would extend the range of available solvents for DNA complex. In these experiments tests of two such candidates – benzalkonium chloride (BA) Fig. 53 (b) and didecyldimethylammonium chloride (DDCA) Fig. 53 (c) – are described.

DNA complexes were prepared according to the procedure adapted from Wang *et al* [111]. It was found that both complexes regarding the solubility were superior over classical DNA-CTMA. Composites of DNA complexes and original push-pull dyes, belonging to azo-carbazole family were prepared by co-solution in DMF, common solvent for both constituents. The detailed synthetic routine of such compounds has been described in [112] and schematic structures of these dyes are pictured in Fig. 54.
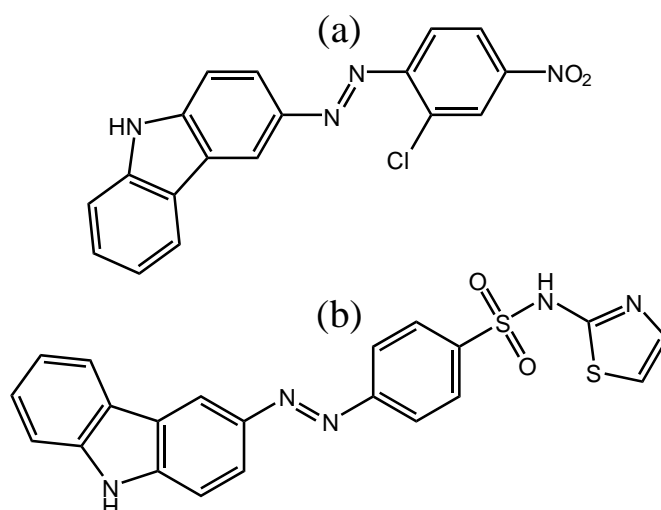
Figure 54. Chemical structure of original dyes. (a) 4-(9H-carbazol-3-ylazo)-3-chloro-N,N-dihydroxy-aniline [Dye1], (b) 4-(9H-carbazol-3-ylazo)-N-thiazol-2-yl-benzenesulfonamide [Dye2] [A12].

The dyes were supposed to be different regarding their nonlinear optical properties due to the strength of acceptor groups attached through azo- bond to electron accepting carbazole moiety (stronger in the case of Dye1). The samples were produced by drop casting on the glass plates cleaned according to RCA-1 recipe and afterwards were baked on the glass plates at 200°C. Samples contained c.a. 10% wt. of the dyes. Three groups of thin films were prepared, consisting of Dye1/DNA-DDCA, Dye1/DNA-BA and Dye2/DNA-BA ([Dye1] is 4-(9H-carbazol-3-ylazo)-3-chloro-N,N-dihydroxy-aniline, and [Dye2] is 4-(9H-carbazol-3-ylazo)-N-thiazol-2-yl-benzenesulfonamide).

3.6.2. Absorption spectra of materials

The UV-Vis spectra of these materials are presented in Fig. 55.
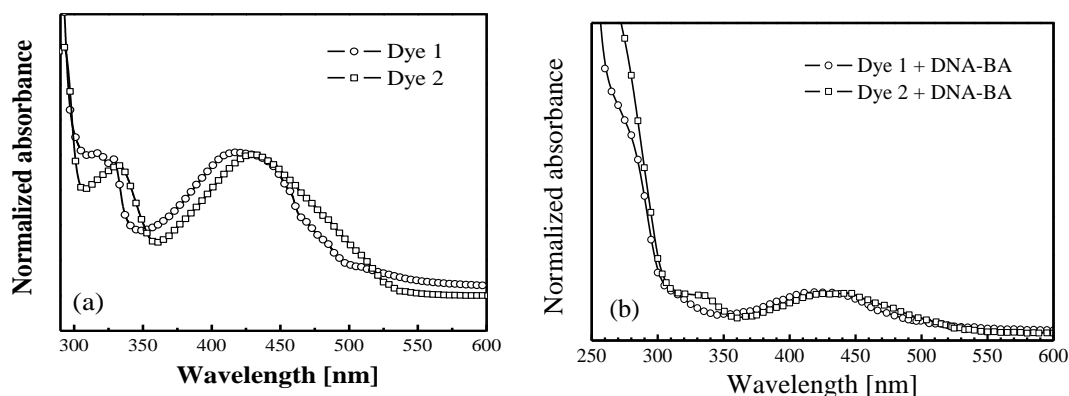
Figure 55. The absorption spectra of Dyes (a) and Dyes with DNA complexes (b).

Below the lower wavelength limit all the samples were optically transparent at least down to 1700 nm, what was the detection limit of the used instrument. The samples for spectroscopic studies were prepared on quartz slides from much diluted stock solutions to obtain films of absorption not exceeding the dynamic range of the used spectrometer. Fig. 55 (a) represents spectra characteristic of pure dyes dissolved in dioxane, while the fig. 55 (b) one pictures data measured for blends consisting of a dye and DNA-BA complex. In the picture one can see that blending these dyes with DNA-complex didn't change substantially the shape of the spectra. However, a slight bathochromic shift by c.a. 5 nm was observed in both cases accompanied by a minor broadening of the main absorption peaks. Apart from this, it seems that DNA complex does not modify substantially the absorption of the studied dyes at least in the wavelength span where DNA-complex is transparent (i.e below c.a. 300nm). As can be seen, in UV-B and UV-C absorption of dyes is screened by DNA.

Similar data were obtained in the case when DNA-DDCA was applied as matrix.

3.6.3. Nonlinear optical measurements and analysis

The nonlinear response was characterized by the optical second (SHG) and third harmonic generation (THG) technique.

The effective nonlinear susceptibilities of thin films were obtained in air by the Maker fringes technique [46]. The experimental analysis of the second order susceptibilities was calculated by comparison with the SHG intensity of a standard 0.5 mm thick Y-cut quartz crystal plate [113, 114, 115]. The simplified model of Lee *et al* [48, A7] was used.

$$\chi^{\langle 2 \rangle} = \chi_q^{\langle 2 \rangle} \frac{2}{\pi} \frac{l_{c,q}}{d} \left(\frac{I^{2\omega}}{I^{\omega}} \right)^{1/2} ,$$

(3.10)

Here $\chi^{(2)}$ and $\chi_q^{(2)}$ denote second-order nonlinear susceptibilities of the studied material and quartz [106] ($\chi_q^{(2)} = 1.0$ pmV^{-1}), respectively, $I^{2\omega}$ and $I^{2\omega}{}_q$ are the second harmonic intensities, d – thickness of thin film. More details are presented in previous work [108].

For THG data analysis usually three theoretical models are used, suggested by Kubodera *et al* [54,116], Reintjes [21] and Kajzar *et al* [52]. The first relative method is based on comparison with a reference sample measured under identical conditions. It can be applied for the thin film of amorphous material the thickness of which d is much smaller than the coherence length $l_{c,s}$ of the reference material. In our case d is comparable with $l_{c,s}$, therefore *Reintjes* and *Kajzar* models were chosen.

The THG intensities were calibrated with THG measurements on a high purity fused silica slab, performed under the same conditions.

The Second Harmonic Generation and Third Harmonic Generation Maker fringes pattern measurements have been carried out in transmission mode. The intensity and the polarization of the fundamental beam (1064 nm) exciting the sample were adjusted by a half wave plate and a polarizer. The second/third harmonic light was detected by a photomultiplier and data were recorded depending on the precisely controlled incidence angle. SHG Maker fringes measurements have been done for both *p* and *s* polarizations. Characteristic experimental curves are shown in Fig. 56.
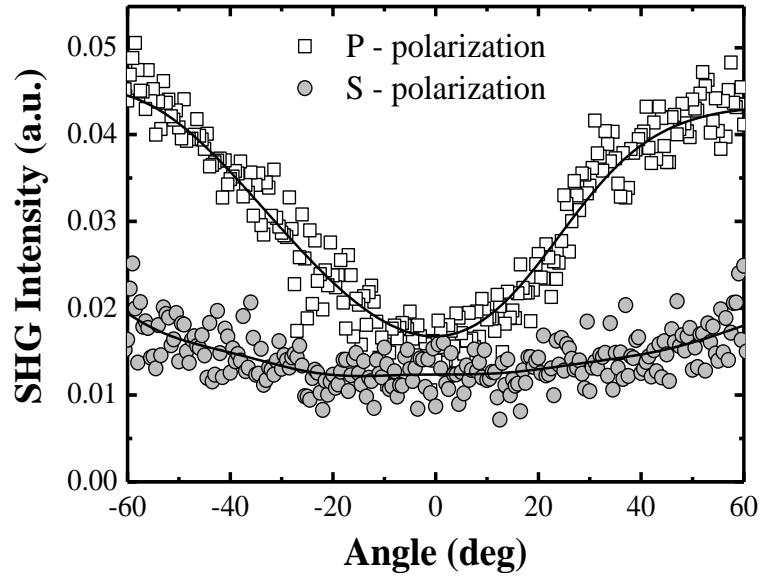
Figure 56. An example SHG signal of Dye1/DNA-DDCA is in p and s polarization [A12].

The SHG signal was very weak comparing to the reference quartz. The effective $\chi^{(2)}$ values have been found to be 0.011 pm/V and 0.003 pm/V for *p* and *s* polarization in the case of Dye1 and Dye2, respectively. THG Maker fringes measurements were taken for three samples of each group and used *s-s* and *p-p* polarization configurations. The high THG intensity as a function of the angle of incidence was observed in all samples and it can be seen in Fig. 57.
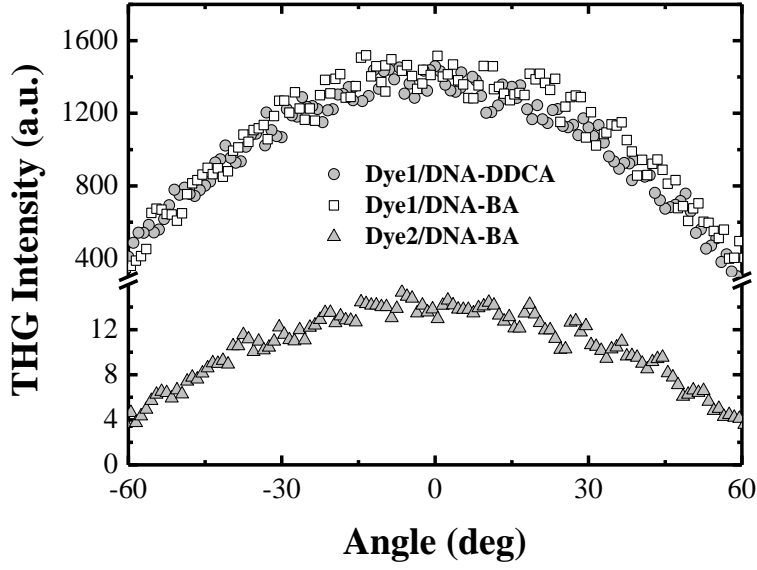
Figure 57. An example of THG Maker fringes signal as a function of the incidence angle in s polarization [A12].

A negligible difference has been found between the experimental data obtained for *s-s* and *p-p* polarizations. In order to calculate precise values of the electronic contribution of $\chi_{elec}^{(3)}$ susceptibility [117], the THG experimental data were fitted with the formulas derived by *Reintjes* [21] and *Kajzar* [53].

$$I_{3\omega} = \frac{576\pi^6}{n_{3\omega}n_{\omega}^3\lambda_{\omega}^2c^2}\left|\chi^3\right|^2 I_{\omega}^3 L^2 \left(\sin\left(\frac{\Delta kL}{2} \right) \middle/ \frac{\Delta kL}{2} \right)^2 \tag{3.11}$$

and

$$I^{3\omega} = \frac{64\pi^4}{c^2}\left|\frac{\chi^3}{\Delta\varepsilon}\right|_s (I^{\omega})^3 \left| e^{i(\psi_s^{3\omega}+\psi_f^{\omega})}\left[T_1 \ e^{i\Delta\psi_s} - 1 + \rho e^{i\phi}T_2(1-e^{-i\Delta\psi_f}) \right] + C_{air} \right|^2 \tag{3.12}$$

The results of the numerical procedure are pictured by the solid lines in Fig. 58.
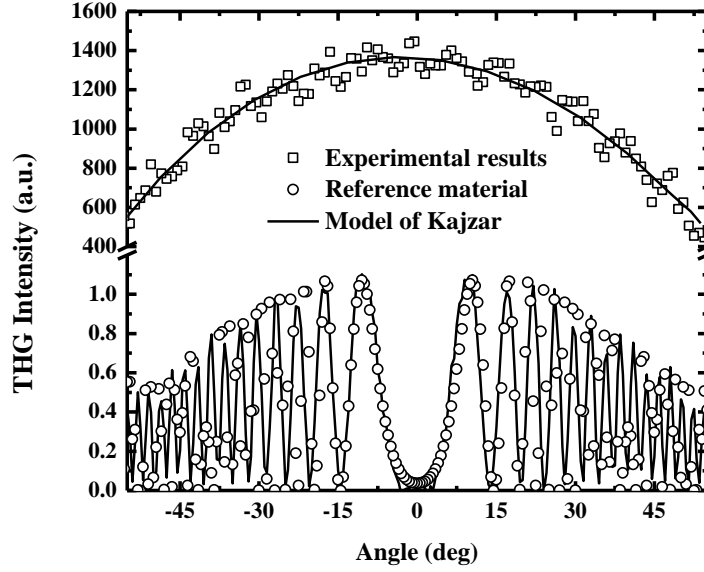
Figure 58. An example of THG Maker fringes of Dye1/DNA-DDCA (square) in s polarization and of reference material (circle) and fitted (solid line) curve [A12].

The third order nonlinear susceptibility for both polarizations was the same within the experimental errors. The determined effective $\chi^{(3)}_{elec}$ value for two theoretical models is listed in Table 3.

Table 3. Comparison of the $\chi^{(3)}_{elec}$ values in different samples [A12].

Model Sample	Rentjes $\chi^{(3)}_{elec}$ $(\times 10^{-21}\ m^2\ V^2)$	Kajzar $\chi^{(3)}_{elec}$ $(\times 10^{-21}\ m^2\ V^2)$
Fused Silica	0.2	
Dye1/DNA-DDCA	17.0 ± 1.9	15.0 ± 1.0
Dye1/DNA-BA	19.0 ± 1.8	17.0 ± 0.9
Dye2/DNA-BA	1.9 ± 0.2	1.8 ± 0.1

The $\chi^{(3)}_{elec}$ values of the sample Dye2/DNA-BA are one order of magnitude higher than that of the fused silica [106] used as reference in THG experiment, whereas for the samples Dye1/DNA-DDCA and Dye1/DNA-BA they are two orders of magnitude higher than in the fused silica. Moreover these values (Dye1/DNA-DDCA and Dye1/DNA-BA) are about 5 times higher

than reported in previous paper [118] for Dye1 dispersed in cured epoxy resin and more than 1.5 times higher in [119]. This fact can be attributed to a better dispersion of Dye1 molecules confined in DNA-surfactant matrix, which prevents dye molecules from aggregating. Azo-carbazoles like majority of efficient NLO dyes have strong tendency to crystallize in the matrix. Crystallites (or other aggregates) are of micrometer size (or smaller) so cannot be observed through transmission optical microscopy. Since they are not necessarily "true" crystals producing well developed X-ray diffraction peaks, their presence is most often is a subject of speculations.

In the case of Rentjes model values of cubic susceptibility are higher as compared with Kajzar model, though the last one is more precise, as it takes into account contributions both of the substrate and the air. This is important condition is neglected sometimes [116].

4. Concluding Summary

1. The functionalized soluble poly(p-phenylenevinylene) (PPV) grafted with push–pull like molecules were purposefully syntehsized to investigate the molecular orientation concept for photovoltaic applications. The grafting of the push–pull molecule with a donor/transmitter/acceptor structure, possessing a large ground state dipole momentum, enables the efficient molecular orientation by a DC-electric field. The effect of orientation of the polar molecules on the carrier injection and transport properties was evidenced by the current–voltage characteristics and mobility measurements using the CELIV method. Upon orientation in forward direction increase of the external quantum efficiency by the factor of up to 1.5 − 2.0 was demonstrated. It is associated with the growth of the mobility, resulting also in the increase of the device current. In contrast, orientation in the reverse direction resulted in the drop of mobility, device current and external quantum efficiency. These effects were reversible and repeatable during the orientation/ disorientation cycles of the polar molecules.

2. Charge transport and trapping phenomena were analyzed in bulk-heterojunction structures of P3HT and PCBM that are promising for the development of organic solar cells. Current–Voltage characterization was used to investigate carrier injection properties, carrier traps were analyzed by the Thermally Stimulated Current spectroscopy, and Carrier mobility measurements were performed by the CELIV method. The energy conversion efficiency of the devices was 3.7 per cent and the fill factor of the I-V characteristics was up to 68 per cent. Despite such relatively good parameters, carrier trapping was demonstrated to be effectively involved in the transport phenomena. The evaluated trapping state activation energy was about 0.62 eV and their density reached up to $10^{17} − 10^{18}$ cm^{-3}. At such high density these states may probably act as transport states, limiting

carrier mobility. The results were analyzed numerically by taking into account carrier thermal generation from the trap states as well as mobility variation according to the Gaussian disorder model. The mobility parameters evaluated from the TSC and obtained by direct mobility measurements were coinciding well, thus evidencing that carrier trapping is among the main factors, determining their mobility behaviour.

3. The thermally stimulated current depending on the spectral range of the exciting light and applied electrical field was investigated in MDMO-PPV films synthesized in two different routes "gilch" and "sulfinyl". The results are a direct indication by the photo-thermo-electrical methods of the distribution of energy-trapping states. It was demonstrated that two traps with the Gaussian distribution of the states and effective mean activation energies of about 0.22 and 0.40 eV are prevailing for "gilch" route synthetized MDMO-PPV polymers and 0.28 eV for "sulfinyl" route. A lower traps level can be accompanied by an increase in the charge carrier life-time. The results indicate that these two in monomer-unit identical polymers indeed have a different density of electronic defects. The standard deviations of the distributions were evaluated to be 70–100 meV. The trap-filling and charge-generation processes were shown to be dependent on the excitation wavelength and applied electric field. By changing the excitation spectral range the thermal activation energy values varied due to different filling of the distribution of energy scale states. The higher electric fields reduce carrier activation energy because of the decreased potential barrier heights.

4. The conductivity of DNA:PEDT–PSS thin films at room temperature was in average about $(1–5) \times 10^{-10} \, \Omega^{-1} cm^{-1}$, though it could deviate by up to two orders of magnitude even in the samples produced on the same glass substrate indicating sensitivity of their properties to the technological conditions. I-V curves were linear and symmetrical down to LN

temperature. The thermal activation energy of the dark conduction near the room temperature was about 0.033 eV and it did not depend on the applied bias. The weakly expressed carrier trapping was identified by the Thermally Stimulated Current method, what proves the fast recombination and/or re-trapping of light generated carriers. The ''bistable'' photoconduction behavior below the room temperature was evidenced at constant light excitation, i.e., a notable increase of the photocurrent could be observed below 140–160 K by cooling the samples. Meanwhile by heating the photosensitivity remained increased up to 230–240 K. Most probably such phenomenon could be attributed to the light-induced morphology changes of the samples and/or varying charge transport conditions.

5. The linear and nonlinear optical properties of DNA-Silica-Rhodamine samples were analyzed. It was demonstrated that even low concentrations of DNA bio-molecules of about 0.15% can affect the aggregate behavior of the dyes in silica materials, resulting in enhancement of both the linear and nonlinear optical properties of the systems. More specifically, the addition of DNA was found to result in higher transmittance and fluorescence efficiency, as well as significantly higher third order nonlinearity. Thus, silica materials are suitable matrices for double helix of DNA molecules mixed with the optical dyes and enable engineering of active optical waveguide materials with enhanced optical properties.

6. The series of bio-organic samples (Dye1/DNA-DDCA, Dye1/DNA-BA, and Dye2/DNA-BA) were prepared, and their nonlinear optical properties characterized using the second and third harmonic generation by Maker fringes technique. The second order nonlinear susceptibility was very small: 0.011 pm/V and 0.003 pm/V for p and s polarizations, respectively. This proves a completely statistical distribution of the dye molecules, i.e., absence of orientation induced either by the matrix or by the substrate.

According to THG measurements, highest value of $\chi_{elec}^{(3)}$ was found for Dye1\DNA-BA sample and was two orders of magnitude higher than that of the fused silica, the standard reference material. Within the experimental errors, there were no differences observed in $\chi_{elec}^{(3)}$ values which might have resulted from the ionic surfactant origin.

References

[1] R. Farchioni and G. Grosso, *Organic Electronic Materials* (Springer, Berlin, 2001).

[2] http://www.orgworld.com [03-05-2012].

[3] R. W. I. de Boer, T. M. Klapwijk, and A. F. Morpurgo, Appl. Phys. Lett., **83**, 4345 (2003).

[4] W. Bruting, *Physics of Organic Semiconductors* (Wiley-VCH, Weinheim, 2005).

[5] P. M. Borsenberger and D. S. Weiss, *Organic Photoreceptors for Imaging Systems* (M. Dekker, New York, 1993).

[6] J. A. Pople and S. H. Walmsley, Mol. Phys. **5**, 15 (1962).

[7] L. Salem, *Molecular Orbital Theory of Conjugated Systems* (Benjamin, New York, 1966).

[8] D. White, D. C. Bott and R. H. Weatherhead, Polymer **24,** (7) 805–809 (1983).

[9] E. M. Conwell, Phys. Rev. **103**, 51 (1956).

[10] N. F. Mott, Canad. J. Phys. **34**, 1356 (1956).

[11] A. Miller and E. Abrahams, Phys. Rev. **120**, 745 (1960).

[12] R. A. Street, *Hydrogenated amorphous silicon* (Cambridge University Press, Cambridge, 1991).

[13] H. Bässler, Phys. Stat. Sol. B, **175**, 15 (1993).

[14] V. Coropceanu, J. Cornil, D. A. da Silva Filho, Y. Olivier, R. Silbey, and J.-L. Brédas. Chem. Rev., **107**, 926 (2007).

[15] S. V. Novikov, D. H. Dunlap, V. M. Kenkre, P. E. Parris, and A. V. Vannikov, Phys. Rev. Lett., **81**, 4472 (1998).

[16] R. W. Boyd, *Nonlinear Optics* (Academic Press, Inc., New York, 2003).

[17] N. Bloembergen, *Nonlinear Optics* (Benjamin, New York, 1964).

[18] S. A. Akhmanov and R. V. Khokhlov, *Problems of Nonlinear Optics* (VINITI, Moscow 1964) *Engl. transl.* (Gordon & Breach, New York, 1972).

[19] Y. R. Shen, *The Principles of Nonlinear Optics* (Wiley, New York, 1984).

[20] D. Cotter and P. N. Butcher, *The Elements of Nonlinear Optics* (Cambridge University Press, Cambridge, 1990).

[21] J. F. Reintjes, *Nonlinear Optical Parametric Processes in Liquids and Gases* (Academic, Orlando, 1984).

[22] B. L. Davydov, L. D. Derkacheva, V. V. Dunina, M. E. Zhabotinski, V .F. Zolin, L. G. Koreneva and M. A. Samokhina, JETP Lett., **12**, 16–18 (1970).

[23] D. S. Chemla and J. Zyss, *Nonlinear Optical Properties of Organic Molecules and Crystals*, edited by D. S. Chemla, J. Zyss, (Academic, Orlando, 1987) Vols. I and II.

[24] P. N. Prasad and D. J. Williams, *Introduction to Nonlinear Optical Effects in Molecules and Polymers* (Wiley, New York, USA 1990).

[25] Ch. Bosshard and K. Sutter, *Organic Nonlinear Optical materials* (Gordon & Breach, Basel, 1995).

[26] B. Richard and A. Hallick, *A Molecular Graphics companion to an Introductory Course in Biology or Biochemistry* 1995.

[27] W. Saenger, *Principles of Nucleic Acid Structure* (Springer-Verlag, New York, 1984).

[28] H. Wagenknecht, Chem. In unserer Zeit **36**, 318 (2002) .

[29] B. A. Armitage, Top. Curr. Chem. **253**, 55– 76 (2005).

[30] B. H. Geierstanger and D. E. Wemmer, Annu. Rev. Biophys. Biomol. Struct. **24**, 463 (1995).

[31] M. Ikonen, L. Murtomaki and K. Kontturi, Colloids Surf. B, **66**, 73-83 (2008).

[32] S. Satoh , B. Fugetsu, M. Nomizu, N. Nishi, Polym. J., **37** (2) 94–101 (2005).

[33] M. Yamada and H. Aono, Polymer, **49**, 4658–4665 (2008).

[34] G. Juška, K. Arlauskas, M. Viliūnas and J. Kocka. Phys. Rev. Lett., **84**, 4946 (2000).

[35] J. Lorrmann, B. H. Badada, O. Inganäs, V. Dyakonov and C. Deibel, J. Appl. Phys., **108**, 113705 (2010).

[36] G. Juška, K. Arlauskas, M. Viliūnas, K. Genevičius, R. Osterbacka and H. Stubb, Phys. Rev. B **62**, R16 235 (2000).

[37] S. Bange, M. Schubert and D. Neher, Phys. Rev. B **81**, 035209 (2010).

[38] C. Deibel, A. Wagenpfahl and V. Dyakonov, Phys. Rev. B **80**, 075203 (2009).

[39] E. Gaubas, T. Čeponis, V. Kalendra, J. Kusakovskij and A. Uleckas, ISRN Materials Science **2012**, (2012).

[40] N. von Malm, J. Steiger, H. Heil, R. Schmechel and H. von Seggern. J. Appl. Phys., **92**, 7564 (2002).

[41] S. W. S. McKeever, *Thermoluminescence of solids* (Cambridge Uni. Press, Cambridge, 1985).

[42] R. R. Haering and E. N. Adams, *Phys. Rev.* **117**, 451-54 (1960).

[43] J. T. Randall and M. H. F. Wilkins. Proc. Roy. Soc. A, **184** ,366 (1945).

[44] G. F. J. Garlick and A. F. Gibson. Proc. Phys. Soc., **60**, 574 (1948).

[45] M. Schwoerer and H. C. Wolf, *Organic molecular solids* (Wiley-VCH, Weinheim, 2007).

[46] P. Maker, R. Terhune, M. Nisenoff and C. Savage, Phys. Rev. Lett. **8**, 21 (1962).

[47] J. Jerphagnon and S. Kurtz, J. Appl. Phys., **41**, 1667–1681 (1970).

[48] G. J. Lee, S. W. Cha, S. J. Jeon and S-I. Jin, J. Korean Phys. Soc. **39,** (5) 912 (2001).

[49] W. Herman and L. Hayden, J. Opt. Soc. Am. B, **12**, 416 (1995).

[50] N. Bloembergen and P. S. Pershan, Phys. Rev., **128**, 606 (1962).

[51] F. Kajzar and J. Messier, Phys. Rev. A, **32**, 2352 (1985).

[52] F. Kajzar, J. Messier and C. Rosilio, J. Appl. Phys., **60**, 3040 (1986).

[53] F. Kajzar, *Characterization Techniques and Tabulations for Organic Nonlinear Optical Materials*, (Marcel Dekker, Inc., New York, 1998).

[54] K. Kubodera and H. Kobayashi, Mol. Cryst. Liq. Cryst., **182**, 103 (1990).

[55] U. Gubler and C. Bosshard, Phys. Rev. B **61,** 10702 (2000).

[56] K.D. Singer, M.G. Kuzyk and J.E. Sohn, J. Opt. Soc. Am. B **4**, 968 (1987).

[57] C. Fiorini, F. Charra, J.-M. Nunzi and P. Raimond, J. Opt. Soc. Am. B **14**, 1984 (1997).

[58] G. Juška, K. Genevičius, M. Viliūnas, K. Arlauskas, R. Österbacka and H. Stubb, Proc. SPIE, **4415**, 145 (2001).

[59] A. J. Mozer, N. S. Sariciftci, A. Pivrikas, R. Österbacka, G. Juška, L. Brassat and H. Bässler, Phys. Rev. B, **71**, 035214 (2005).

[60] I. D. Parker, J. Appl. Phys., **75,** 3 (1994).

[61] C. Sentein, C. Fiorini, A. Lorin, L. Sicot and J.-M. Nunzi, Opt. Mater. **9**, 316 (1998).

[62] G. Weihao, Solid State Physics II Journal. (2009).

[63] M. Glatthaar, M. Niggemann, B. Zimmermann, P. Lewer, M. Riede, A. Hinsch, and J. Luther, Thin Solid Films, **491**, 298 (2005).

[64] I. Chen, J. Appl. Phys., **47**, 2988 (1976).

[65] N. F. Mott, Phil. Mag., **19**, 835(1969).

[66] L. G. Kaake, P. F. Barbara and X. Y. Zhu, J. Phys. Chem. Lett., **1,** 628–635 (2010).

[67] T. Munters, T. Martens, L. Goris, V. Vrindts, J. Manca, L. Lutsen, W. De Ceuninck, D. Vanderzande, L. De Schepper, J. Gelan, N. S. Sariciftci and C. J. Brabec, Thin Solid Films **403–404**, 247–251 (2002).

[68] H. G. Gilch and W. L. Wheelwright, J. Pol. Sci., **4**, 1337 (1966).

[69] H. Spreitzer, H. Becker, E. Kluge, W. Kreuder, H. Schenck, R. Demandt and H. Schoo, Adv. Mater., **10**, 1340 (1998).

[70] F. Louwet, D. Vanderzande, J. Gelan and J. Mullens, Macromolecules, **28**, 1330 (1995).

[71] F. Louwet, D. Vanderzande and J. Gelan, Synth. Met., **52**, 125 (1995).

[72] M. Kuik, J. Vandenbergh, L. Goris, E. J. Begemann, L. Lutsen, D. J. M. Vanderzande, J. V. Manca, and P. W. M. Blom, Appl. Phys. Lett., **99**, 183305 (2011).

[73] Z. Wang, S. Qu, X. Zeng, J. Liu, C. Zhang, M. Shi, F. Tan and Z. Wang, Curr. Appl. Phys. **9**, 1175–1179 (2009).

[74] J. G. Simmons and G. W. Taylor, Phys. Rev. B **5**, 1619 (1972).

[75] C. Manfredotti, R. Murri, A. Quirini and L. Vasanelli, Phys. Status Solidi (a) **38**, 685-93 (1976).

[76] E. Hernandez, L. Duran, C.A. Durante Ricon, G. Aranguren, C. Guerrero and J. Naranjo, Cryst. Res. Technol., **37**, 1227-33 (2002).

[77] L.I. Grossweiner, J. Appl. Phys. **24**,1306-07 (1953).

[78] V. Kažukauskas, H. Tzeng and S. A. Chen, Appl. Phys. Lett., **80**, 2017-19 (2002).

[79] V. Kažukauskas, Semicond. Sci. Technol. **19**, 1373-80 (2004).

[80] P. D. Townsend and R. H. Friend, Phys. Rev. B **40**, 3112 (1989).

[81] H. E. Tseng, C. Y. Liu and S. A. Chen, Appl. Phys. Lett., **88**, 042112 (2006).

[82] I. Glowacki and J. Ulański, J. Appl. Phys. **78**, 1019 (1995).

[83] H. E. Tseng, T.H. Jen, K. Y. Peng, and S.A. Chen, Appl. Phys. Lett. **84**, 1456 (2004).

[84] J. Grote, D. Diggs, R. Nelson, J. Zetts, F. Hopkins, N. Ogata, J. Hagen, E. Heckman, P. Yaney, M. Stone and L. Dalton, Mol. Cryst. Liq. Cryst. **426**, 16 (2005).

[85] J. G. Grote, J. A. Hagen, J. S. Zetts, R. L. Nelson, D. E. Diggs, M. O. Stone, P. P. Yaney, E. Heckman, C. Zhang, W. H. Steier, A. K.-Y. Jen, L. R.

Dalton, N. Ogata, M. J. Curley, S. J. Clarson and F. K. Hopkins, J. Phys. Chem. B **108**, 8584 (2004).

[86] E. M. Heckman, J. Hagen, P. Yaney, J. Grote and F. Hopkins, J. Appl. Phys. Lett. **87**, 211115 (2005).

[87] L. Wang, J. Yoshida, N. Ogata, S. Sasaki and T. Kajiyama, Chem. Mater. **13**, 1273 (2001).

[88] E. P. Bellido, A. D. Bobadilla, N. L. Rangel, H. Zhong, M. L. Norton, A. Sinitskii and J. M. Seminario, Nanotechnology **20**, 175102 (2009).

[89] J. Y. Kim, J. H. Jung, D. E. Lee and J. Joo, Synth. Met. **126**, 311 (2002).

[90] A. M. Nardes, M. Kemerink, R. A. J. Janssen, J. A. M. Bastiaansen, N. M. M. Kiggen, B. M. W. Langeveld, A. J. J. M. van Breemen and M. M. de Kok, Adv. Mater. **19**, 1196 (2007).

[91] C. S. S. Sangeeth, M. Jaiswal and R. Menon, J. Phys.: Condens. Matter, **21**, 072101 (2009).

[92] T. Kodama, A. Jain and K. E. Goodson, Nanoletters **9**, 2005 (2009).

[93] P. Tran, B. Alavi and G. Gruner, Phys. Rev. Lett. **85**, 1564 (2000).

[94] A. Inomata, T. Shimomura, S. Heike, M. Fujimori, T. Hashizume and K. Ito, J. Phys. Soc. J. **75**, 074803 (2006).

[95] H. Boettger and V. V. Bryksin, *Hopping Conduction in Solids* (Akademie-Verlag, Deerfield Beach, FL, 1985).

[96] A. Kaynak and Turk. J. Chem. **22**, 81 (1985).

[97] O. Krupka, A. El-Ghayoury, I. Rau, B. Sahraoui, J.G. Grote and F. Kajzar, Thin Solid Films **516**, 8932 (2008).

[98] L. Tang, Z. Sun, J. Guo and Z. Wang, Chin. Opt. Lett. **4**, 101 (2006).

[99] S. Marciniak, X. Crispin, K. Uvdal, M. Trzcinski, J. Birgerson, L. Groenendaal, F. Louwet and W. R. Salaneck, Synth. Met. **141**, 67–73 (2004).

[100] M. Mihaly, A. Comanescu, A. Rogozea, C. Pirvu and I. Rau, Proc. SPIE **7403**, 740308 (2009).

[101] B. Nithyaja, H. Misha, P. Radhakrishnan, and V. P. N. Nampoori, J. Appl. Phys. **109**, 023110 (2011).

[102] R. Vogel, P. Meredith, M. D. Harvey and H. Rubinsztein-Dunlop, Spectrochimica Acta Part A **60**, 245–249 (2004).

[103] P. N. Prasad, *Introduction to Biophotonics*, (John Wiley & Sons, New York, 2003), p. 545–557.

[104] F. Ito, T. Kakiuchi and T. Nagamura J. Phys. Chem. C, **111**, 6983-6988 (2007).

[105] M. Mihaly, I. Lacatusu and A. Meghea, Rev. Chim., **58,** 9 929 – 932 (2007).

[106] F. Kajzar, Y. Okada-Shudo, C. Meritt, and Z. Kafafi, Synth-Int. J. Methods **117**, 189 (2001).

[107] A. N. Naumov, D. A. Sidorov-Biryukov, A. B. Fedotov, and A. M. Zheltikov, Opt. Spectrosc., **90**, 78–783 (2001).

[108] B. Sharaoui, J. Luc, A. Meghea, R. Czaplicki, J-L. Fillaut and A. Migalska-Zalas, J. Opt. A: Pure Appl. Opt. **11**, 024005 (2009).

[109] K. Tanaka, Y. Okahata, J. Am. Chem. Soc. **118**, 10679 (1996).

[110] Y. Kawabe, L. Wang, S. Horinouchi and N. Ogata, Adv. Mater. **12**, 1281–1283 (2000).

[111] L. L. Wang, J. Yoshida, and N. Ogata, Chem. Mater. **13**, 1273 (2010).

[112] J.Niziol and J.Pielichowski, Opt. Mater. **32**, 673 (2010).

[113] L. R. Dalton, C. Xu, A. W. Harper, R. Ghson, B. Wu, Z. Liang, R. Montgomery and A. Jen, Nonlinear Opt., **10**, 383 (1995).

[114] Q. W. Pan, C. S. Fang, Z. H. Qin, Q. T. Gu, X. F. Cheng, D. Xu and J. Z. Yu, Mater. Lett., **57**, 2612 (2003).

[115] M. Amano and T. Kaino. J. Appl. Phys., **68**, 6024 (1990).

[116] X. H. Wang, D. P. West, N. B. McKeown and T. A. King, J. Opt. Soc. Am. B **15**, 1895 (1998).

[117] W. Nie, Adv. Mater. **5**, 520-545 (1993).

[118] J. Niziol, Z. Essaidi, M. Bednarz and B. Sahraoui, Opt.Mater. **31**, 501 (2009).

[119] W. Bi, N. Louvain, N. Mercier, J. Luc, I. Rau, F. Kajzar and B. Sahraoui, Adv. Mater. **20**, 1013–1017 (2008).